Supporting Information

Influence of Molecular Shape and Hydrogen Bonding on Glycolipid Self-assembly into Thermotropic Gyroid Phases

Soumi Das,[†] Caini Zheng,[†] Timothy P. Lodge,[†,] J. Ilja Siepmann,[†] Michelle A. Calabrese,[‡]* Theresa M. Reineke[†]*

[†]Department of Chemistry, University of Minnesota Twin Cities, 207 Pleasant St SE, Minneapolis, MN 55455, United States

[‡]Department of Chemical Engineering and Materials Science, University of Minnesota Twin Cities, 421 Washington Ave SE #151, Minneapolis, MN 55455, United States

Corresponding Author E-mail: treineke@umn.edu, mcalab@umn.edu

I. Reported Thermal Stability of DG in literature:

Table S1 Thermal stability of DG formed by molecular amphiphiles reported in the literature.

DG-forming system	DG thermal stability	Ref.
Discotic molecules	~58–70 °C	[1]
Guerbet maltoside	~19 °C	[2]
Guerbet galactosides	~26 °C	[3]
Guerbet mannosides	~12–35 °C	[4]
Sugar-Based Block Copolymers	~40 °C	[5]
Sugar–Polyolefin Conjugates	~58 °C	[6]

II. Materials and Instrumentation:

Lactose octaacetate (98%), *β*-D-maltose octaacetate (98%), 2-butyl-1-octanol (95%), 2-decyl-1-tetradecanol (97%), BF_3•Et_2O, $SnCl_4$ (98%), $NaOCH_3$ and the ion exchange resin DOWEX 50WX8-400 were obtained from MilliporeSigma (Milwaukee, WI). 2-octyl-1-dodecanol, and 2-hexyl-1-decanol (> 97%) were purchased from TCI Chemicals (Philadelphia, PA), and 2-ethyl-1-hexanol was received from Spectrum Chemical (New Brunswick, NJ). All the received chemicals and reagents were used as received. All the solvents used for this work were of ACS grade. Synthesized compounds were purified via column chromatography using silica gel (60-120 mesh) procured from Millipore-Sigma. The reactions were monitored by thin-layer chromatography (TLC) using plates coated with Silica Gel 60 obtained from Fisher Scientific. The NMR solvents were obtained from Millipore-Sigma.

^1H NMR and ^{13}C NMR spectra were recorded with a Bruker spectrometer at 400 and 150 MHz, respectively, using methanol-d_4 as the solvent. Chemical shifts were referenced to the residual protiated solvent peak, and spectral analyses yielded the reported chemical shifts in δ (ppm) and coupling constants J (Hz). Peak multiplicities are designated s (singlet), d (doublet), t (triplet), m (multiplet), and br (broadened).

III. General Glycolipid Synthesis Procedure

Guerbet maltosides and lactosides with varying branched alkyl tail lengths were synthesized in two steps following a well-established procedure typically starting from lactose octaacetate and *β*-D-maltose octaacetate.[7-8] We present a representative synthesis of one such compound.

In the first step, a Lewis acid-mediated direct glycosylation reaction was performed using acetyl-protected lactose or maltose with Guerbet alcohol. Using the Lewis acid $BF_3•Et_2O$, the reaction proceeded for 4 hours, predominantly yielding *β*-anomers of lactoside and maltoside peracetates. Alternatively, when $SnCl_4$ was employed as the Lewis acid, the glycosylation reactions yielded α-anomers of lactoside and maltoside peracetates predominantly, requiring 18 hours and 3 days of reaction time, respectively. Pure *α*- and *β*-anomers were successfully isolated from the reaction mixtures through column chromatography.

Lactose or maltose octaacetate (1.5 mmol, 1 eq.) was dissolved in anhydrous dichloromethane (20 mL) under a nitrogen atmosphere with constant stirring using a magnetic stir bar. Once a homogeneous solution was obtained, the selected Lewis acid (7.4 mmol, 5 eq.) was added. The desired Guerbet alcohol (2.2 mmol, 1.5 eq.) was then added dropwise to the reaction mixture at 0 °C. After completing the alcohol addition, the reaction was gradually brought to ambient temperature and allowed to proceed for the specified time. Following the reaction, the mixture was diluted with dichloromethane and quenched with saturated aqueous $NaHCO_3$. The product was extracted with dichloromethane (3 × 20 mL), and the combined organic layers were washed with saturated aqueous NaCl (15 mL) and dried over anhydrous Na_2SO_4. The crude reaction mixture was concentrated by rotary evaporation and purified via column chromatography using an ethyl acetate/hexane solvent system. The acetyl ester of the Guerbet alcohol, a side product, was first eluted using pure hexanes. The desired anomers were subsequently collected using a hexane/ethyl acetate mixture. The ethyl acetate/hexane ratio varied depending on the Guerbet chain length, ranging from 36% v/v for the $–C_{14}C_{10}$ chain to 42% v/v for the $–C_6C_2$ chain.

The Guerbet glycolipid peracetates were deprotected through Zemplén deacetylation as described previously. The peracetylated glycolipid was dissolved in methanol (MeOH), and the reaction mixture was adjusted to pH 9 using solid sodium methoxide (NaOMe) at 22 °C. Deacetylation was monitored by TLC and found to be complete after 16 hours.

The reaction mixture was then subjected to ion exchange using Dowex® resin (H^+ form). Following resin removal by filtration, the desired glycolipids were obtained by concentrating the filtrate. The purities of the synthesized glycolipids were confirmed by ^1H and ^{13}C NMR spectroscopy[2, 8-11] (Figures S1–S20).

Finally, all samples were lyophilized for 4 days to thoroughly remove trace amounts of water from these hygroscopic compounds.

IV. Elemental Analysis:

Combustion elemental analyses were conducted at Atlantic Microlab (Norcross, GA, USA) on lyophilized samples to confirm the absence of moisture.

V. Differential Scanning Calorimetry (DSC):

Differential scanning calorimetry (DSC) experiments were conducted using a Mettler Toledo DSC 1 instrument equipped with cooling accessories and operating under a nitrogen atmosphere. For sample preparation, approximately 5–8 mg of lyophilized glycolipids were sealed in Tzero aluminum pans (DSC Consumables, Austin, MN). After equilibrating the samples at 25 °C, DSC measurements were performed during heating at a rate of 5 °C/min. The data were analyzed using TA Instruments thermal analysis software. The reported results and thermograms correspond to the first heating cycle, which clearly revealed mobility transitions and thermotropic liquid crystalline phase transitions.

VI. Polarized Optical Microscopy (POM)

Polarized optical microscopy (POM) was used to study liquid crystal phase textures using an Olympus BX53 polarizing light microscope. The microscope was equipped with a Linkam LTS420 hot stage and a T95 temperature controller, operated via Linksys 32 software. Digital images were captured using a QiCam Fast 1394 12-bit camera. Dried glycolipid samples were placed on clean microscope slides, and a coverslip with silicone grease applied along the edges was used to protect the samples from atmospheric exposure and minimize moisture uptake. The samples were heated at a rate of 10 °C/min to the desired temperature and annealed for at least 5 minutes before observations were recorded.

VII. Small-Angle X-ray Scattering (SAXS)

Sample Preparation:

30 mg portion of the lyophilized glycolipid sample was hermetically sealed in a TZero aluminum DSC pan (TA Instruments, New Castle, DE, USA) in an inert atmosphere glovebox under argon to prevent unwanted moisture uptake.

Measurement:

Lab source SAXS was performed at the Characterization Facility, University of Minnesota by using a SAXSLAB Ganesha 300XL instrument. Cu Kα X-rays ($\lambda = 1.54$ Å) generated by a Xenocs Geni3DX source were collimated through 2 sets of 4-bladed slits (JJ X-ray, A/S). 2D-SAXS patterns were acquired using a EIGER R 1 M Dectris detector (7.72 cm × 7.99 cm rectangular area) with 1030 × 1065 pixels (75 µm × 75 µm pixel size) at a sample-to-detector distance of 46.8 cm and a wave vector, q, covering $q = 0.02\text{–}0.7$ Å^{-1}. SAXS diffractograms were calibrated by using a silver behenate standard with a *d*-spacing of 58.38 Å. All 2D-SAXS patterns were azimuthally integrated to obtain the 1D scattering intensity, using the DataSqueeze software.

Variable temperature small-angle X-ray scattering (SAXS) analyses were performed using a SAXSLAB Ganesha 300XL instrument at the Characterization Facility of the University of Minnesota and at the 5-ID-D and 12-ID-B beamlines of the Advanced Photon Source (Argonne, IL). Samples were either loaded into a sample array stage at the beamline, providing stable temperature control (±3 °C) over a range of 25–205 °C, or thermostatted on a Linkam hot stage with ±1 °C temperature stability. Samples were heated at a rate of 10 °C/min to the target temperature and allowed to thermally equilibrate for at least 10 minutes prior to X-ray exposure.

At the 5-ID-D beamline, analyses were conducted with an 8.5 m sample-to-detector distance (SDD) and a beam energy of 17 keV. At the 12-ID-B beamline, experiments used a 3.6 m SDD and a beam energy of 12 keV. In both cases, flight tubes for the incident and scattered beams were maintained under vacuum to reduce air scattering. For 2D-SAXS at the 5-ID-D beamline, data were collected using three Rayonix MX170-HS detectors (active area: 170 × 170 mm^2, resolution: 3840 × 3840 pixels, pixel size: 86.6 × 86.6 μm). At the 12-ID-B beamline, 2D-SAXS patterns were recorded on a Pilatus 2M detector (active area: 253.7 × 288.8 mm^2, resolution: 1475 × 1679 pixels, pixel size: 172 × 172 μm), while 2D-WAXS patterns were collected on a Pilatus 300K detector (active area: 33.5 × 83.8 mm^2, resolution: 487 × 619 pixels, pixel size: 172 × 172 μm). These setups enabled the acquisition of scattering data over a wavevector range of $0.003 \leq |q| \leq 0.5$ $Å^{-1}$. To ensure sample homogeneity at each temperature, five 2D-SAXS patterns were recorded at different locations within each sample pan.

In case of SAXSLAB Ganesha instrument, an EIGER R 1 M Dectris detector with 1030 × 1065 pixels (75 μm × 75 μm pixel size) was used to capture the 2D-SAXS patterns at a sample-to-detector distance of 46.8 cm and a wave vector, q, covering $q = 0.02–0.7$ $Å^{-1}$. A silver behenate standard was used to calibrate the acquired SAXS data.

The 2D scattering data were azimuthally integrated to obtain the scattered intensity $I(q)$ as a function of $|\boldsymbol{q}| = 4\pi\sin(\theta/2) / \lambda$, where θ is the scattering angle and λ is the incident beam wavelength. In the presented SAXS data (Figure S23-S29, S31, S33-37, S39), Bragg peaks corresponding to ordered morphologies were indexed using 1D-SAXS indexing macro for Igor Pro.[12]

VIII. Simulation details:

MD simulations were conducted to study the phase behaviors of six glycolipids including *α*-Cel–C_8C_4, *β*-Cel–C_8C_4, *α*-Mal–C_8C_4, *β*-Mal–C_8C_4, *α*-Lac–C_8C_4 and *β*-Lac–C_8C_4. A combined force field is applied to model the glycolipids, where CHARMM all-atom potentials[13-16] and TraPPE united-atom potentials[17-19] are used to model the sugar head and the alkyl tail, respectively. The initial LAM configuration is constructed by inserting the glycolipids into an orthorhombic simulation cell using the PACKMOL package.[20] The simulation is then carried out using GROMACS 2019[21] with an isothermal–isobaric (NPT) ensemble, where the simulation box is allowed to fluctuate in three dimensions independently. In the first stage, the Berendsen thermostat with a time constant of 0.4 ps and Berendsen barostat with a time constant of 10 ps are used for temperature and pressure coupling.[22] After at least 1 μs, atom coordinates and velocities from the last step of the first stage were used to initialize the second simulation run. During the second stage, the Nosé-Hoover thermostat[23-24] with a time constant of 4 ps and the Parrinello-Rahman barostat[25-26] with a time constant of 10 ps are used for temperature and pressure control, respectively. Systems are allowed to equilibrate for at least 50 ns and 200 ns frames from the production stage were used for analysis.

IX. Characterization Data for Synthesized Compounds

2-ethyl-butyl-D-lactoside, (α-*Lac-C_6C_2*)

R_f = 0.48 (EtOAc:Hexane = 1:1.4); Overall yield= 29%. ^{1}H NMR (400 MHz, MeOD, 22 °C) δ (ppm) 4.76 (d, J = 3.7 Hz, 1H), 4.38 (d, J = 7.5 Hz, 1H), 3.90 (dd, J = 12.0, 4.0 Hz, 1H), 3.86 – 3.77 (m, 4H), 3.75 – 3.67 (m, 2H), 3.67 – 3.55 (m, 4H), 3.54 – 3.46 (m, 2H), 3.39 – 3.34 (m, 1H), 1.65 – 1.28 (m, 10H), 0.97 – 0.90 (m, 6H); ^{13}C NMR (101 MHz, MeOD, 22 °C) δ (ppm) 105.2, 100.3, 100.2, 81.1, 81.1, 77.1, 74.9, 73.5, 73.4, 72.6, 72.2, 72.0, 72.0, 70.3, 62.5, 61.9, 41.0, 40.8, 31.6, 31.5, 30.3, 30.2, 24.9, 24.8, 24.1, 14.5, 14.4, 11.6, 11.3; Anal. Calc.: $C_{20}H_{38}O_{11}$; C, 52.85; H, 8.43; Found: C, 52.56; H, 8.46.

2-ethyl-butyl-D-lactoside, (β-**Lac-C$_6$C$_2$*****)***

R$_f$ = 0.48 (EtOAc:Hexane = 1:1.4); Overall yield= 25%. ^{1}H NMR (400 MHz, MeOD, 22°C) δ (ppm) 4.37 (d, J = 7.5 Hz, 1H), 4.26 (d, J = 7.8 Hz, 1H), 3.94 – 3.67 (m, 6H), 3.62 – 3.45 (m, 5H), 3.40 (ddt, J = 9.5, 6.7, 4.5 Hz, 2H), 3.25 (dd, J = 9.0, 7.8 Hz, 1H), 1.59 – 1.26 (m, 10H), 0.90 (td, J = 7.3, 1.3 Hz, 6H); ^{13}C NMR (101 MHz, MeOD, 22 °C) δ (ppm) 105.1, 104.7, 80.8, 77.1, 76.6, 76.4, 74.8, 74.8, 73.7, 73.6, 72.6, 70.3, 62.5, 62.0, 41.1, 41.0, 31.5, 30.2, 24.7, 24.7, 24.1, 14.5, 11.4, 11.3; Anal. Calc.: $C_{20}H_{38}O_{11}$; C, 52.85; H, 8.43; Found: C, 53.65; H, 8.49.

2-butyl-octyl-D-lactoside, (α-**Lac-C$_8$C$_4$*****)***

R$_f$ = 0.48 (EtOAc:Hexane = 1:1.5); Overall yield= 22%. ^{1}H NMR (400 MHz, MeOD, 22 °C) δ (ppm) 4.74 (d, J = 3.8 Hz, 1H), 4.35 (d, J = 7.6 Hz, 1H), 3.91 – 3.75 (m, 5H), 3.74 – 3.65 (m, 2H), 3.64 – 3.53 (m, 4H), 3.53 – 3.43 (m, 2H), 3.34 (d, J = 5.4 Hz, 1H), 1.63 (s, 1H), 1.48 – 1.24 (m, 17H), 0.91 (td, J = 6.6, 4.0 Hz, 6H); ^{13}C NMR (101 MHz, MeOD, 22 °C) δ (ppm) 105.2, 100.3, 81.1, 77.1, 74.9, 73.5, 73.4, 72.6, 72.5, 72.2, 70.3, 62.5, 61.9, 39.4, 33.1, 33.1, 32.4, 32.1, 30.9, 30.8, 30.3, 30.1, 28.0, 27.9, 24.1, 23.7, 14.5, 14.5. Anal. Calc.: $C_{24}H_{46}O_{11}$; C, 56.45; H, 9.08; Found: C, 56.34; H, 9.07.

2-butyl-octyl-D-lactoside, (β-Lac-C$_8$C$_4$)

R$_f$ = 0.48 (EtOAc:Hexane = 1:1.5); Overall yield= 26%. ^{1}H NMR (400 MHz, MeOD, 22 °C) δ (ppm) 4.37 (d, J = 7.5 Hz, 1H), 4.25 (d, J = 7.8 Hz, 1H), 3.93 – 3.74 (m, 5H), 3.70 (dd, J = 11.4, 4.6 Hz, 1H), 3.62 – 3.46 (m, 5H), 3.40 (ddd, *J* = 8.0, 6.3, 3.1 Hz, 2H), 3.25 (dd, *J* = 9.0, 7.8 Hz, 1H), 1.65 – 1.56 (m, 1H), 1.46 – 1.20 (m, 17H), 0.91 (td, *J* = 6.8, 3.9 Hz, 6H); ^{13}C NMR (101 MHz, MeOD, 22 °C) *δ* (ppm) 105.1, 104.7, 80.8, 77.1, 76.6, 76.4, 74.8, 74.8, 74.1, 74.0, 72.6, 70.3, 62.5, 62.0, 39.6, 33.1, 32.3, 32.3, 32.0, 32.0, 30.9, 30.2, 27.9, 24.1, 23.7, 14.5, 14.4; Anal. Calc.: $C_{24}H_{46}O_{11}$; C, 56.45; H, 9.08; Found: C, 55.54; H, 9.16.

2-hexyl-decyl-D-lactoside, (α-Lac-$C_{10}C_6$)

R_f = 0.46 (EtOAc:Hexane = 1:1.6); Overall yield= 16%. ^{1}H NMR (400 MHz, MeOD, 22 °C) *δ* (ppm) 4.74 (d, *J* = 3.7 Hz, 1H), 4.36 (d, *J* = 7.6 Hz, 1H), 3.92 – 3.74 (m, 5H), 3.74 – 3.65 (m, 2H), 3.64 – 3.51 (m, 4H), 3.51 – 3.43 (m, 2H), 3.36 – 3.32 (m, 1H), 1.63 (t, *J* = 6.4 Hz, 1H), 1.49 – 1.20 (m, 25H), 0.91 (td, *J* = 6.9, 1.6 Hz, 6H); ^{13}C NMR (101 MHz, MeOD, 22 °C) *δ* (ppm) 105.2, 100.2, 81.0, 77.1, 74.9, 73.5, 73.3, 72.5, 72.5, 72.2, 70.3, 62.5, 61.9, 39.4, 39.3, 33.1, 33.1, 32.4, 32.4, 31.1, 31.1, 30.8, 30.8, 30.8, 30.7, 30.5, 28.0, 27.9, 27.8, 23.7, 14.5; Anal. Calc.: $C_{28}H_{54}O_{11}$; C, 59.34; H, 9.60; Found: C, 59.33; H, 9.62.

2-hexyl-decyl-D-lactoside, (β-Lac-$C_{10}C_6$)

R_f = 0.46 (EtOAc:Hexane = 1:1.6); Overall yield= 17%. ^{1}H NMR (400 MHz, MeOD, 22 °C) *δ* (ppm) 4.37 (d, *J* = 7.5 Hz, 1H), 4.25 (d, *J* = 7.9 Hz, 1H), 3.94 – 3.84 (m, 2H), 3.84 – 3.74 (m, 3H), 3.70 (dd, *J* = 11.5, 4.6 Hz, 1H), 3.62 – 3.45 (m, 5H), 3.44 – 3.36 (m, 2H), 3.25 (dd, *J* = 9.0, 7.8 Hz, 1H), 1.65 – 1.56 (m, 1H), 1.30 (s, 25H), 0.94 – 0.86 (m, 6H); ^{13}C NMR (101 MHz, MeOD, 22 °C) *δ* (ppm) 105.1, 104.7, 80.8, 77.1, 76.6, 76.4, 74.8, 74.8, 74.1, 72.6, 70.3, 62.5, 62.0, 39.5, 33.1, 33.1, 32.3, 32.2, 32.2, 31.2, 30.8, 30.7, 30.5, 27.9, 23.7, 14.5; Anal. Calc.: $C_{28}H_{54}O_{11}$; C, 59.34; H, 9.60; Found: C, 59.15; H, 9.63.

2-octyl-dodecyl-D-lactoside, (α-Lac-$C_{12}C_8$)

R_f = 0.47 (EtOAc:Hexane = 1:1.7); Overall yield= 18%. ^{1}H NMR (400 MHz, MeOD, 22 °C) δ (ppm) 4.74 (d, J = 3.8 Hz, 1H), 4.36 (d, J = 7.6 Hz, 1H), 3.91 – 3.74 (m, 5H), 3.73 – 3.63 (m, 2H), 3.63 – 3.51 (m, 4H), 3.47 (td, J = 9.4, 3.5 Hz, 2H), 3.34 (d, J = 5.5 Hz, 1H), 1.63 (s, 1H), 1.30 (s, 33H), 0.95 – 0.86 (m, 6H); ^{13}C NMR (101 MHz, MeOD, 22 °C) δ (ppm) 105.2, 100.3, 81.0, 77.1, 74.9, 73.5, 73.4, 72.6, 72.2, 70.3, 62.5, 61.9, 39.3, 33.1, 32.3, 31.1, 31.1, 31.1, 30.8, 30.8, 30.7, 30.5, 27.9, 27.8, 23.8, 14.5; Anal. Calc.: $C_{32}H_{62}O_{11}$; C, 61.71; H, 10.03; Found: C, 61.57; H, 9.94.

2-octyl-dodecyl-D-lactoside, (β-Lac-$C_{12}C_8$)

R_f = 0.47 (EtOAc:Hexane = 1:1.7); Overall yield= 13%. ^{1}H NMR (400 MHz, MeOD, 22 °C) δ (ppm) 4.37 (d, J = 7.6 Hz, 1H), 4.25 (d, J = 7.8 Hz, 1H), 3.92 – 3.85 (m, 2H), 3.84 – 3.75 (m, 3H), 3.70 (dd, J = 11.5, 4.6 Hz, 1H), 3.61 – 3.46 (m, 5H), 3.40 (ddd, J = 9.5, 5.0, 2.5 Hz, 2H), 3.25 (dd, J = 9.0, 7.8 Hz, 1H), 1.66 – 1.56 (m, 1H), 1.40 (d, J = 8.3 Hz, 2H), 1.30 (s, 31H), 0.94 – 0.87 (m, 6H); ^{13}C NMR (101 MHz, MeOD, 22 °C) δ (ppm) 105.1, 104.7, 80.8, 77.1, 76.6, 76.4, 74.8, 74.1, 72.6, 70.3, 62.5, 62.0, 39.5, 33.1, 32.2, 31.1, 30.8, 30.8, 30.7, 30.5, 27.8, 23.8, 14.5; Anal. Calc.: $C_{32}H_{62}O_{11}$; C, 61.71; H, 10.03; Found: C, 61.43; H, 10.01.

2-decyl-tetradecyl-D-lactoside, (α-Lac-$C_{14}C_{10}$)

R_f = 0.45 (EtOAc:Hexane = 1:1.8); Overall yield= 15%. ^{1}H NMR (400 MHz, MeOD. 22 °C) δ (ppm) 4.74 (d, J = 3.7 Hz, 1H), 4.35 (d, J = 7.7 Hz, 1H), 3.91 – 3.74 (m, 5H), 3.74 – 3.65 (m, 2H), 3.57 (dddd, J = 17.1, 9.9, 8.7, 6.8 Hz, 4H), 3.47 (td, J = 9.4, 3.5 Hz, 2H), 3.35 – 3.32 (m, 1H), 1.63 (s, 1H), 1.49 – 1.21 (m, 41H), 0.95 – 0.86 (m, 6H); ^{13}C NMR (101 MHz, MeOD, 22 °C) δ 105.2, 100.3, 81.0, 77.1, 74.9, 73.4, 72.6, 72.2, 70.3, 62.5, 61.9, 39.3, 33.1, 32.3, 31.1, 30.8, 30.5, 23.8, 14.5; Anal. Calc.: $C_{36}H_{70}O_{11}$; C, 63.69; H, 10.39; Found: C, 63.61; H, 10.32.

2-decyl-tetradecyl-D-lactoside, (β-Lac-$C_{14}C_{10}$)

R_f = 0.45 (EtOAc:Hexane = 1:1.8); Overall yield= 26%. ^{1}H NMR (400 MHz, MeOD, 22 °C) δ (ppm) 4.37 (d, J = 7.5 Hz, 1H), 4.25 (d, J = 7.8 Hz, 1H), 3.93 – 3.74 (m, 5H), 3.70 (dd, J = 11.4, 4.6 Hz, 2H), 3.62 – 3.45 (m, 5H), 3.40 (dd, J = 9.5, 6.1 Hz, 2H), 3.25 (t, J = 8.4 Hz, 1H), 1.61 (s, 1H), 1.30 (s, 41H), 0.90 (t, J = 6.7 Hz, 6H); ^{13}C NMR (126 MHz, MeOD, 22 °C) δ (ppm) 105.1, 104.7, 80.8, 77.1, 76.6, 76.4, 74.8, 74.8, 74.1, 72.6, 70.3, 62.5, 62.0, 39.5, 33.1, 32.2, 31.1, 31.1, 30.8, 30.8, 30.8, 30.7, 30.5, 27.8, 23.8, 14.5; Anal. Calc.: $C_{36}H_{70}O_{11}$; C, 63.69; H, 10.39; Found: C, 63.89; H, 10.62.

2-ethyl-butyl-D-maltoside, (α-Mal-C_6C_2)

R_f = 0.48 (EtOAc:Hexane = 1:1.4); Overall yield= 15%. ^{1}H NMR (400 MHz, MeOD, 22 °C) δ (ppm) 5.13 (d, J = 3.7 Hz, 1H), 4.74 (d, J = 3.7 Hz, 1H), 3.92 – 3.77 (m, 4H), 3.73 – 3.59 (m, 5H), 3.55 – 3.41 (m, 3H), 3.36 – 3.32 (m, 1H), 3.30 – 3.24 (m, 1H), 1.62 – 1.44 (m, 2H), 1.42 – 1.28 (m, 7H), 0.91 (tdd, J = 7.4, 4.8, 2.2 Hz, 6H); ^{13}C NMR (101 MHz, MeOD, 22 °C) δ (ppm) 103.1, 100.4, 100.3, 82.0, 75.1, 74.2, 74.8, 74.3, 73.3, 72.4, 72.0, 71.9, 71.5, 62.8, 62.1, 41.0, 40.9, 31.6, 31.5, 30.3, 30.1, 24.9, 24.2, 24.1, 14.5, 14.5, 11.6, 11.3; Anal. Calc.: $C_{20}H_{38}O_{11}$; C, 52.85; H, 8.43; Found: C, 51.69; H, 8.42.

2-ethyl-butyl-D-maltoside, (β-Mal-C_6C_2)

R_f = 0.48 (EtOAc:Hexane = 1:1.4); Overall yield= 51%. ^{1}H NMR (400 MHz, MeOD, 22°C) δ (ppm) 5.16 (d, J = 3.8 Hz, 1H), 4.24 (d, J = 7.8 Hz, 1H), 3.92 – 3.78 (m, 4H), 3.73 – 3.51 (m, 5H), 3.47 – 3.33 (m, 3H), 3.30 – 3.19 (m, 2H), 1.57 – 1.41 (m, 2H), 1.40 – 1.27 (m, 7H), 0.90 (td, *J* = 7.3, 1.2 Hz, 6H); ^{13}C NMR (101 MHz, MeOD, 22 °C) δ (ppm) 104.8, 102.9, 81.4, 77.9, 76.6, 75.1, 74.8, 74.2, 73.6, 71.5, 62.8, 62.2, 41.1, 31.5, 30.2, 24.7, 24.2, 14.5, 11.4; Anal. Calc.: $C_{20}H_{38}O_{11}$; C, 52.85; H, 8.43; Found: C, 51.63; H, 8.46.

2-butyl-octyl-D-maltoside, (α-Mal-C_8C_4)

R_f = 0.48 (EtOAc:Hexane = 1:1.5); Overall yield= 19%. ^{1}H NMR (400 MHz, MeOD, 22 °C) δ (ppm) 5.13 (d, *J* = 3.8 Hz, 1H), 4.74 (d, *J* = 3.7 Hz, 1H), 3.93 – 3.76 (m, 4H), 3.73 – 3.57 (m, 5H), 3.57 – 3.40 (m, 3H), 3.33 (d, *J* = 6.0 Hz, 1H), 3.28 – 3.21 (m, 1H), 1.64 (s, 1H), 1.45 – 1.26 (m, 16H), 0.98 – 0.87 (m, 6H); ^{13}C NMR (101 MHz, MeOD, 22 °C) δ (ppm) 103.1, 100.3, 82.0, 75.1, 74.8, 74.3, 72.4, 71.5, 39.3, 33.1, 32.4, 28.0, 24.2, 23.7, 14.5; Anal. Calc.: $C_{24}H_{46}O_{11}$; C, 56.45; H, 9.08; Found: C, 55.24; H, 9.01.

2-butyl-octyl-D-maltoside, (β-Mal-C_8C_4)

R_f = 0.48 (EtOAc:Hexane = 1:1.5); Overall yield= 27%. ^{1}H NMR (400 MHz, MeOD, 22 °C) δ (ppm) 5.18 (d, *J* = 3.8 Hz, 1H), 4.26 (d, *J* = 7.8 Hz, 1H), 3.93 – 3.81 (m, 4H), 3.74 – 3.53 (m, 5H), 3.48 – 3.35 (m, 3H), 3.27 (ddd, *J* = 11.5, 9.4, 8.4 Hz, 2H), 1.63 (s, 1H), 1.43 (qd, *J* = 7.9, 3.7 Hz, 2H), 1.33 (q, *J* = 3.2 Hz, 14H), 0.93 (td, *J* = 6.8, 3.8 Hz, 6H); ^{13}C NMR (101 MHz, MeOD, 22 °C) δ (ppm) 104.8, 102.9, 81.4, 77.9, 76.6, 75.1, 74.8, 74.2, 74.1, 71.5, 62.8, 62.2, 39.6, 33.1, 32.3, 32.0, 30.9, 30.2, 27.9, 24.2, 23.8, 14.5, 14.4; Anal. Calc.: $C_{24}H_{46}O_{11}$; C, 56.45; H, 9.08; Found: C, 55.54; H, 9.00.

2-hexyl-decyl-D-maltoside, (α-Mal-$C_{10}C_6$)

R_f = 0.46 (EtOAc:Hexane = 1:1.6); Overall yield= 15%. ^{1}H NMR (400 MHz, MeOD, 22 °C) δ (ppm) 5.13 (d, J = 3.8 Hz, 1H), 4.74 (d, J = 3.8 Hz, 1H), 3.91 – 3.76 (m, 4H), 3.72 – 3.58 (m, 5H), 3.55 – 3.41 (m, 3H), 3.33 (d, J = 5.7 Hz, 1H), 3.27 (d, J = 9.3 Hz, 1H), 1.64 (s, 1H), 1.46 – 1.38 (m, 1H), 1.32 (d, J = 11.0 Hz, 23H), 0.91 (td, J = 6.8, 1.9 Hz, 6H); ^{13}C NMR (101 MHz, MeOD, 22 °C) δ (ppm) 103.1, 100.3, 81.9, 75.1, 74.9, 74.8, 74.3, 73.3, 72.4, 71.5, 62.7, 62.0, 39.3, 39.3, 33.1, 33.0, 32.3, 31.2, 31.1, 30.8, 30.8, 30.8, 30.7, 30.5, 28.0, 27.9, 27.8, 27.7, 23.7, 14.5, 14.5, 14.5; Anal. Calc.: $C_{28}H_{54}O_{11}$; C, 59.34; H, 9.60; Found: C, 58.49; H, 9.54.

2-hexyl-decyl-D-maltoside, (β-Mal-$C_{10}C_6$)

R_f = 0.46 (EtOAc:Hexane = 1:1.6); Overall yield= 28%. ^{1}H NMR (400 MHz, MeOD, 22 °C) δ (ppm) 5.16 (d, J = 3.8 Hz, 1H), 4.24 (d, J = 7.8 Hz, 1H), 3.92 – 3.77 (m, 4H), 3.71 – 3.51 (m, 6H), 3.47 – 3.33 (m, 3H), 3.25 (ddd, J = 11.2, 9.4, 8.4 Hz, 2H), 1.61 (s, 1H), 1.39 (d, J = 13.3 Hz, 2H), 1.30 (s, 22H), 0.94 – 0.87 (m, 6H); ^{13}C NMR (101 MHz, MeOD, 22 °C) δ (ppm) 104.8, 102.9, 81.4, 77.9, 76.6, 75.1, 74.8, 74.2, 74.1, 71.5, 62.8, 62.2, 49.5, 49.3, 39.6, 33.1, 33.1, 32.2, 31.2, 30.9, 30.7, 30.5, 27.9, 23.7, 14.5; Anal. Calc.: $C_{28}H_{54}O_{11}$; C, 59.34; H, 9.60; Found: C, 58.19; H, 9.64.

2-octyl-dodecyl-D-maltoside, (α-Mal-$C_{12}C_8$)

R_f = 0.47 (EtOAc:Hexane = 1:1.7); Overall yield= 11%. ^{1}H NMR (400 MHz, MeOD, 22 °C) δ (ppm) 5.13 (d, J = 3.8 Hz, 1H), 4.74 (d, J = 3.8 Hz, 1H), 3.92 – 3.76 (m, 4H), 3.73 – 3.58 (m, 5H), 3.52 (dd, J = 9.9, 8.7 Hz, 1H), 3.44 (dd, J = 9.7, 3.8 Hz, 2H), 3.33 (d, J = 5.8 Hz, 1H), 3.27 (d, J = 9.4 Hz, 1H), 1.64 (s, 1H), 1.30 (s, 32H), 0.95 – 0.87 (m, 6H); ^{13}C NMR (101 MHz, MeOD, 22 °C)

δ (ppm) 103.1, 100.4, 81.9, 75.1, 74.9, 74.8, 74.3, 73.3, 72.4, 71.5, 62.7, 62.0, 39.3, 33.1, 32.3, 31.1, 31.1, 30.8, 30.8, 30.5, 27.9, 27.7, 23.8, 14.5; Anal. Calc.: $C_{32}H_{62}O_{11}$; C, 61.71; H, 10.03; Found: C, 61.23; H, 10.05.

2-octyl-dodecyl-D-maltoside, (β-Mal-$C_{12}C_8$)

R_f = 0.47 (EtOAc:Hexane = 1:1.7); Overall yield= 43%. ^{1}H NMR (400 MHz, MeOD, 22 °C) δ (ppm) 5.18 (d, J = 3.8 Hz, 1H), 4.26 (d, J = 7.8 Hz, 1H), 3.93 – 3.80 (m, 4H), 3.74 – 3.53 (m, 5H), 3.48 – 3.35 (m, 3H), 3.31 – 3.23 (m, 2H), 1.66 – 1.60 (m, 1H), 1.32 (s, 32H), 0.96 – 0.88 (m, 6H); ^{13}C NMR (101 MHz, MeOD, 22 °C) δ (ppm) 104.7, 102.9, 81.3, 77.9, 76.6, 75.1, 74.8, 74.7, 74.2, 74.1, 71.5, 62.8, 62.2, 39.5, 33.1, 32.2, 32.2, 31.2, 31.1, 30.8, 30.8, 30.7, 30.5, 27.8, 23.7, 14.5; Anal. Calc.: $C_{32}H_{62}O_{11}$; C, 61.71; H, 10.03; Found: C, 61.12; H, 10.02.

2-decyl-tetradecyl-D-maltoside, (α-Mal-$C_{14}C_{10}$)

R_f = 0.45 (EtOAc:Hexane = 1:1.8); Overall yield= 19%. ^{1}H NMR (400 MHz, MeOD. 22 °C) δ (ppm) 5.16 (d, J = 3.8 Hz, 1H), 4.76 (d, J = 3.8 Hz, 1H), 3.94 – 3.78 (m, 4H), 3.74 – 3.60 (m, 5H), 3.57 – 3.44 (m, 3H), 3.35 (d, J = 5.5 Hz, 1H), 3.29 (d, J = 9.3 Hz, 1H), 1.71 – 1.62 (m, 1H), 1.49 – 1.28 (m, 40H), 0.96 – 0.89 (m, 6H); ^{13}C NMR (101 MHz, MeOD, 22 °C) δ 103.0, 100.3, 81.9, 75.1, 74.9, 74.7, 74.3, 73.3, 72.4, 72.4, 71.4, 62.7, 62.0, 39.3, 33.1, 32.2, 31.1, 31.1, 31.1, 30.8, 30.8, 30.8, 30.8, 30.5, 27.9, 27.9, 27.7, 23.8, 14.5; Anal. Calc.: $C_{36}H_{70}O_{11}$; C, 63.69; H, 10.39; Found: C, 62.92; H, 10.43.

2-decyl-tetradecyl-D-maltoside, (β-Mal-$C_{14}C_{10}$)

R_f = 0.45 (EtOAc:Hexane = 1:1.8); Overall yield= 27%. ^{1}H NMR (400 MHz, MeOD, 22 °C) δ (ppm) 5.16 (d, J = 3.8 Hz, 1H), 4.24 (d, J = 7.8 Hz, 1H), 3.92 – 3.77 (m, 4H), 3.72 – 3.51 (m, 5H), 3.47 – 3.32 (m, 3H), 3.29 – 3.19 (m, 2H), 1.61 (s, 1H), 1.29 (s, 40H), 0.93 – 0.87 (m, 6H); ^{13}C NMR (101 MHz, MeOD, 22 °C) *δ* (ppm) 104.7, 102.9, 81.3, 77.9, 76.6, 75.1, 74.8, 74.7, 74.2, 74.1, 71.5, 62.8, 62.2, 39.5, 33.1, 32.2, 32.1, 31.1, 31.1, 30.8, 30.8, 30.8, 30.8, 30.7, 30.5, 27.8, 23.8, 14.5; Anal. Calc.: $C_{36}H_{70}O_{11}$; C, 63.69; H, 10.39; Found: C, 62.79; H, 10.39.

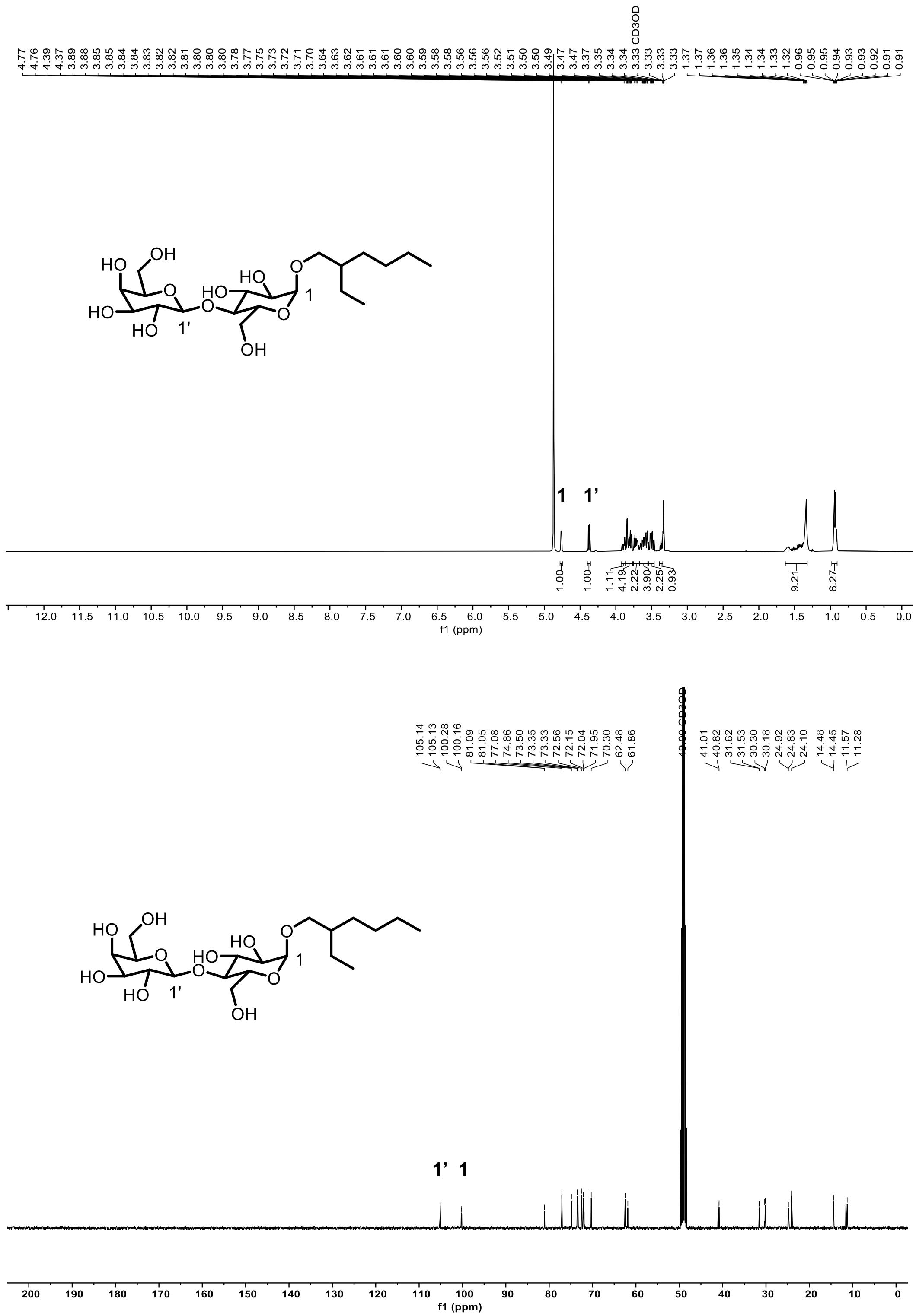

Figure S1. ^{1}H and ^{13}C NMR spectra of α-Lac-C_6C_2 in MeOD at 22 °C.

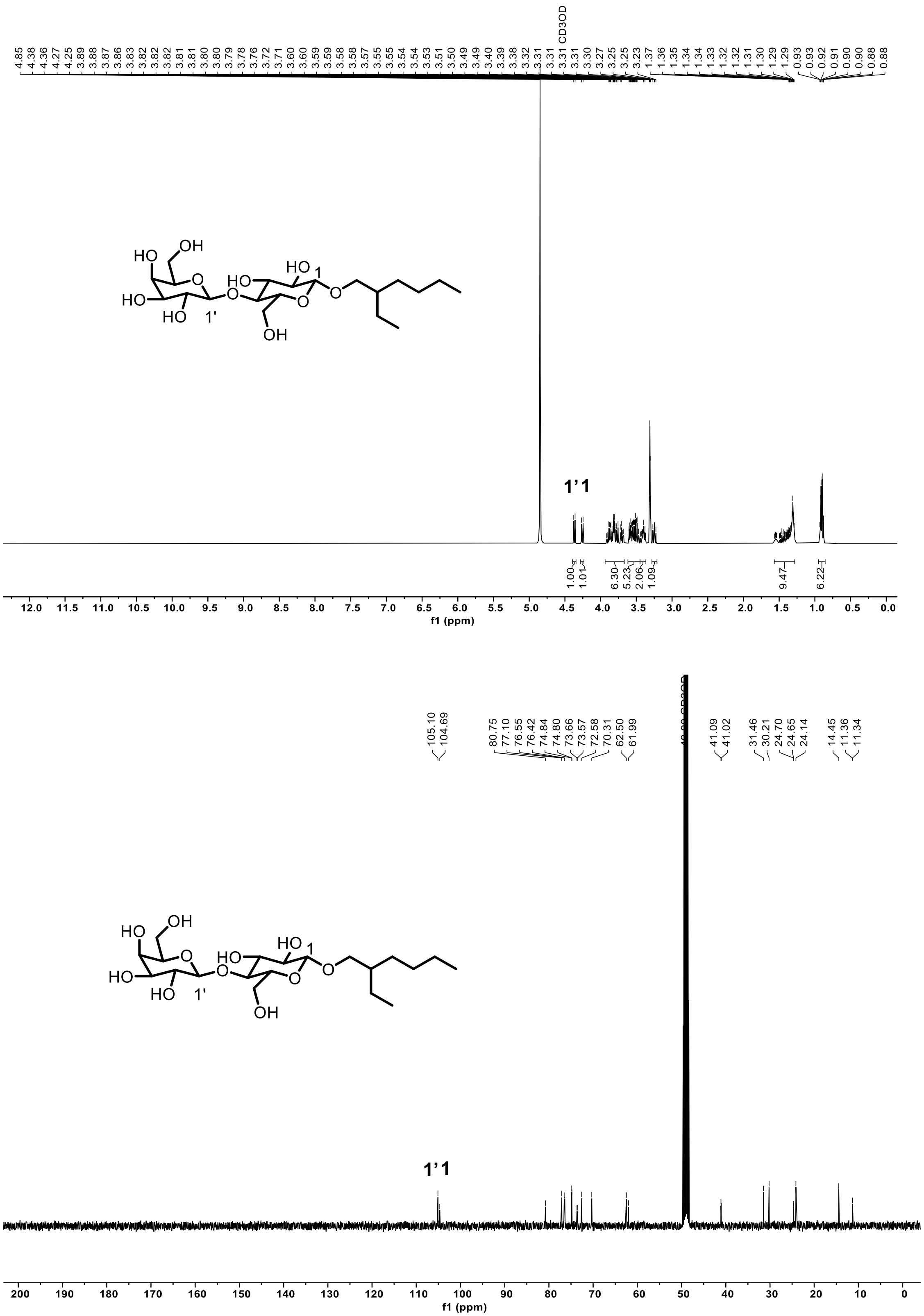

Figure S2. ^{1}H and ^{13}C NMR spectra of β-Lac-C_6C_2 in MeOD at 22 °C.

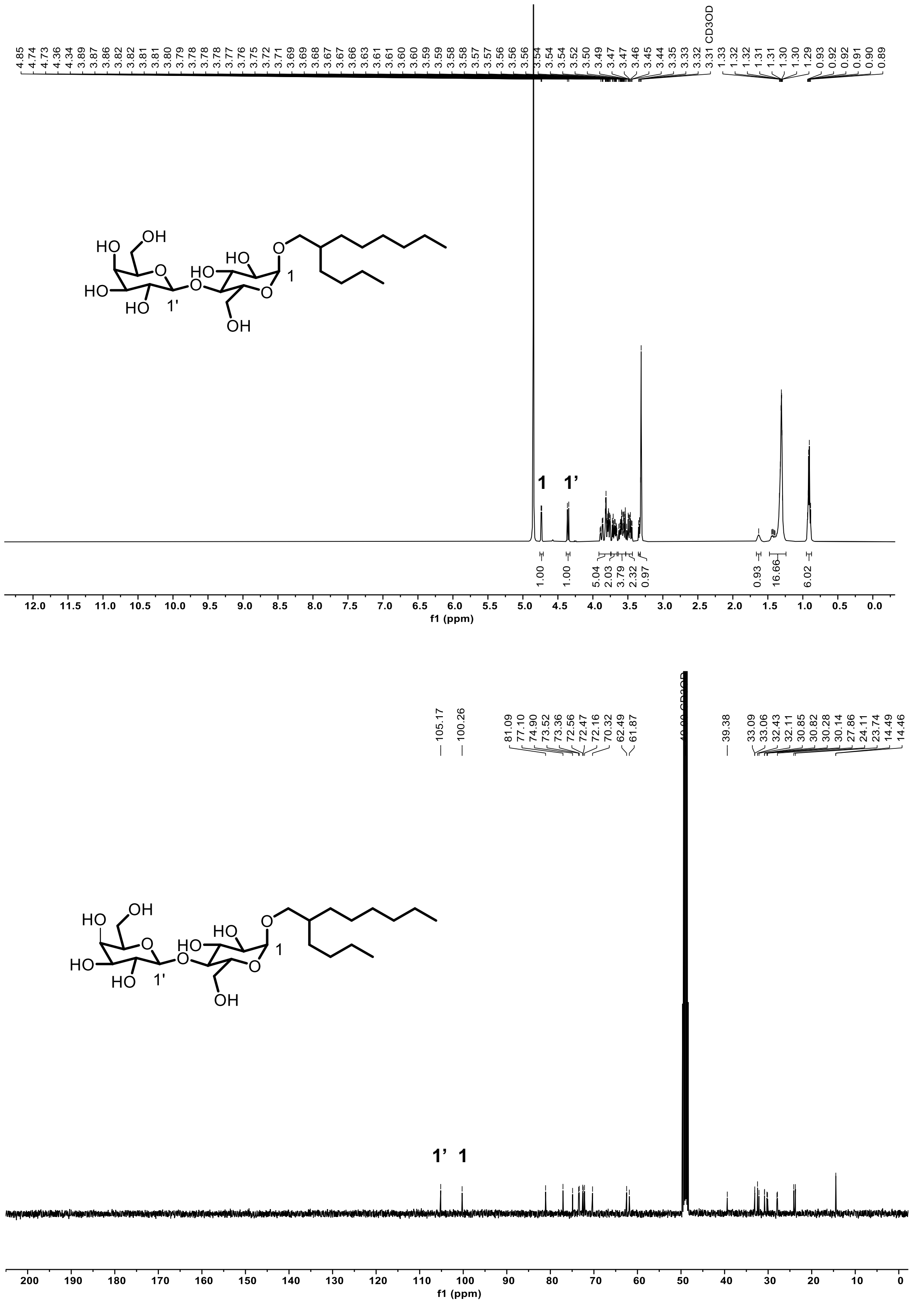

Figure S3. ^{1}H and ^{13}C NMR spectra of α-Lac-C_8C_4 in MeOD at 22 °C.

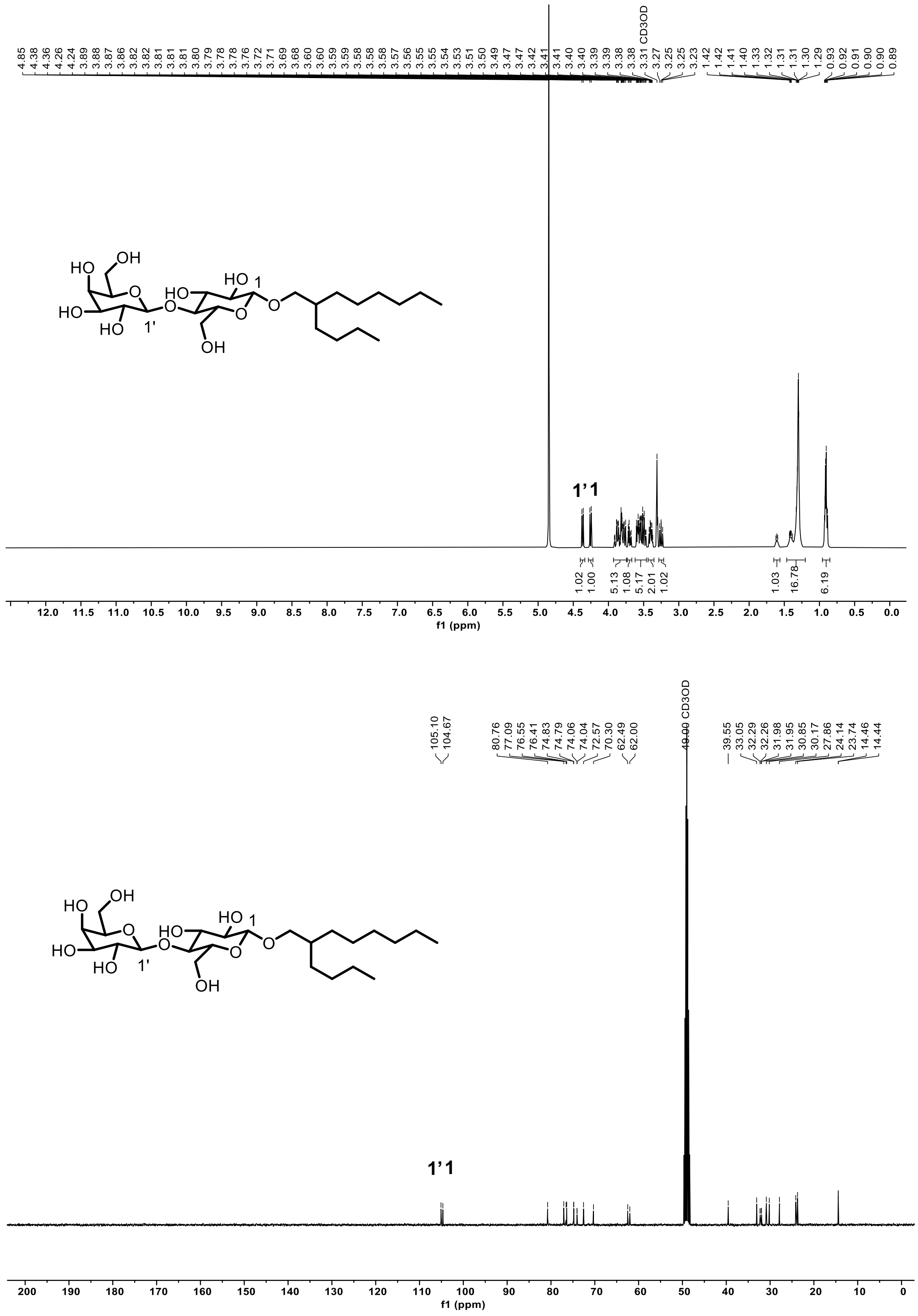

Figure S4. ^{1}H and ^{13}C NMR spectra of *β*-Lac-C_8C_4 in MeOD at 22 °C.

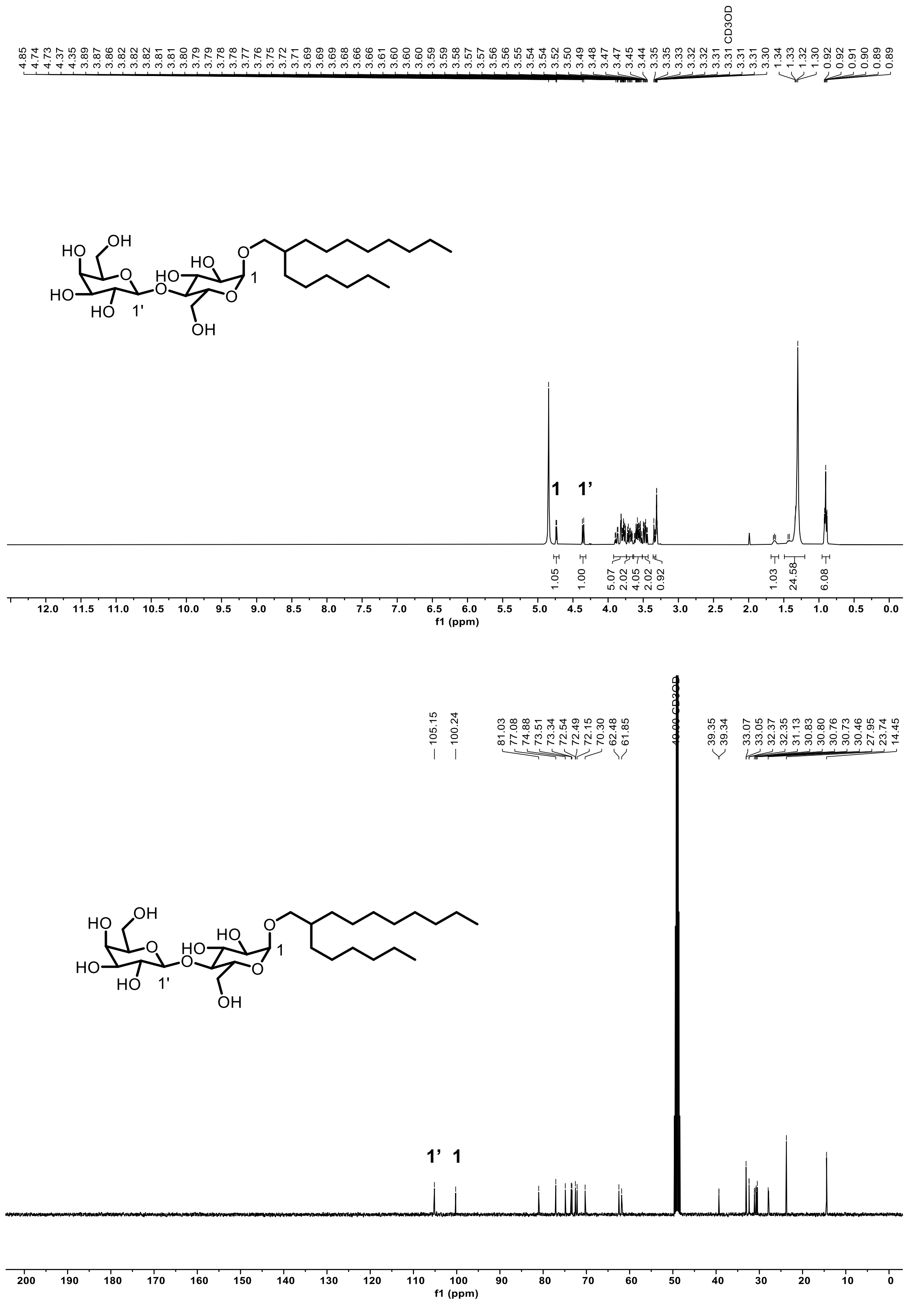

Figure S5. ^{1}H and ^{13}C NMR spectra of α-Lac-$C_{10}C_{6}$ in MeOD at 22 °C.

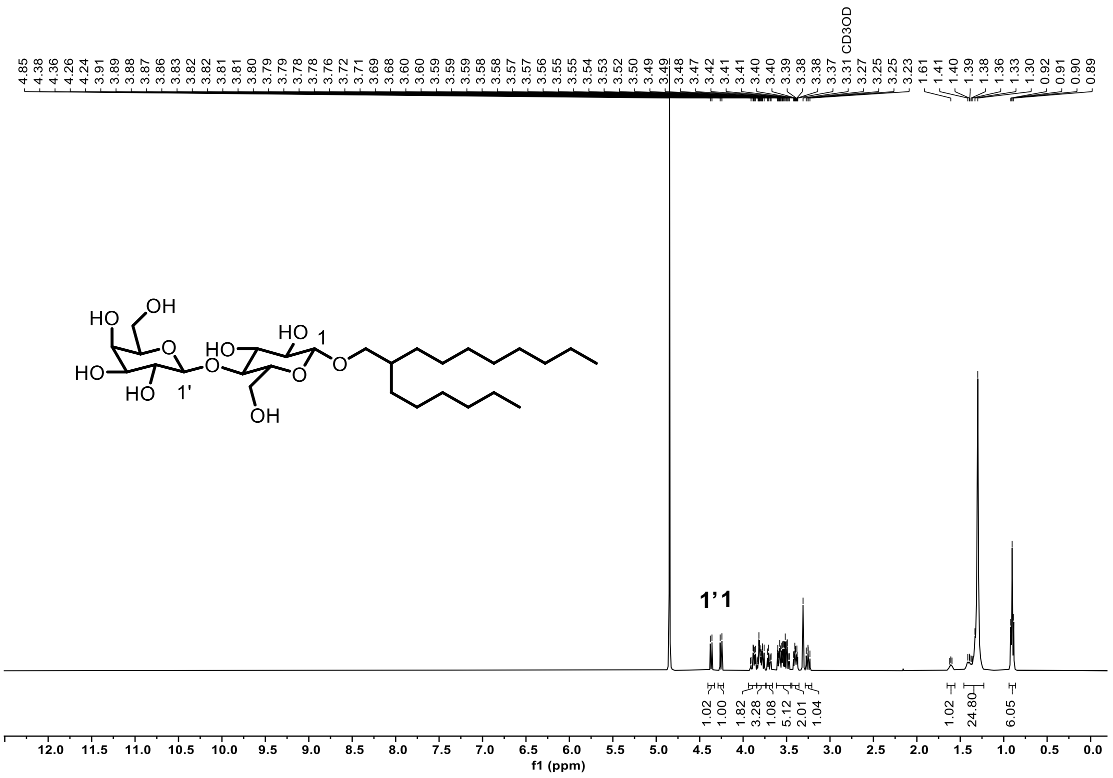

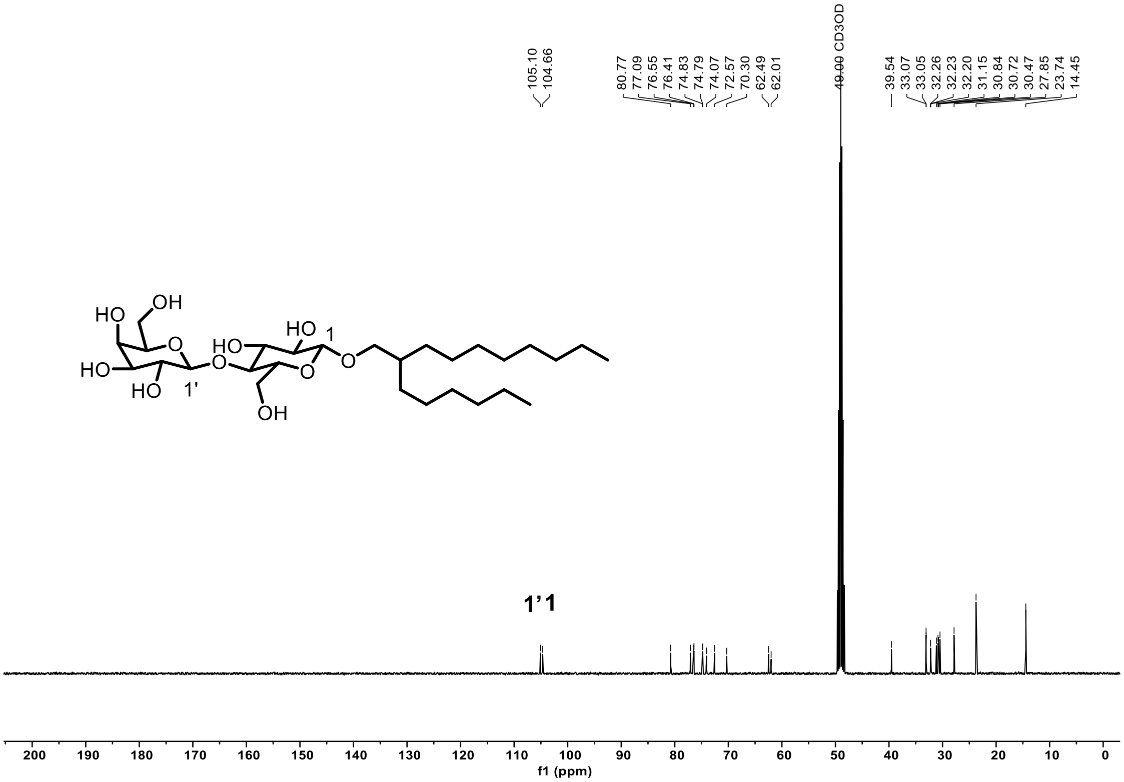

Figure S6. ^{1}H and ^{13}C NMR spectra of *β*-Lac-$C_{10}C_{6}$ in MeOD at 22 °C.

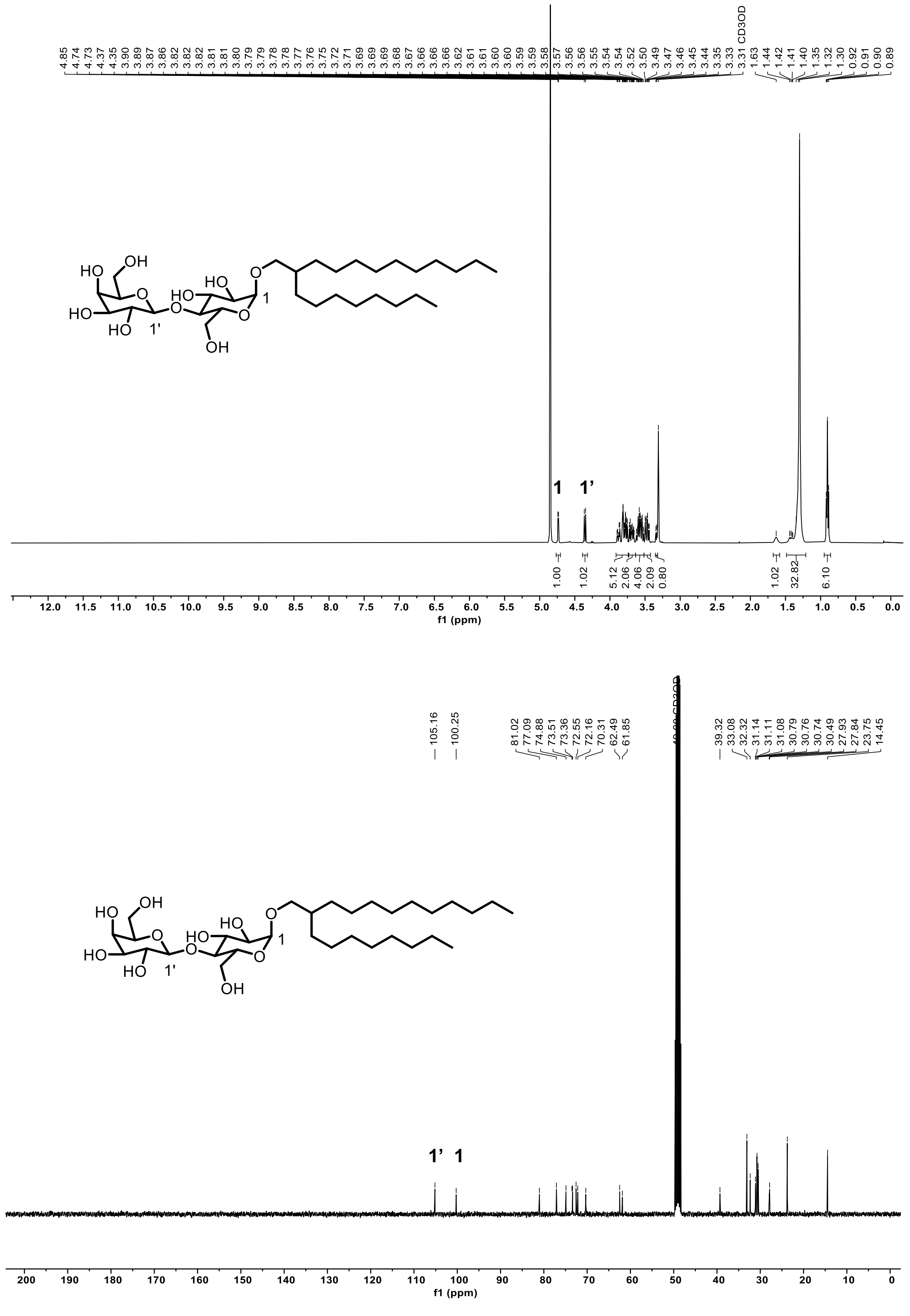

Figure S7. ^{1}H and ^{13}C NMR spectra of α-Lac-C$_{12}$C$_8$ in MeOD at 22 °C.

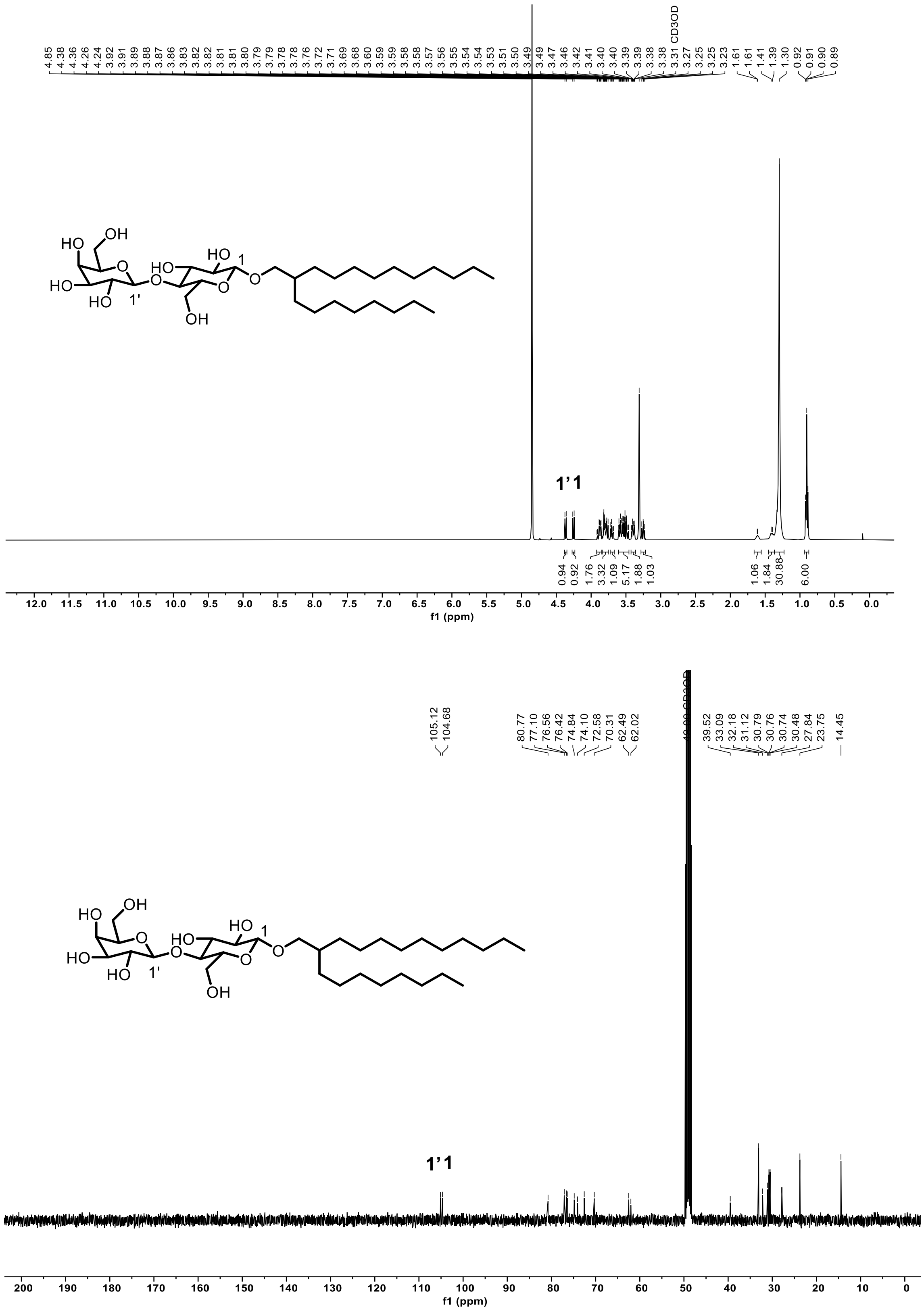

Figure S8. ^{1}H and ^{13}C NMR spectra of *β*-Lac-$C_{12}C_{8}$ in MeOD at 22 °C.

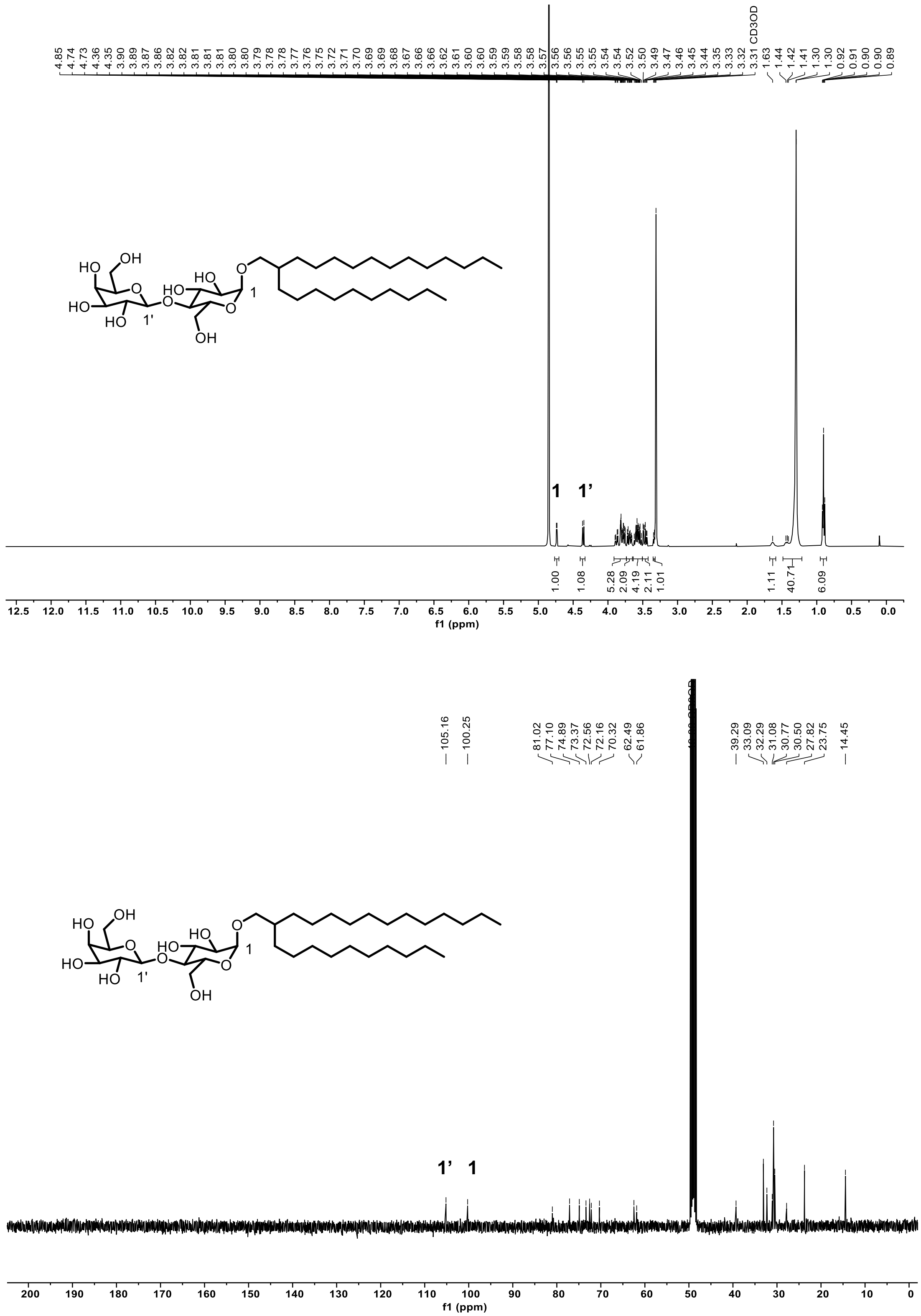

Figure S9. ^{1}H and ^{13}C NMR spectra of α-Lac-C$_{14}$C$_{10}$ in MeOD at 22 °C.

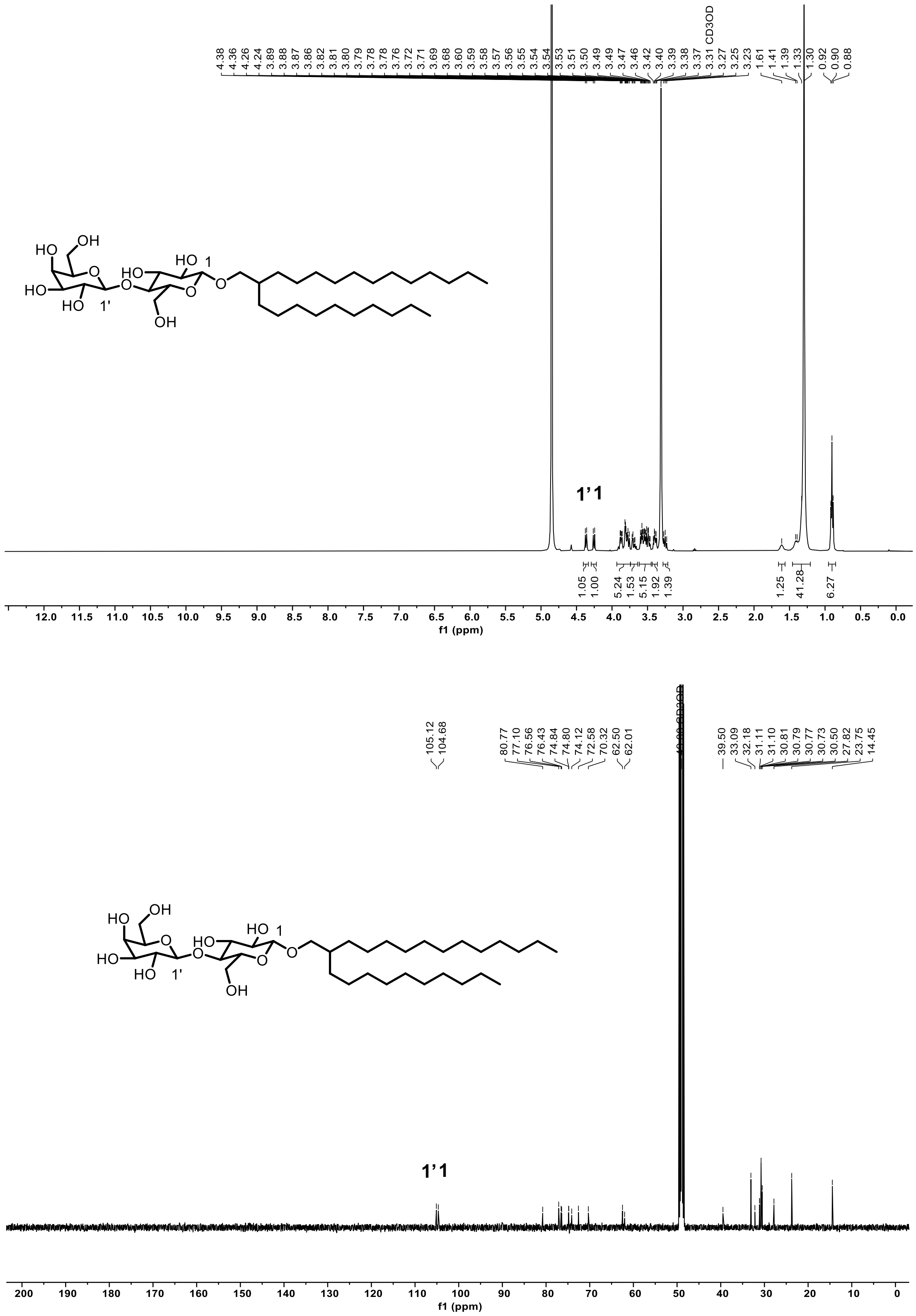

Figure S10. ^{1}H and ^{13}C NMR spectra of β-Lac-$C_{14}C_{10}$ in MeOD at 22 °C.

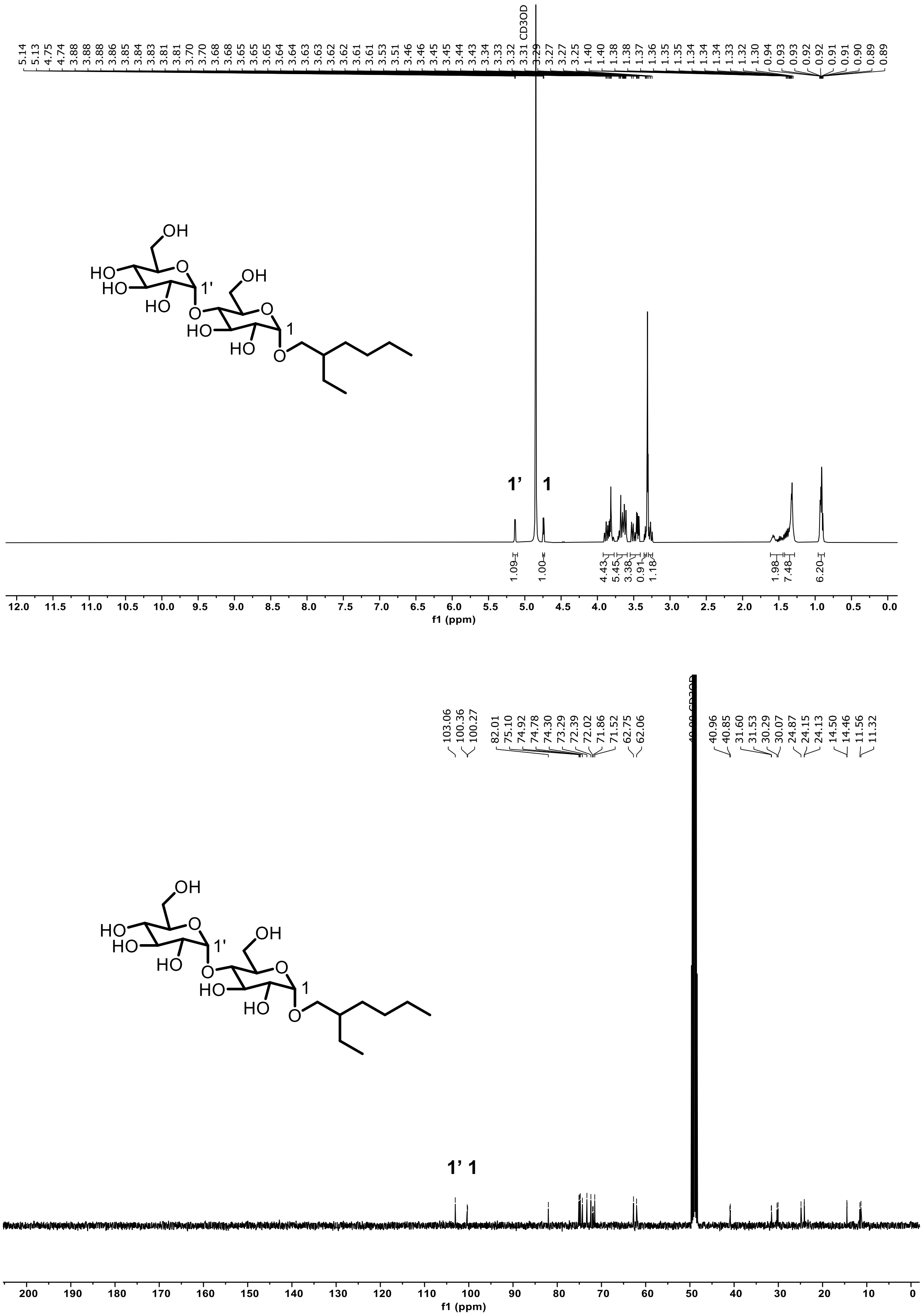

Figure S11. ^{1}H and ^{13}C NMR spectra of α-Mal-C$_6$C$_2$ in MeOD at 22 °C.

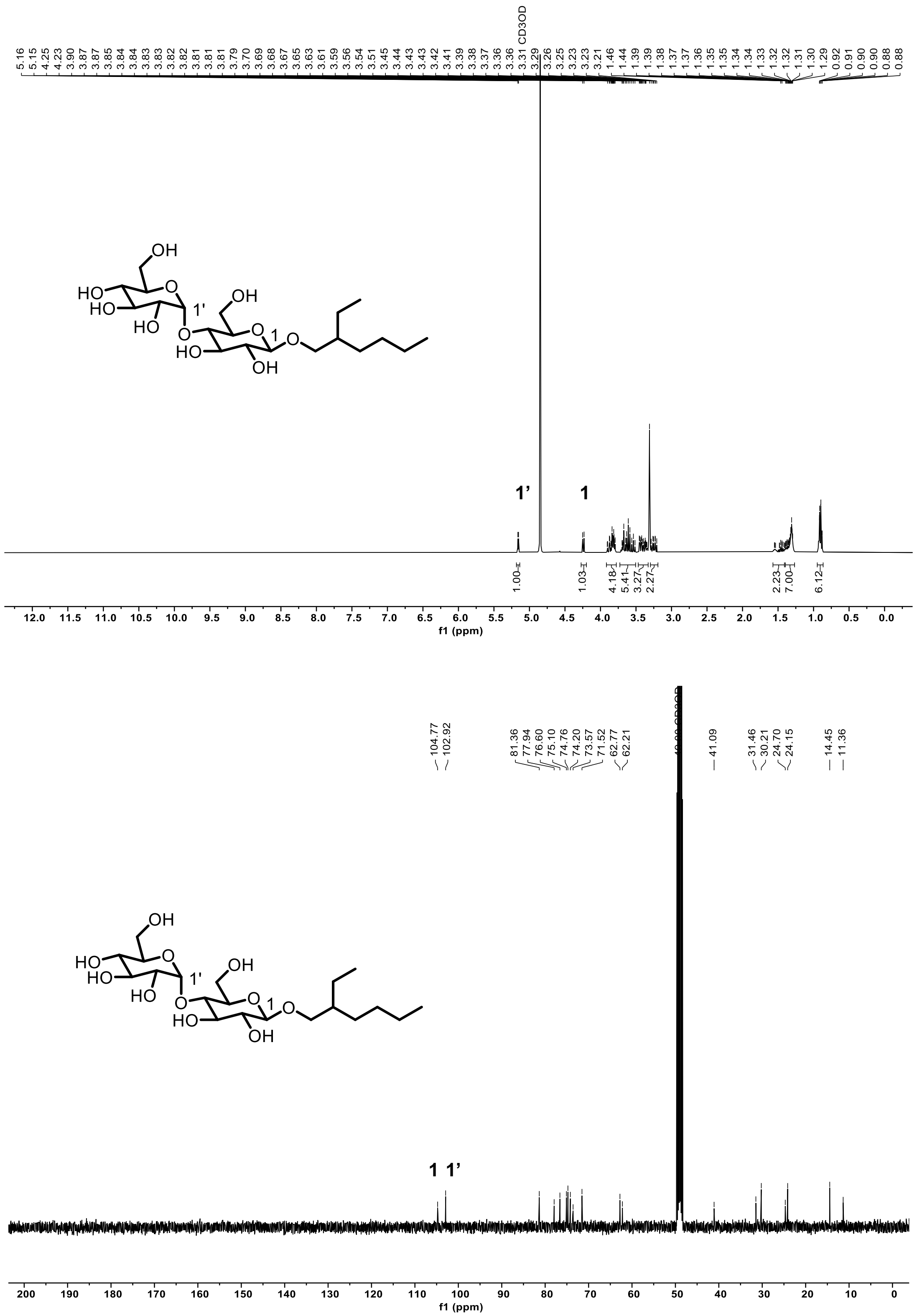

Figure S12. ^{1}H and ^{13}C NMR spectra of β-Mal-C$_6$C$_2$ in MeOD at 22 °C.

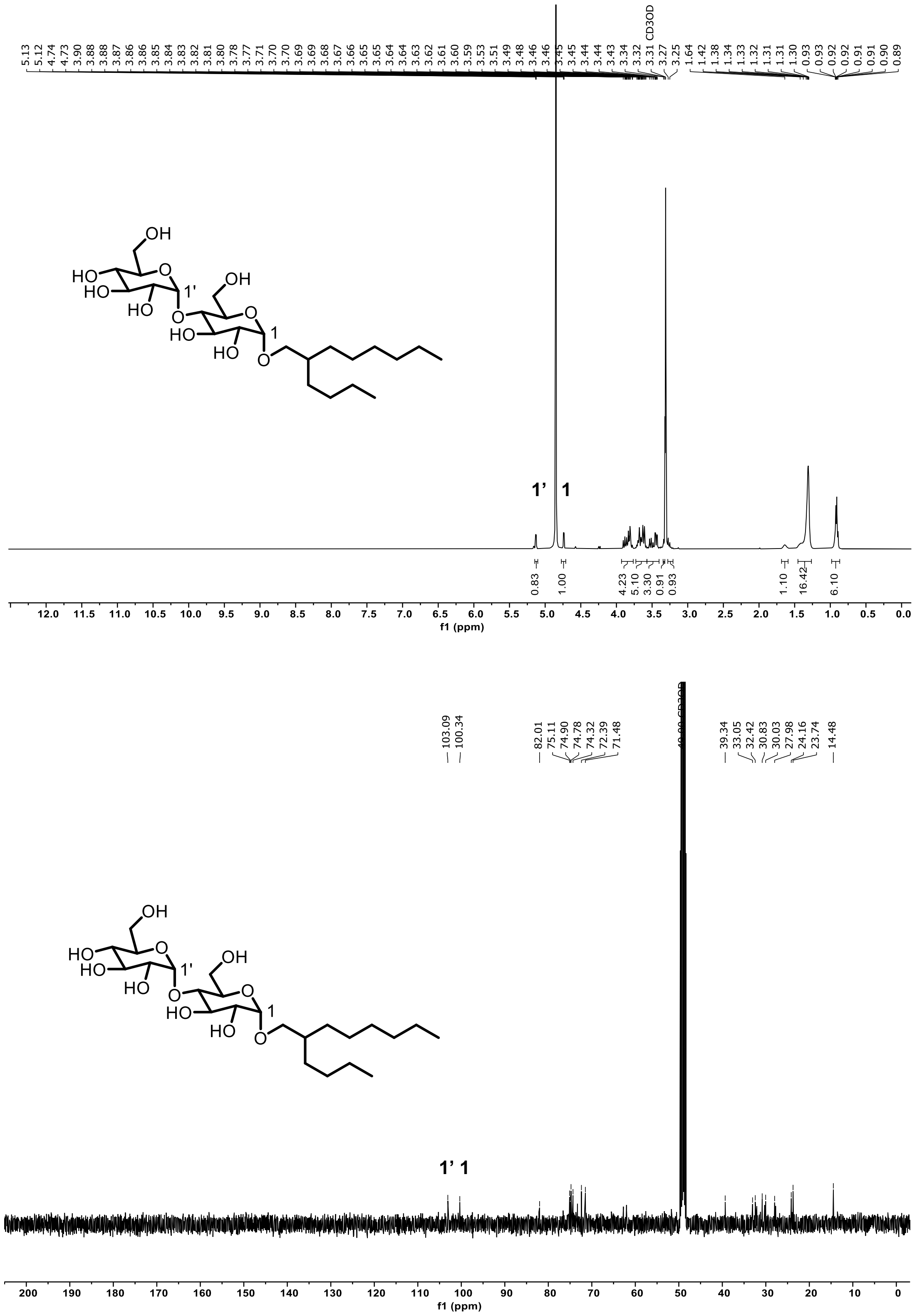

Figure S13. ^{1}H and ^{13}C NMR spectra of α-Mal-C_8C_4 in MeOD at 22 °C.

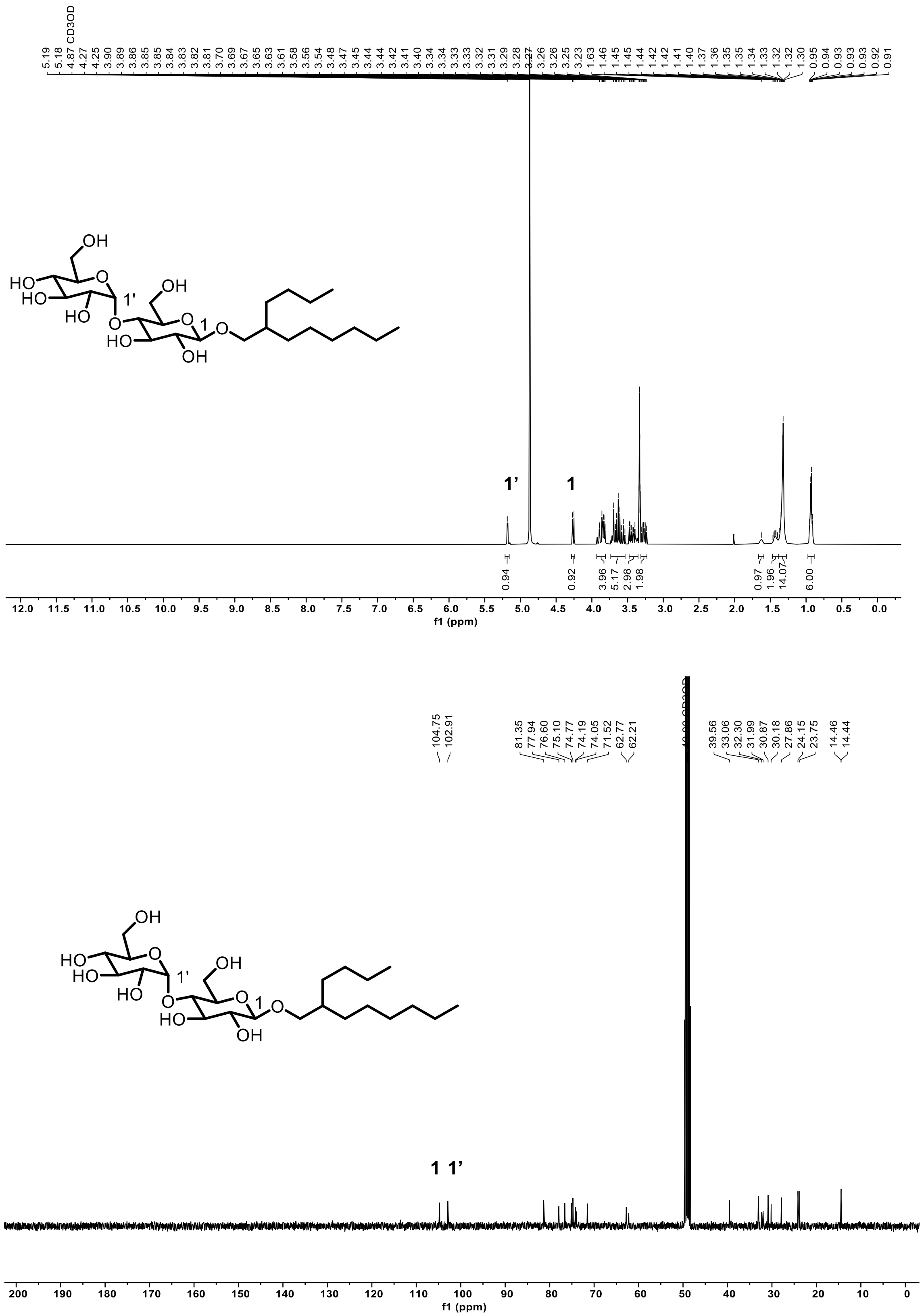

Figure S14. ^{1}H and ^{13}C NMR spectra of *β*-Mal-C_8C_4 in MeOD at 22 °C.

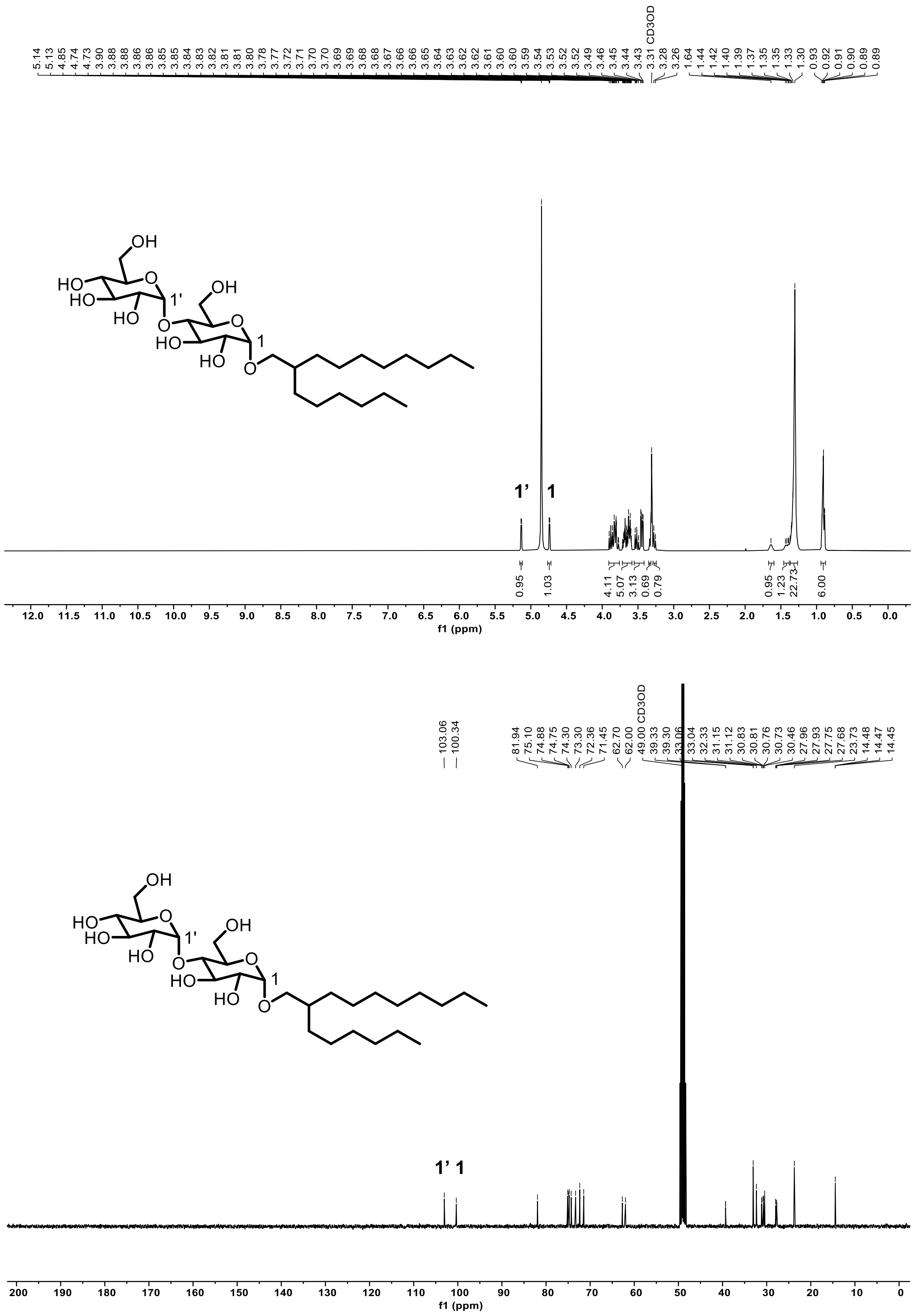

Figure S15. ^{1}H and ^{13}C NMR spectra of α-Mal-C$_{10}$C$_{6}$ in MeOD at 22 °C.

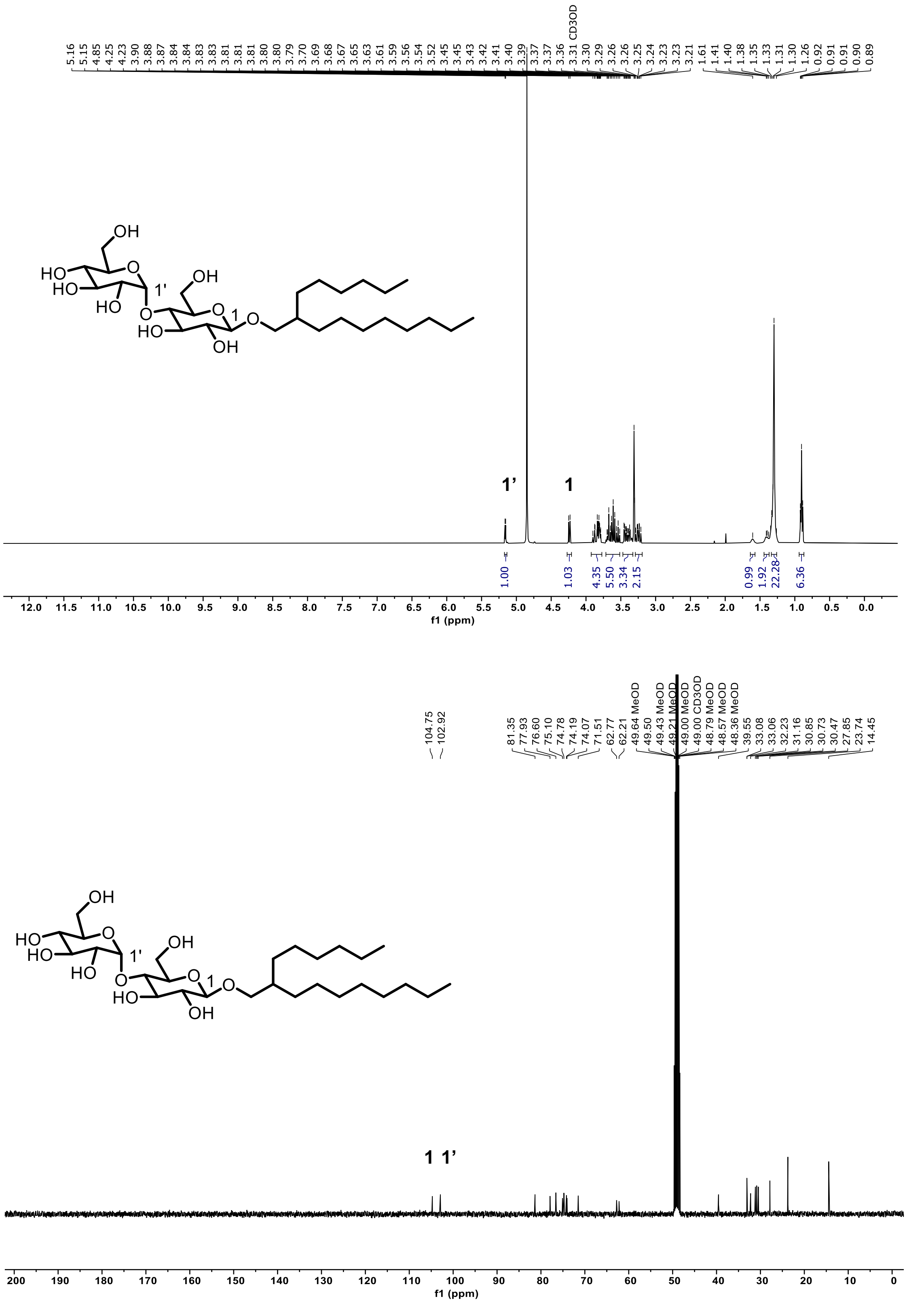

Figure S16. ^{1}H and ^{13}C NMR spectra of *β*-Mal-$C_{10}C_6$ in MeOD at 22 °C.

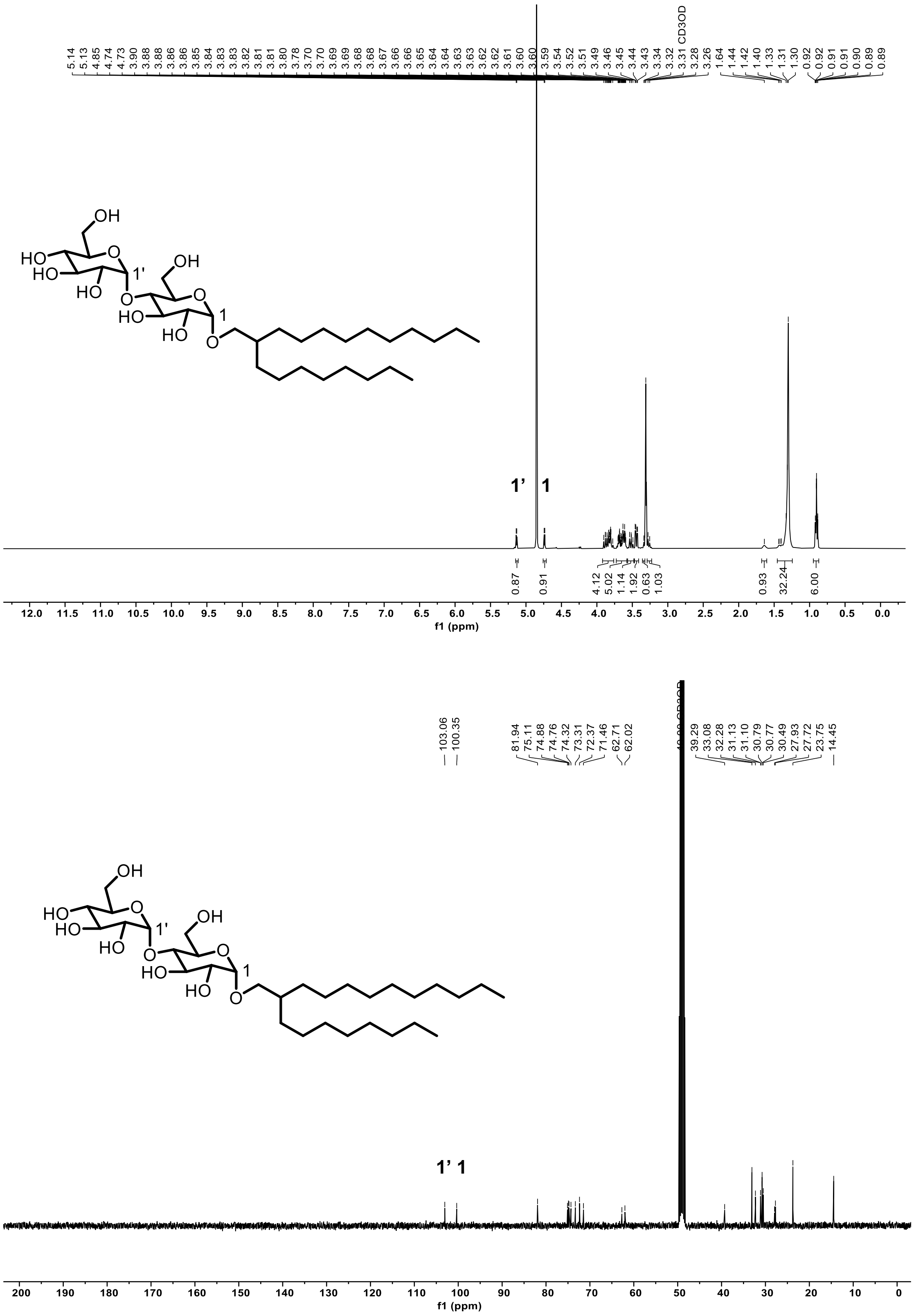

Figure S17. ^{1}H and ^{13}C NMR spectra of α-Mal-$C_{12}C_{8}$ in MeOD at 22 °C.

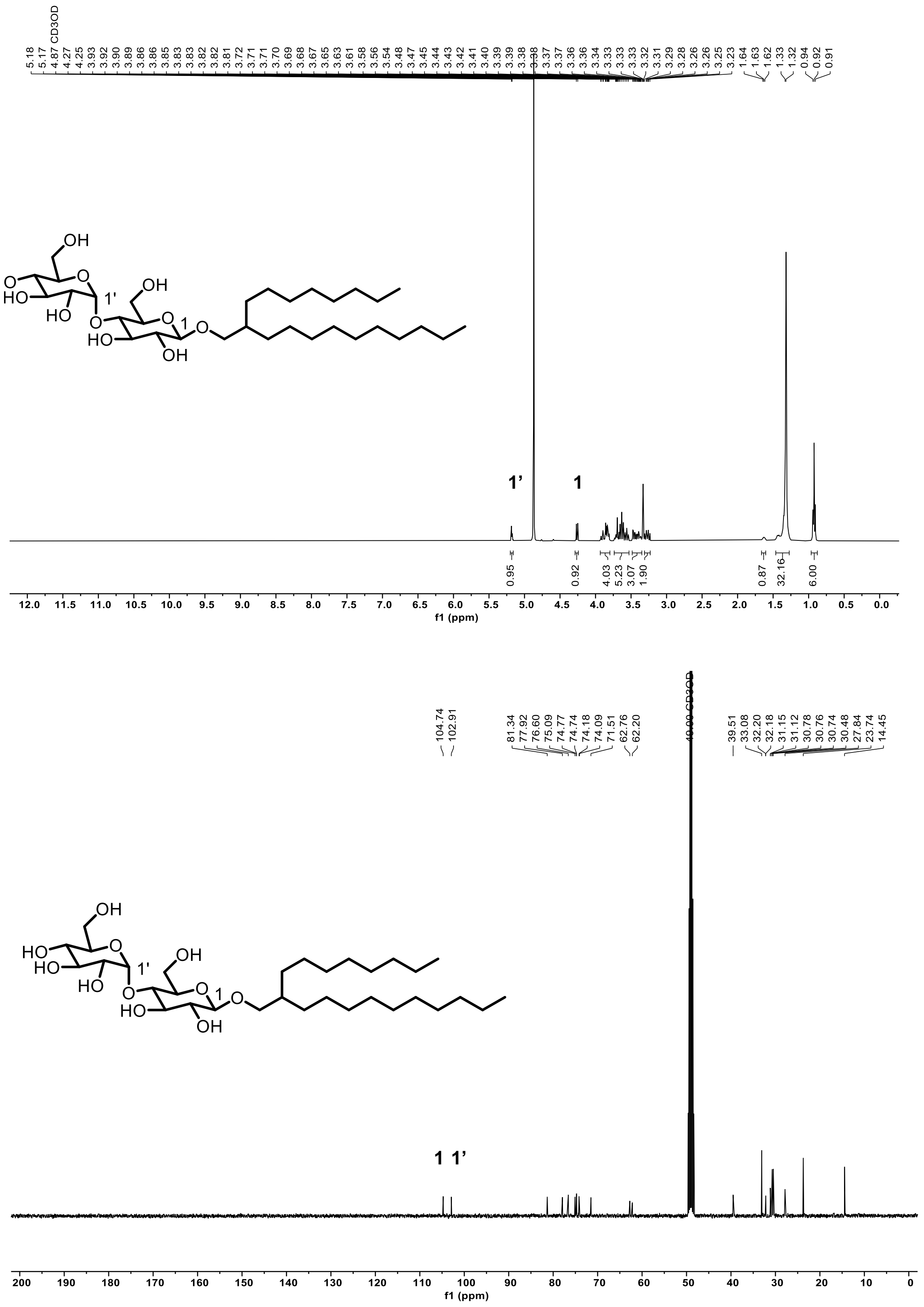

Figure S18. ^{1}H and ^{13}C NMR spectra of *β*-Mal-$C_{12}C_8$ in MeOD at 22 °C.

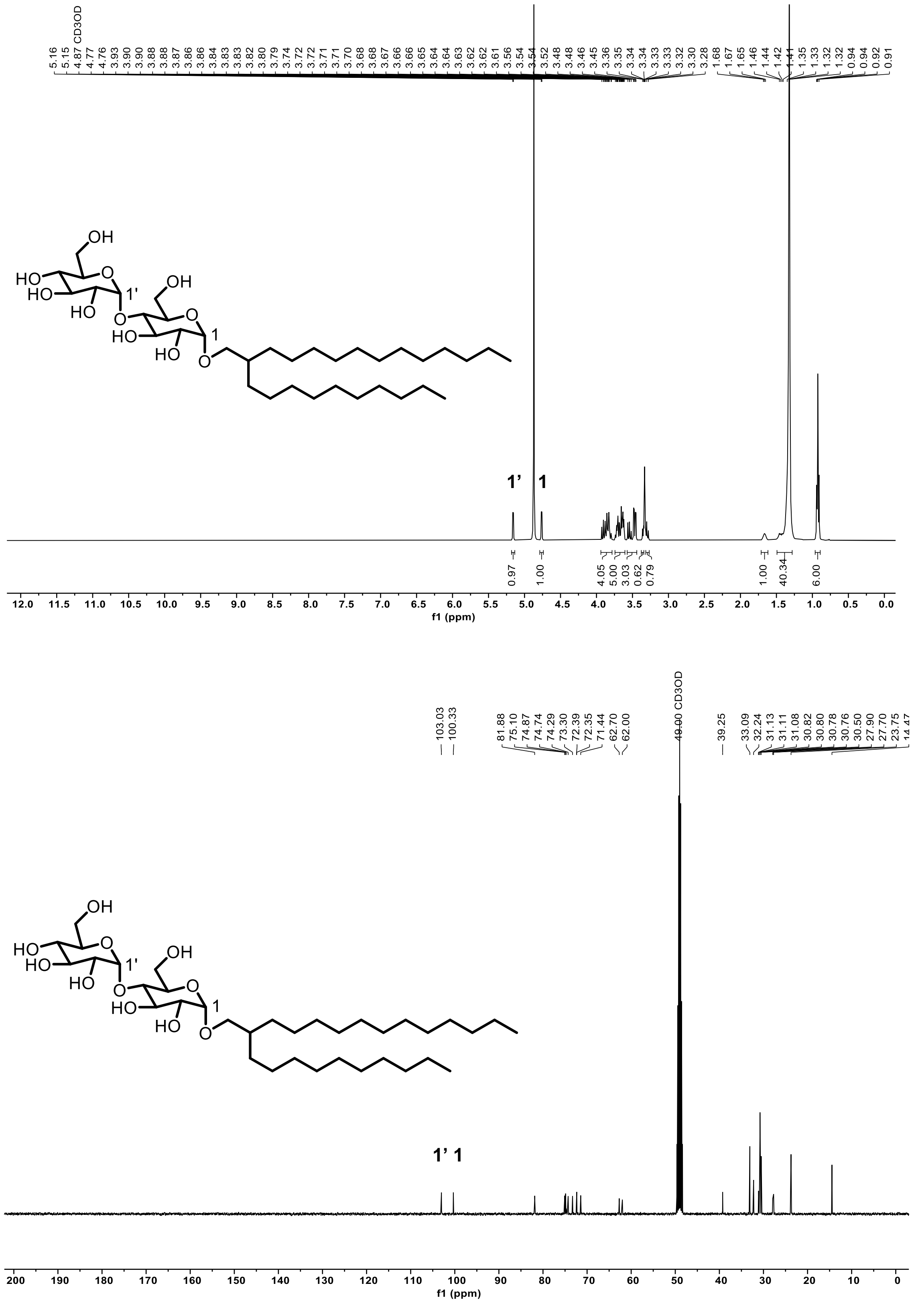

Figure S19. ^{1}H and ^{13}C NMR spectra of α-Mal-C$_{14}$C$_{10}$ in MeOD at 22 °C.

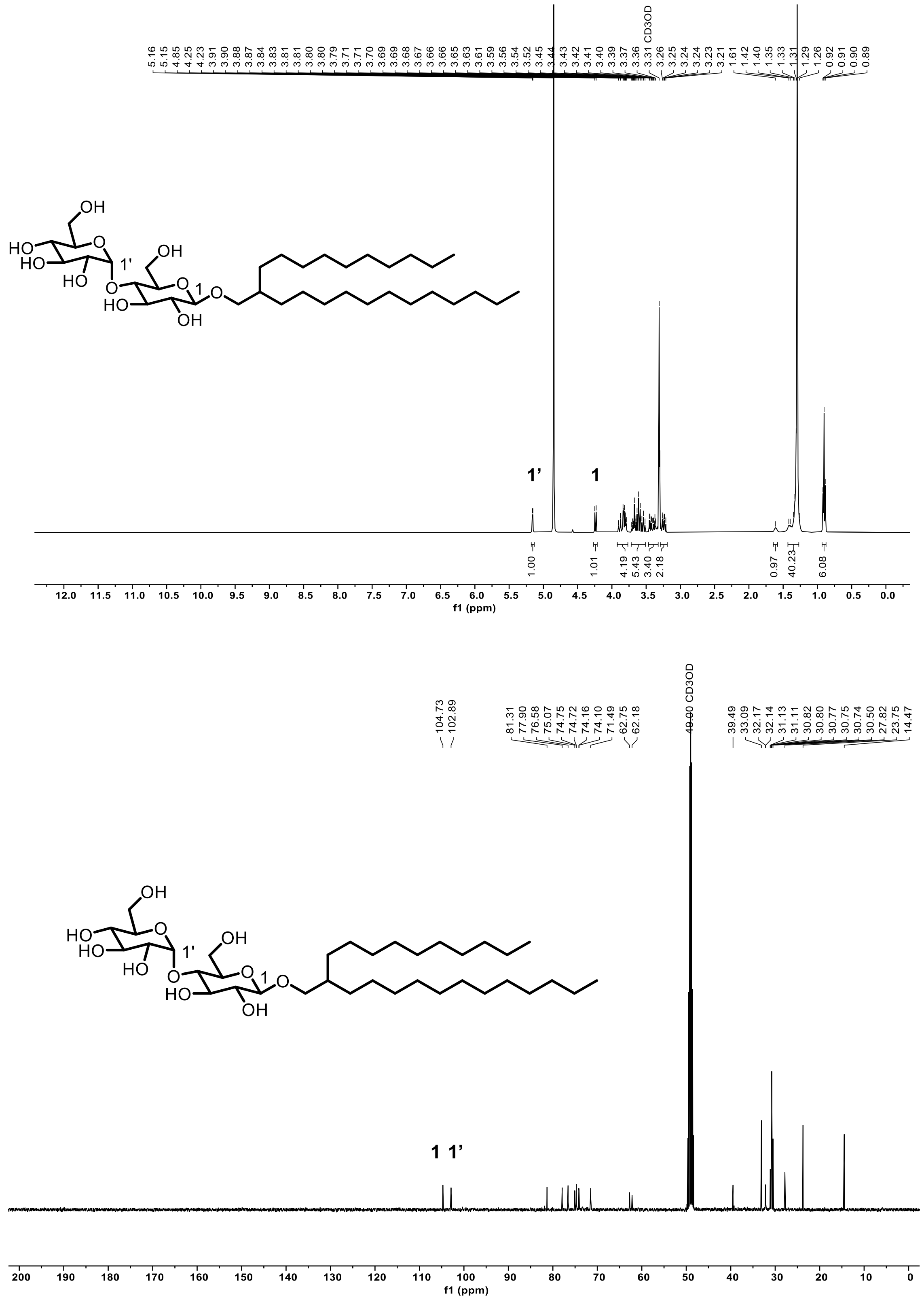

Figure S20. ^{1}H and ^{13}C NMR spectra of *β*-Mal-$C_{14}C_{10}$ in MeOD at 22 °C

X. Characterization of Glycolipid Phase Behavior Using DSC

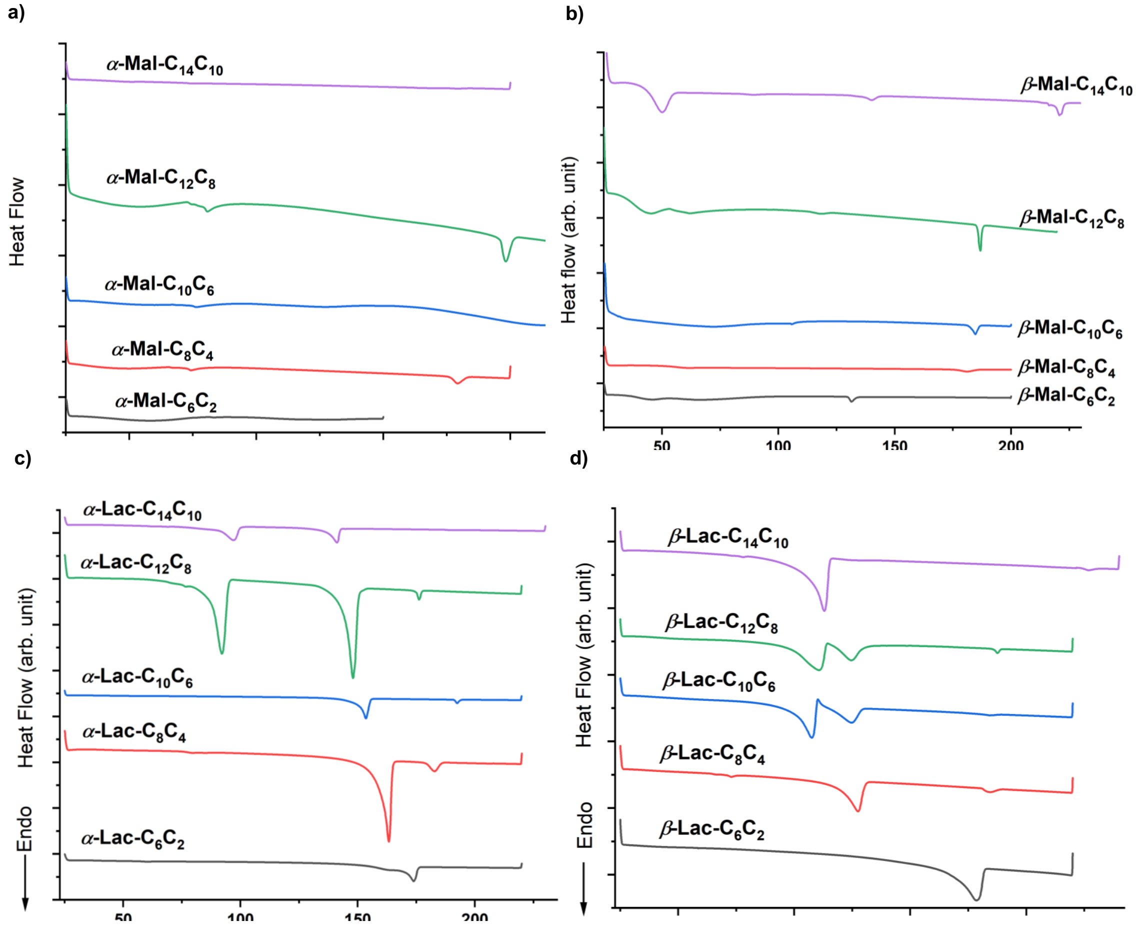

Figure S21. DSC profile of dry a) α-maltosides and b) β- maltosides c) α-lactosides and d) β-lactosides within the temperature range of 25–240 ˚C at a heating scan rate of 5 °C min^{-1}.

The thermotropic phase behavior of glycolipids was initially examined DSC to determine the temperature range for self-assembly. Weak, step-like transitions between $48 \leq T \leq 76$ °C were observed in the DSC thermograms of all Guerbet maltosides during the first heating at 5 °C/min (Figure S21, Table S1). This behavior, commonly associated with a glass transition (T_g), has been previously reported for Guerbet cellobiosides,[27] Guerbet β-maltosides,[2] and other glycolipids.[28] However, no systematic trend in T_g with respect to Guerbet chain length is observed for maltosides, as previously reported.[2, 27] Interestingly, melting transitions are never observed for the maltosides in DSC thermograms (Figure S21) consistent with prior literature.[2] To determine their melting transitions, variable temperature POM was employed with ±5 °C resolution, as previously used for other glycolipids.[7, 27] POM analysis reveals that maltosides begin forming LC phases at $T \geq 70$ °C, depending on the chain length (Table S1). Accordingly, phases at $T < 70$ °C are classified as crystalline (Crys.) for maltosides.

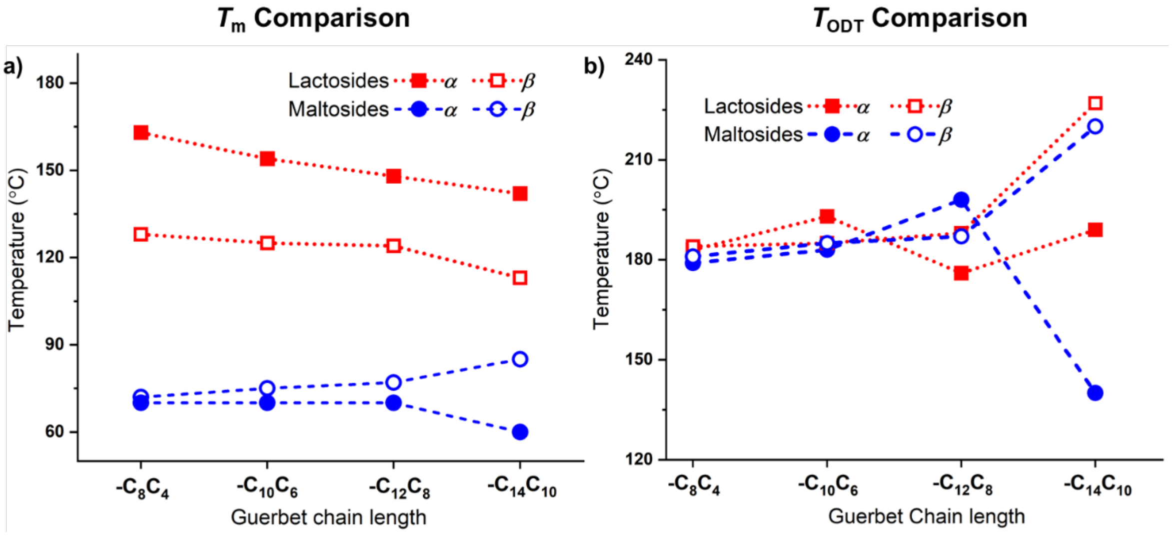

Figure S22. Comparison of transition temperatures between lactosides anomers and maltoside anomers a) melting transition (T_m) and b) order to disorder transition (T_{ODT}) obtained from combined results of DSC, SAXS and POM.

Guerbet lactosides showed no detectable glass transition (T_g) in DSC thermograms but exhibited sharp melting endotherms, indicating a crystal-to-LC transition (Figures S21c,d, Table S1). Notably, in cellobiosides, this melting transition was observed only for α/β-Cel-$C_{14}C_{10}$ and β-Cel-$C_{12}C_8$ via DSC. Additionally, lactosides exhibited significantly higher melting temperatures (113–178 °C) compared to cellobiosides ($T \geq 85$ °C) and maltosides ($T \geq 70$ °C) (Figure S22a). This high T_m has been noted previously in Guerbet β-lactosides,[8] and is largely attributed to the more tightly packed headgroup in lactosides vs. in cellobiosides and maltosides.[8, 29] The ability of lactose headgroups to form stronger intermolecular interactions vs. other sugar heads has been observed before,[30-31] and lactose-based glycolipids can also form crystallite-like tight packings depending upon the hydrophobic/hydrophilic balance.[32] Although all Guerbet lactosides showed a high enthalpy endothermic peak marking crystalline to LC phase transitions, additional endothermic peaks were observed for α-lactosides with -$C_{12}C_8$ and -$C_{14}C_{10}$ tails and β-lactosides for -$C_{10}C_6$ and -$C_{12}C_8$ tails (Figure S21c,d). Typically, the first endothermic peak at lower temperatures (within 92–110 °C) corresponds to changes in hydrophobic chain packing, while the second peak at higher temperatures (within 124–148 °C) marks the crystal-to-LC transition

Thermal Transitions in Lactosides:

In the β-lactosides, the formation of a crystalline lamellar phase (L_C) at room temperature was disclosed through corresponding wide-angle X-ray scattering (WAXS) peaks at 4.5, 3.8, and 3.4 Å (Figure S23).[32-34] The β-lactosides experienced a shift in their assembly pattern at 107 °C (for -$C_{10}C_6$) and 110 °C (for -$C_{12}C_8$), as indicated by the initial endotherms in their respective DSC profiles. Detailed analysis of their SAXS data unveiled that at these temperatures the glycolipids were forming a coexistence of two lamellar phases for β-$C_{10}C_6$ and a coexistence of lamellar and gyroid for β-$C_{12}C_8$ with a change in lamellar spacing from 20.2 to 26.2 for -$C_{10}C_6$ and from 22.8 to 29.8 for -$C_{12}C_8$. Despite these changes, their WAXS profile still consists of sharp peaks confirming a crystalline state. Upon further temperature increase, both transitioned from a crystalline to an LC phase, marked by the appearance of a broad peak in their WAXS at 124 ˚C. Like the β-lactosides, characteristic SAXS and WAXS peaks (Figure S24) affirmed the formation of a crystalline lamellar (L_C) phase for both α-$C_{12}C_8$ and α-$C_{14}C_{10}$ lactosides. The dominant scattering peak at 4.6 in their WAXS profile indicated triclinic packing mode of lipid chains, in the L_C phase.[33, 35] The initial endothermic peak at 97 °C (for -$C_{14}C_{10}$) and 92 °C (for -$C_{12}C_8$) in their DSC profiles did not correspond to any morphological change evident from SAXS and WAXS patterns. However, sharp peaks in WAXS confirmed their crystallinity, along with a noticeable change in lamellar *d*-spacing. Additionally, a new sharp peak at 4.3 Å appeared in their WAXS pattern, accompanied by two weak peaks, indicating a change in hydrophobic chain packing with a more complex arrangement.[32] Finally, the second endotherms at 141 °C (for -$C_{14}C_{10}$) and 148 °C (for -$C_{12}C_8$) corresponded to the crystal-to-LC transition, evidenced by a broad peak in the WAXS pattern of α-$C_{14}C_{10}$ lactosides and melting observed in POM.

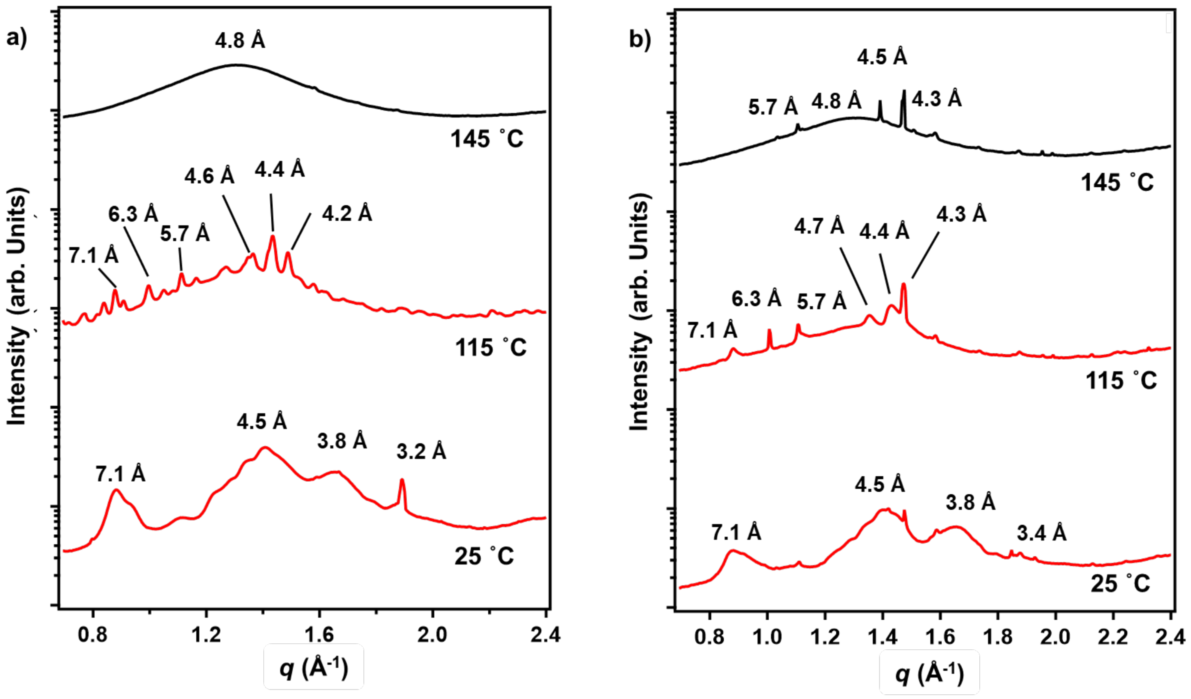

Figure S23. WAXS profile of a) β-Lac-$C_{10}C_6$ and b) β- Lac-$C_{12}C_8$ at temperature 25, 115 and 145 ˚C.

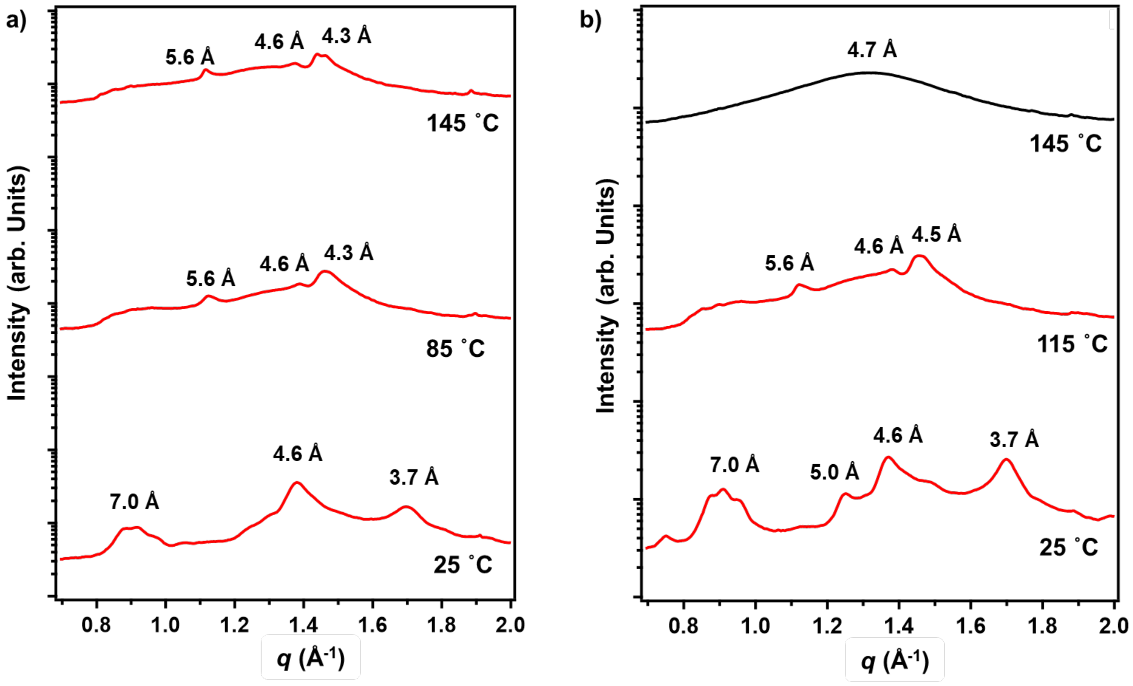

Figure S24. WAXS profile of a) α-Lac-$C_{12}C_8$ and b) α- Lac-$C_{14}C_{10}$ at temperature 25, 115 and 145 °C.

XI. T_g values for maltosides and T_m, T_{ODT} values of lactosides and maltosides

Table S2. T_g and T_m and T_{ODT} of maltosides and lactosides in °C

Guerbet Chains	Maltosides T_g		Maltosides				Lactosides#			
	α-anomer	β-anomer	α-anomer		β-anomer		α-anomer		β-anomer	
			T_m*	T_{ODT}	T_m*	T_{ODT}	T_m	T_{ODT}	T_m	T_{ODT}
-C_6C_2	-	60	-	80	85	132	-	174	-	178
-C_8C_4	72	59	70	179	72	181	163	183	128	184
-$C_{10}C_6$	74	57	70	183*	75	185	154	193	125	185
-$C_{12}C_8$	76	50	70	198	77	187	148	176	124	188
-$C_{14}C_{10}$	-	48	60	140*	85	220	142	189	113	227

***Measured by POM, # Measured by DSC**

XII. Variable Temperature SAXS Profiles of Maltose-based Glycolipids

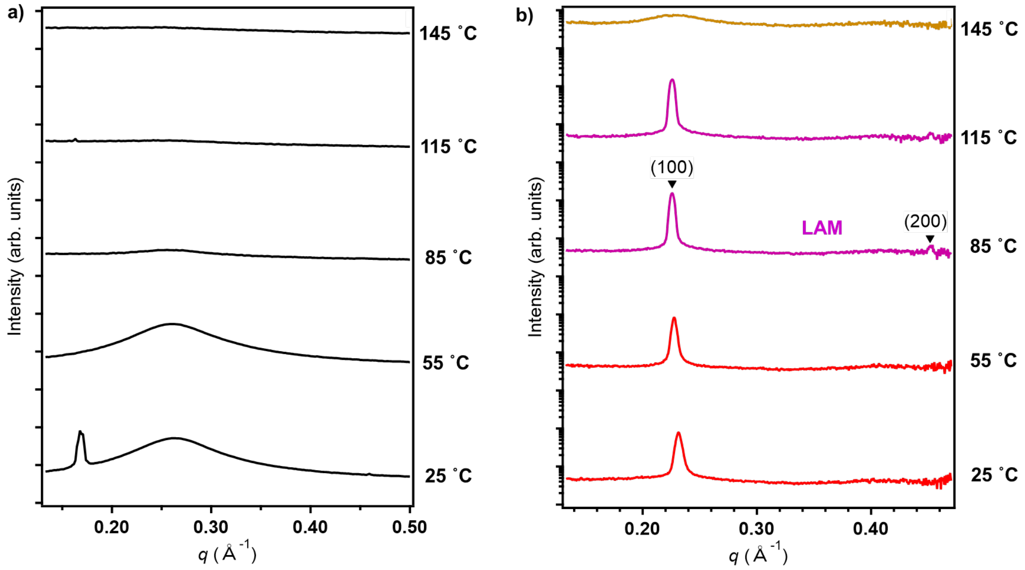

Figure S25. SAXS profile of a) α-Mal-C_6C_2 and b) β- Mal-C_6C_2 within the temperature range of 25-145 °C.

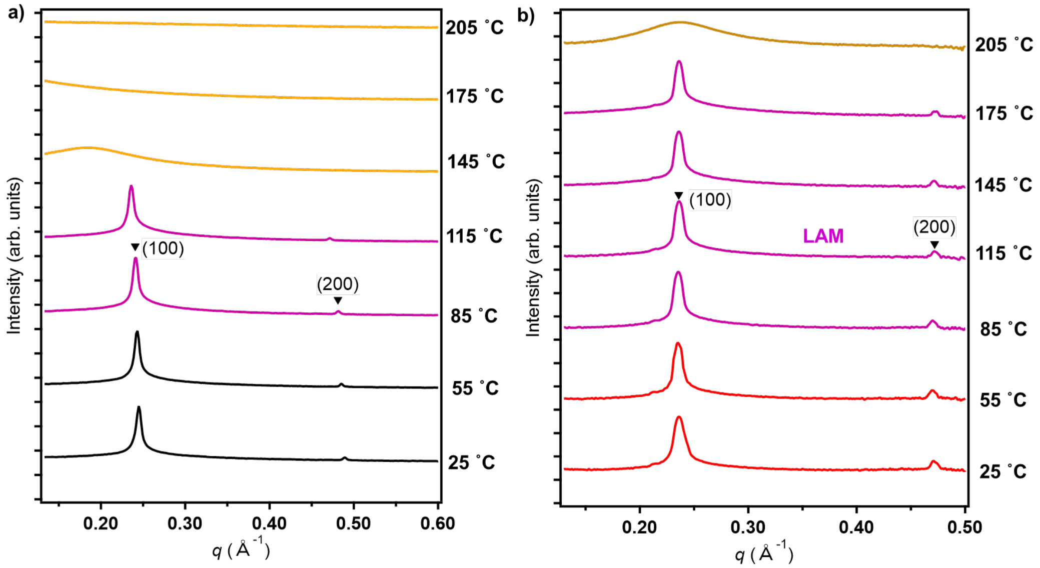

Figure S26. SAXS profile of a) α-Mal-C_8C_4 and b) β-Mal-C_8C_4 within the temperature range of 25-205 °C.

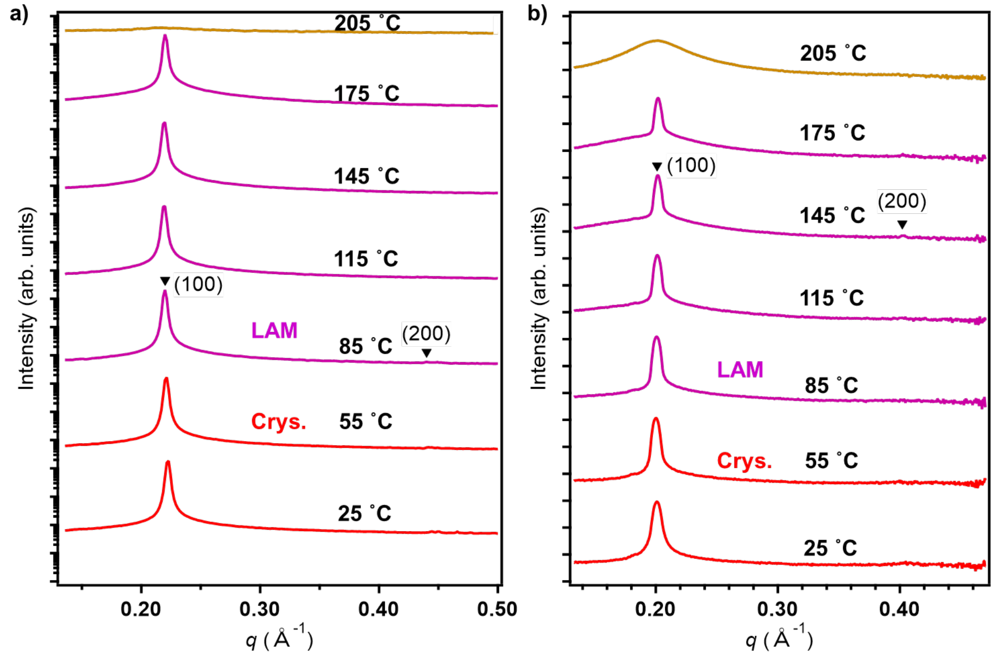

Figure S27. SAXS profile of a) α-Mal -$C_{10}C_6$ and b) β-Mal -$C_{10}C_6$ within the temperature range of 25-205 °C

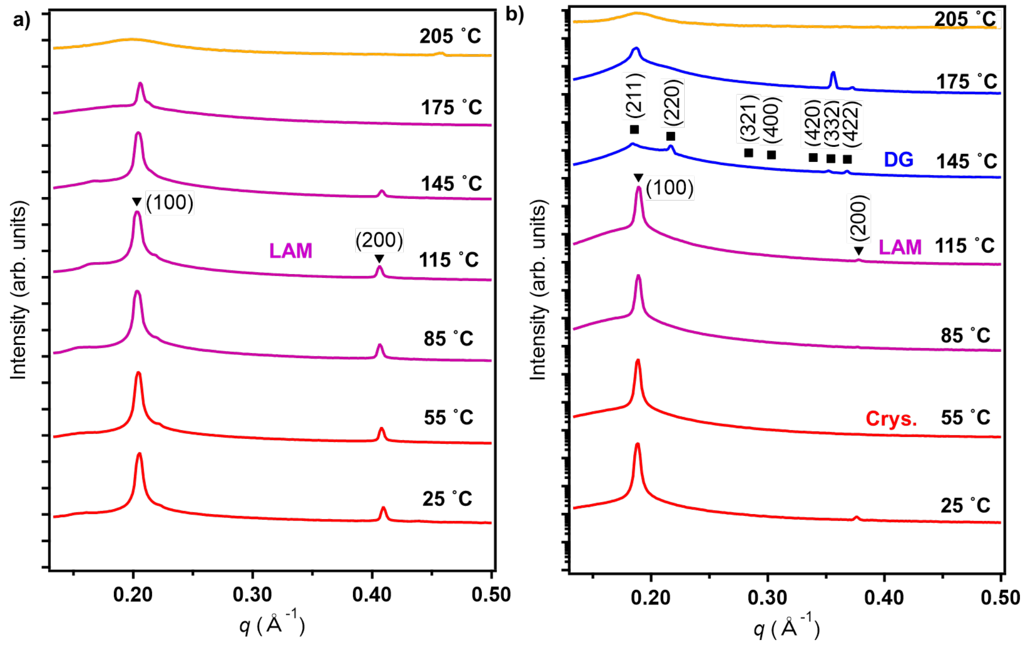

Figure S28. SAXS profile of a) α-Mal-$C_{12}C_8$ and b) β-Mal-$C_{12}C_8$ within the temperature range of 25-205 °C.

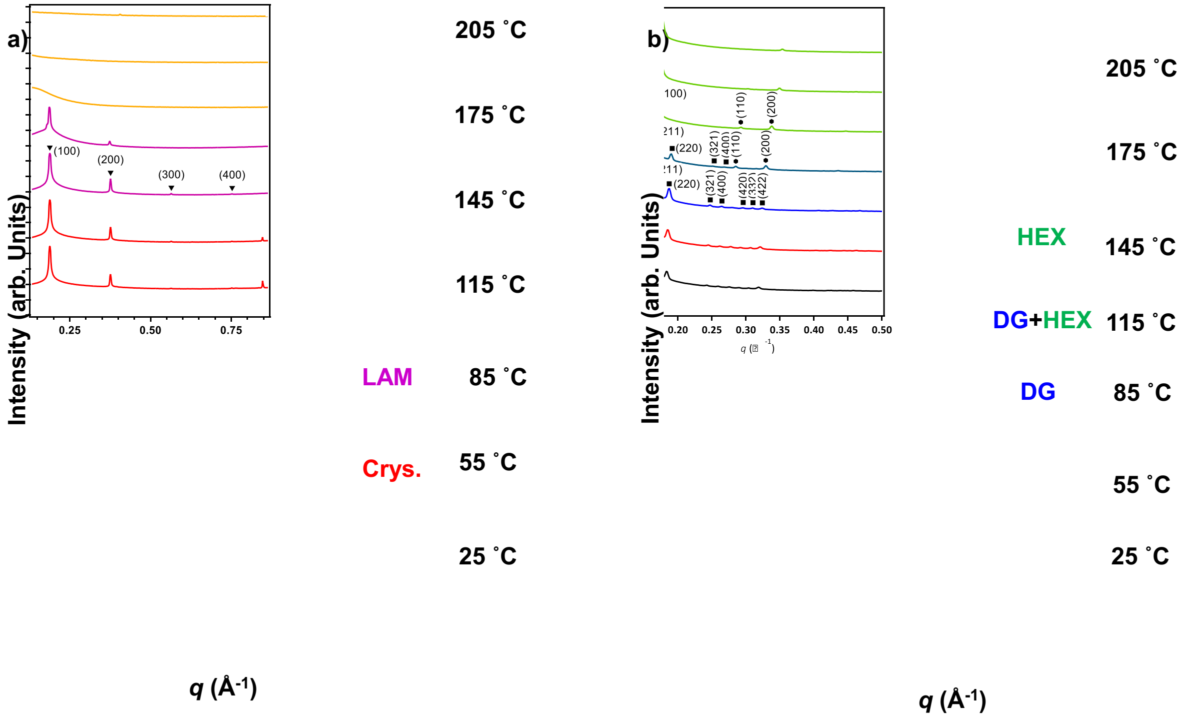

Figure S29. SAXS profile of a) α-Mal-$C_{14}C_{10}$ within the temperature range of 25-185 °C and b) β-Mal-$C_{14}C_{10}$ within the temperature range of 25-205 °C.

XIII. POM images of Guerbet maltosides

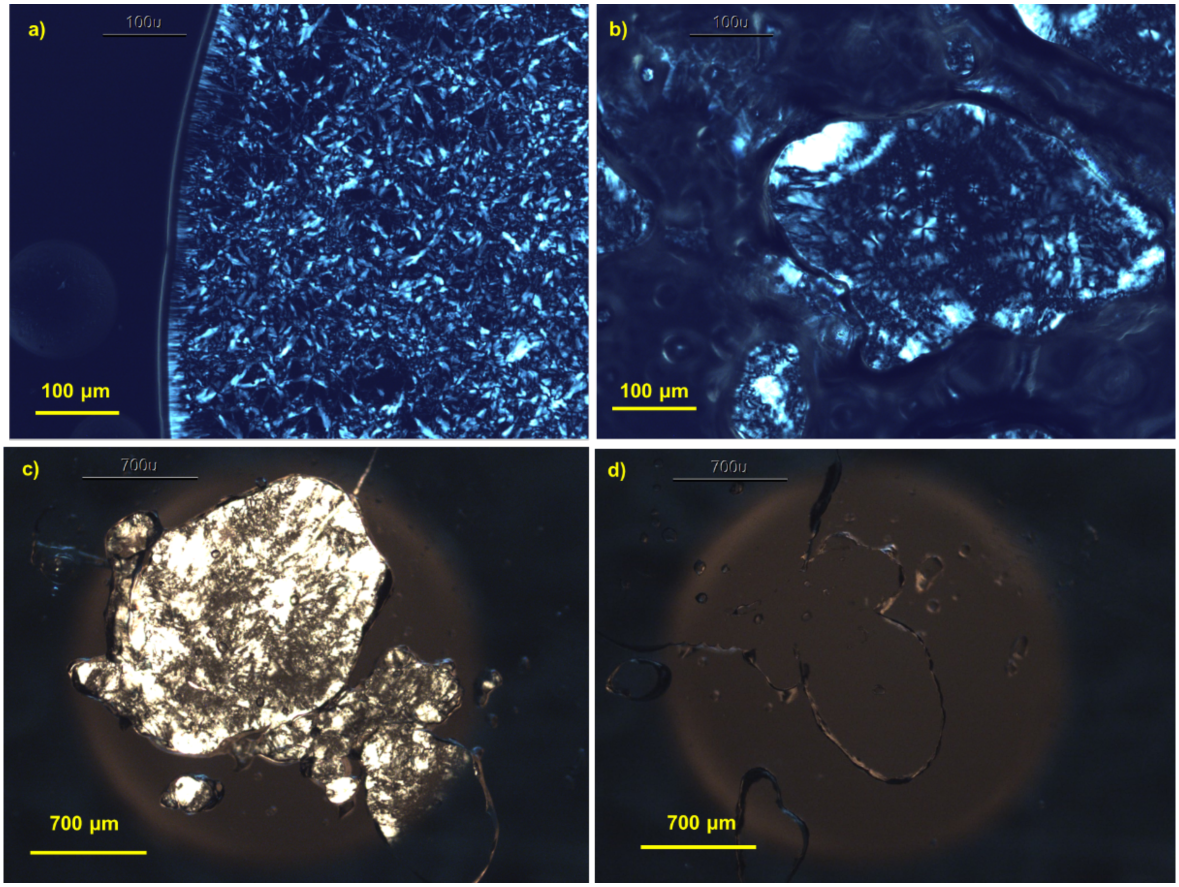

Figure S30. POM images of a) β-Mal-C_6C_2 at 114 ˚C during cooling showing fan-shaped textures representing LAM phase b) α-Mal-$C_{10}C_6$ at 145 ˚C during heating showing focal conics representative of Smectic A phase, c) β-Mal-$C_{12}C_8$ during heating at 113 ˚C showing birefringence, d) β-Mal-$C_{12}C_8$ during heating at 120 ˚C showing isotropic viscous solution representative of cubic phase.

XIV. 1D SAXS of β-Mal-$C_{12}C_8$ during cooling

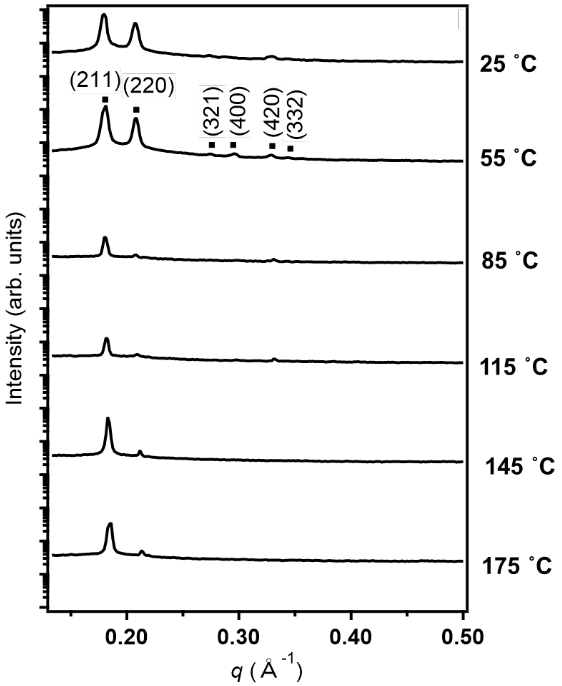

Figure S31. SAXS profile of β-Mal-$C_{12}C_8$ after cooling from an isotropic melt state.

XV. 2D-SAXS Patterns of the Glycolipids

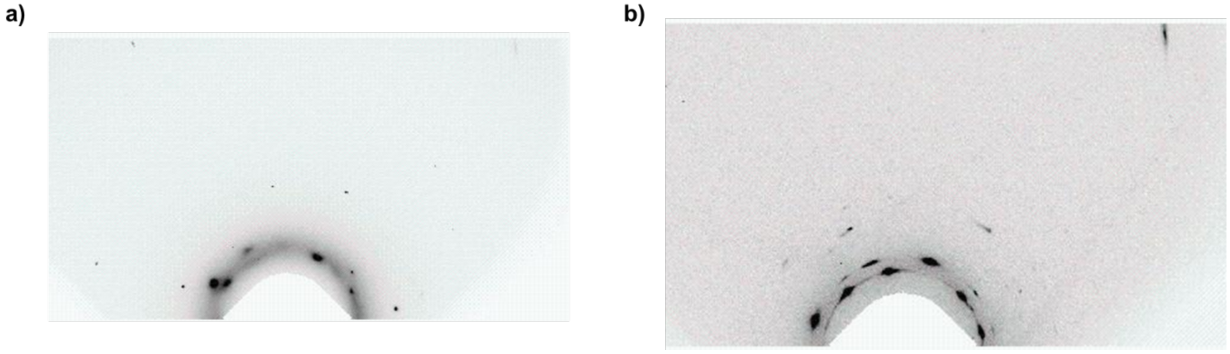

Figure S32. 2D-SAXS pattern of a) β-Mal-$C_{12}C_8$ at 145 °C during heating and b) at 25 °C after cooling.

XVI. Variable Temperature SAXS Profiles of Lactose-based Glycolipids

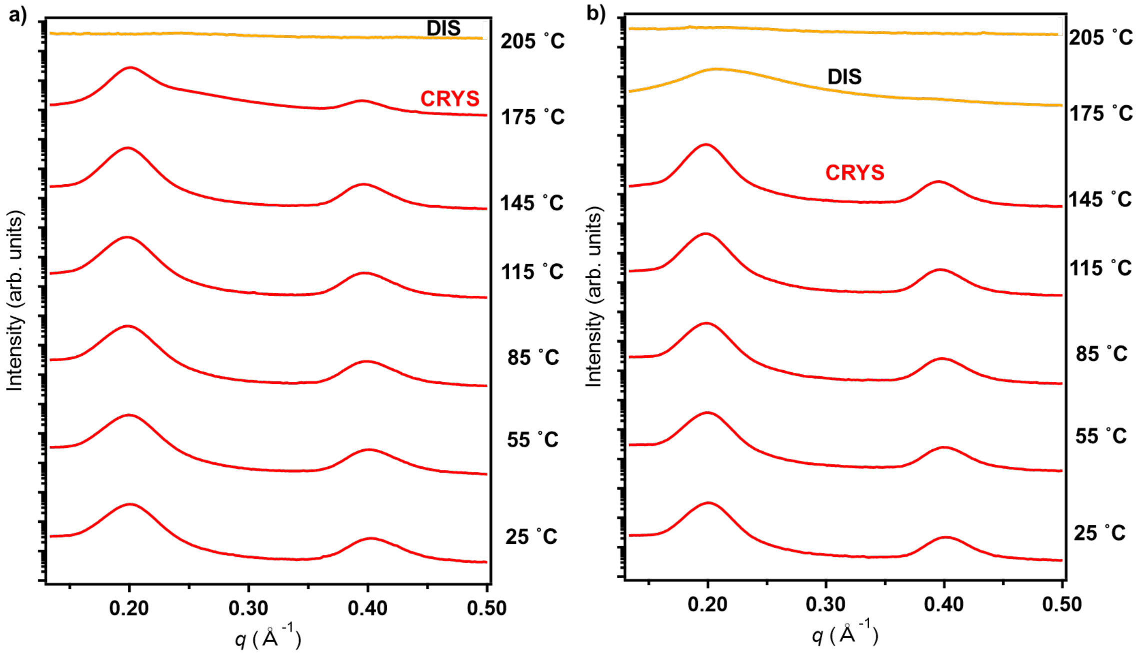

Figure S33. SAXS profile of a) α-Lac-C_6C_2 and b) β- Lac- C_6C_2 within the temperature range of 25-205 °C.

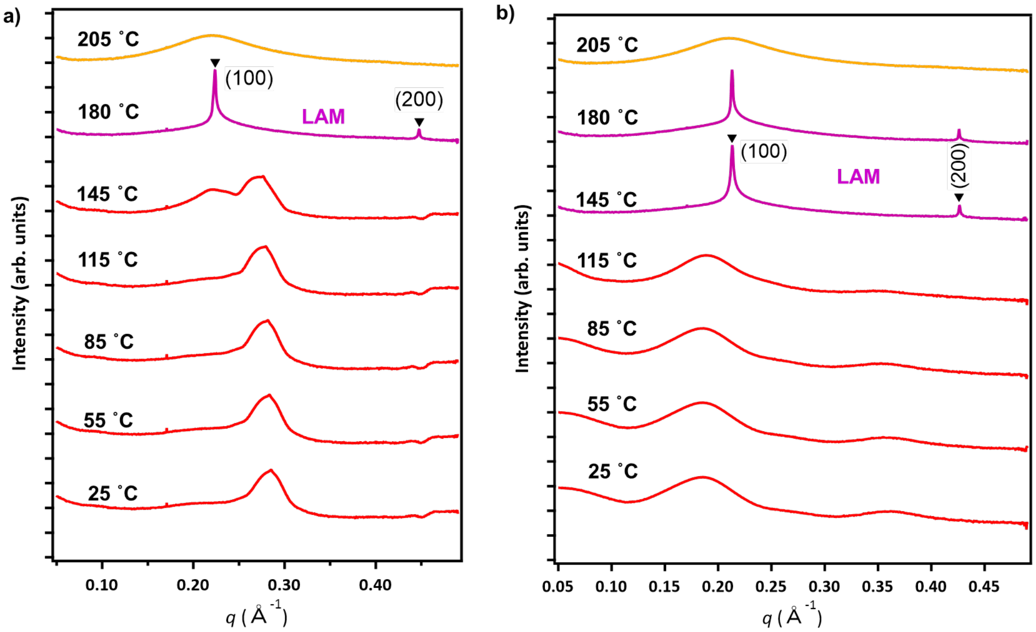

Figure S34. SAXS profile of a) α-Lac-C_8C_4 and b) β- Lac- C_8C_4 within the temperature range of 25-205 °C

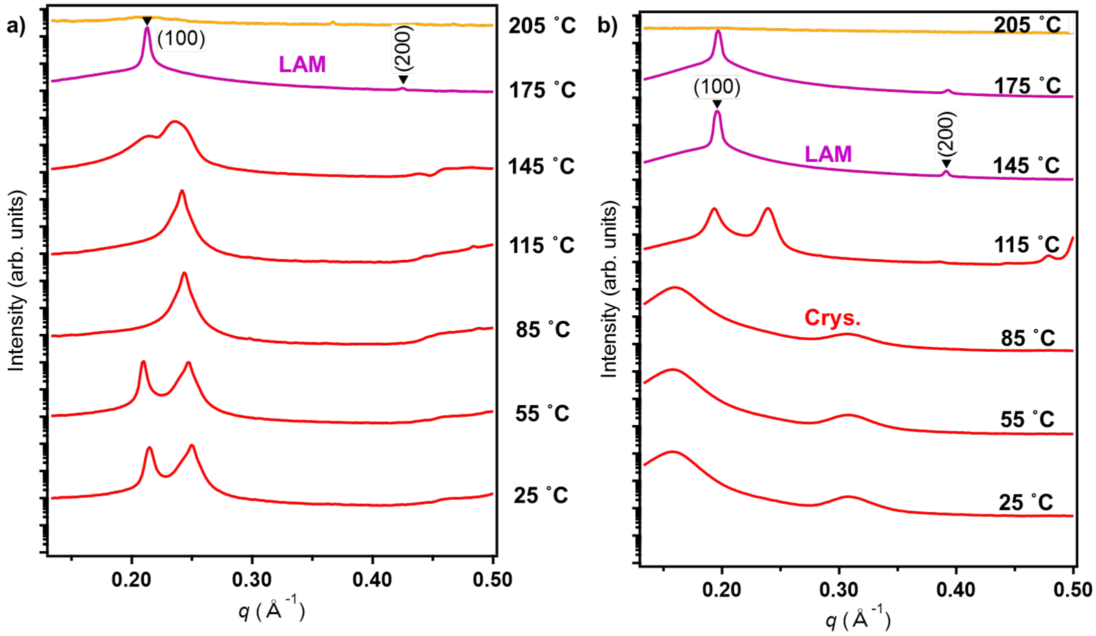

Figure S35. SAXS profile of a) α-Lac-$C_{10}C_6$ and b) β-Lac- $C_{10}C_6$ within the temperature range of 25-205 °C.

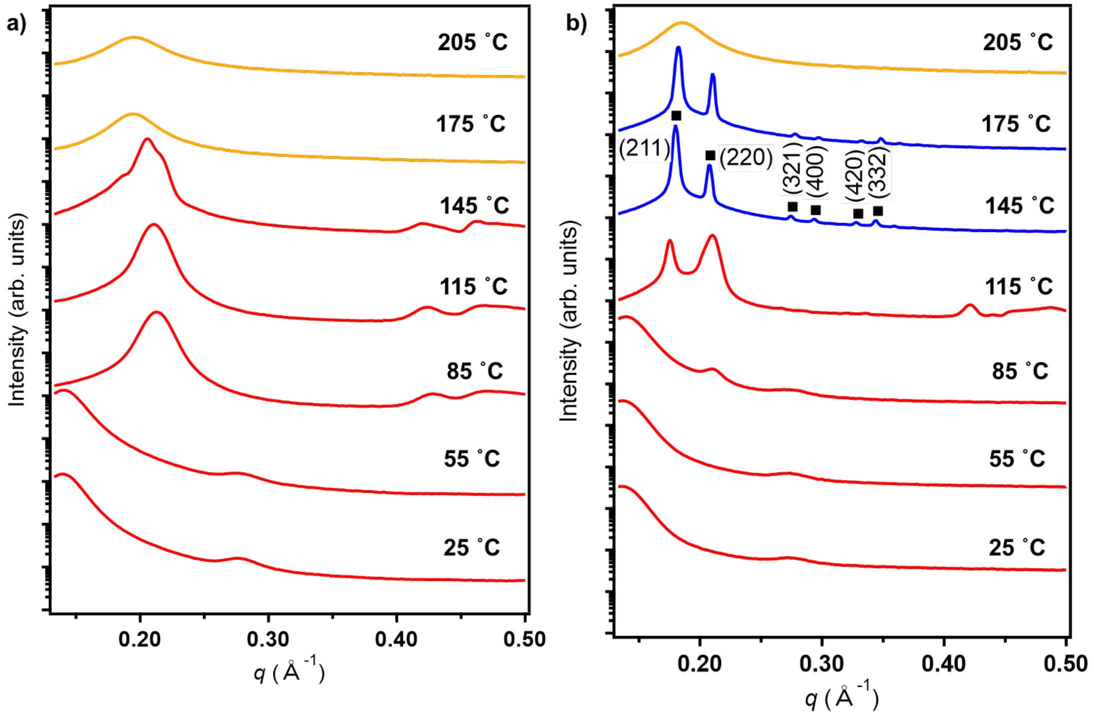

Figure S36. SAXS profile of a) α-Lac-$C_{12}C_8$ and b) β- Lac-$C_{12}C_8$ within the temperature range of 25-205 °C.

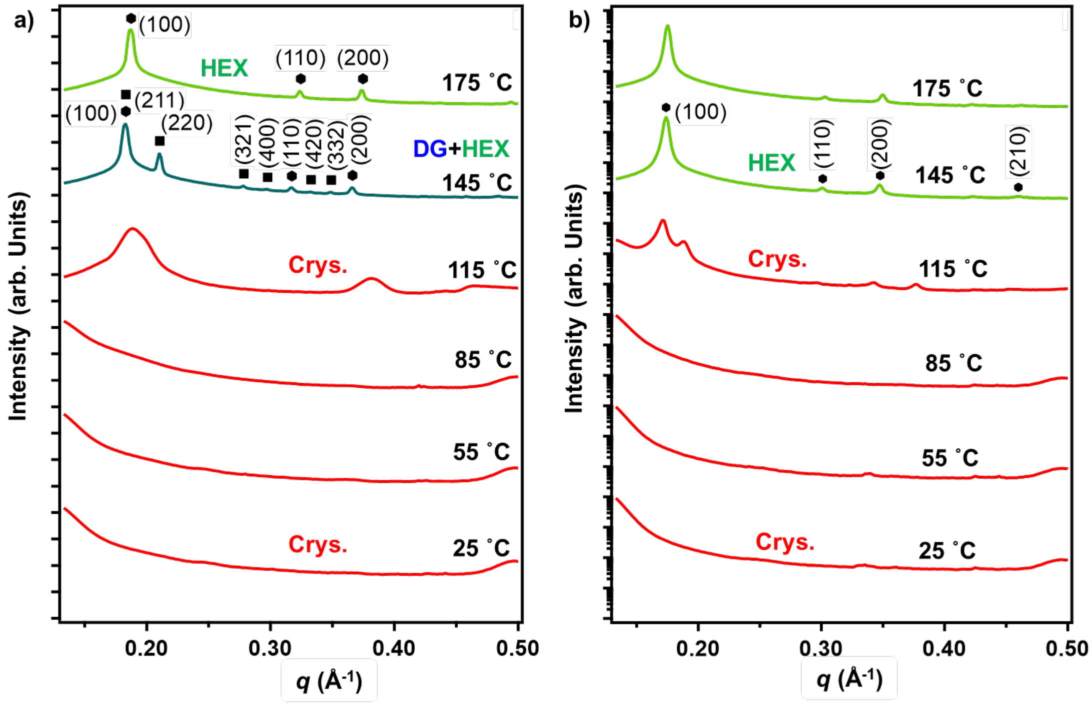

Figure S37. SAXS profile of a) α-Lac-$C_{14}C_{10}$ and b) β- Lac-$C_{14}C_{10}$ within the temperature range of 25-175 °C.

XVII. POM Images of Lactosides

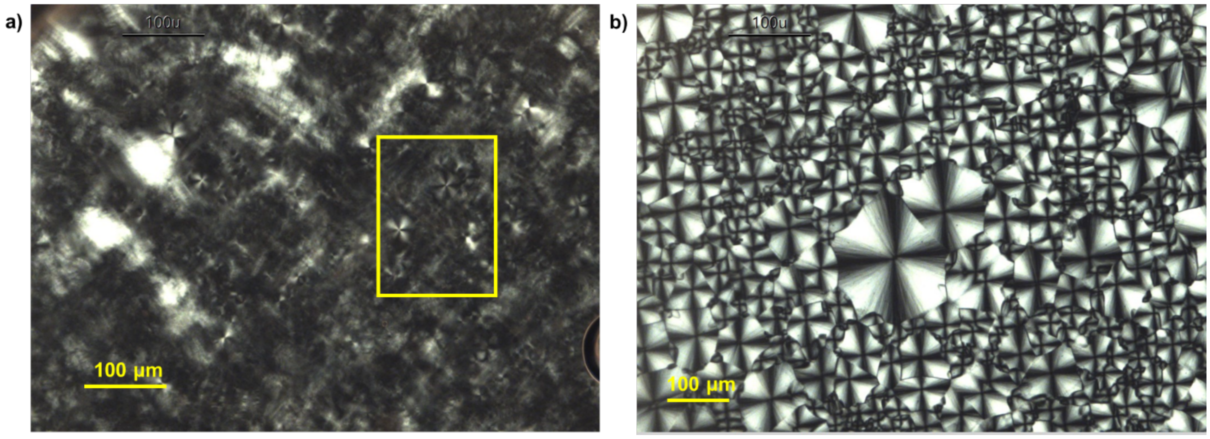

Figure S38. POM images of a) α-Lac-$C_{12}C_8$ at 160 °C during heating, showing focal conic texture representative of smectic A, b) α-Lac-$C_{12}C_8$ at 25 °C after cooling, showing focal conics of a Smectic A LC.

XVIII. 1D SAXS of α-Lac-$C_{14}C_{10}$ during cooling

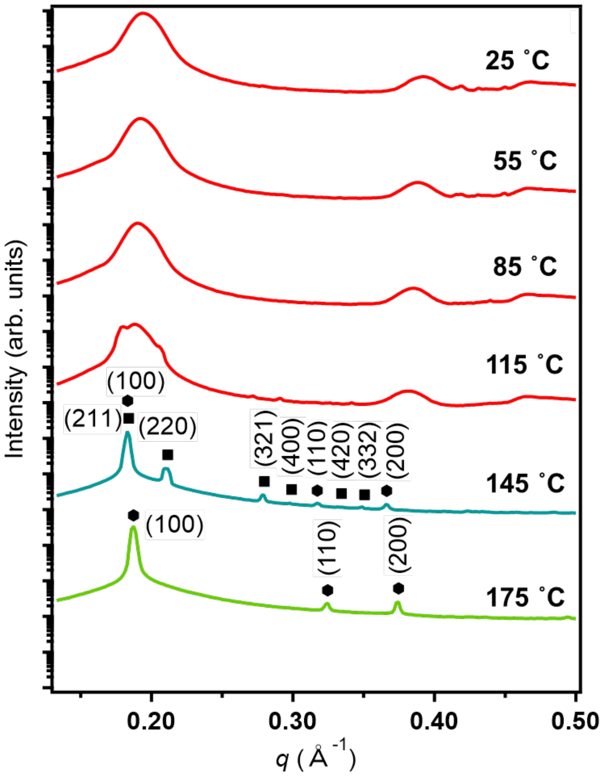

Figure S39. SAXS profile of α-Lac-$C_{14}C_{10}$ after cooling from an isotropic melt state.

XIV. Temperature-dependent Lattice Parameters of LC Phases

Table S3. Lattice parameter of the phases formed by maltosides as a function of temperature

Lipid	Temperature (°C)	α-anomer		β-anomer	
		Phase	Lattice parameter (Å)	Phase	Lattice parameter (Å)
Mal-C_6C_2	85	DIS[a]	-	-	27.7
	115	-	-	-	27.8
	145	-	-	DIS[a]	-
	175	-	-	-	-
Mal-C_8C_4	85	LAM	26.1	LAM	29.3
	115	LAM	26.1	LAM	29.2
	145	DIS[a]	-	-	29.2
	175	DIS[a]	-	DIS[a]	29.2
Mal-$C_{10}C_6$	85	LAM	28.6	LAM	31.3
	115	LAM	28.6	LAM	31.2
	145	LAM	28.6	LAM	31.2
	175	LAM	28.5	DIS[a]	31.2
Mal-$C_{12}C_8$	85	LAM	31.0	LAM	33.1
	115	LAM	31.0	LAM	33.2
	145	LAM	30.8	DG	83.7
	175	LAM	30.5	DG	82.6
Mal-$C_{14}C_{10}$	85	LAM	33.4	DG	94.9
	115	LAM	33.7	DG, HEX	93.5, 44.1
	145	DIS[a]	-	HEX	43.0
	175	DIS[a]	-	HEX	41.5
	205	DIS[a]	-	HEX	41.1

[a] Denotes disordered phase

Table S4. Lattice parameter of the phases formed by lactosides as a function of temperature

Lipid	Temperature (°C)	α-anomer		β-anomer	
		Phase	Lattice parameter (Å)	Phase	Lattice parameter (Å)
Lac-C_6C_2	115	CRYS	-	CRYS	-
	145	CRYS	-	CRYS	-
	175	CRYS	-	DIS[a]	-
	205	DIS[a]	-	DIS[a]	-
Lac -C_8C_4	115	CRYS	-	CRYS	-
	145	CRYS	-	LAM	29.4
	175	LAM	28.1	LAM	29.4
	205	DIS[a]	-	DIS[a]	-
Lac-$C_{10}C_6$	115	CRYS	-	CRYS	-
	145	CRYS	-	LAM	32.1
	175	LAM	29.6	LAM	31.9
	205	DIS[a]	-	DIS[a]	-
Lac-$C_{12}C_8$	115	CRYS	-	CRYS	-
	145	CRYS	-	DG	84.8
	175	DIS[a]	-	DG	84.4
	205	DIS[a]	-	DIS[a]	-
Lac-$C_{14}C_{10}$	115	CRYS	-	CRYS	-
	145	DG, HEX	84.4, 39.6	HEX	41.7
	175	HEX	38.7	HEX	41.4

[a] Denotes disordered phase

XV. POM Images of -C_8C_4 Maltosides and Lactosides

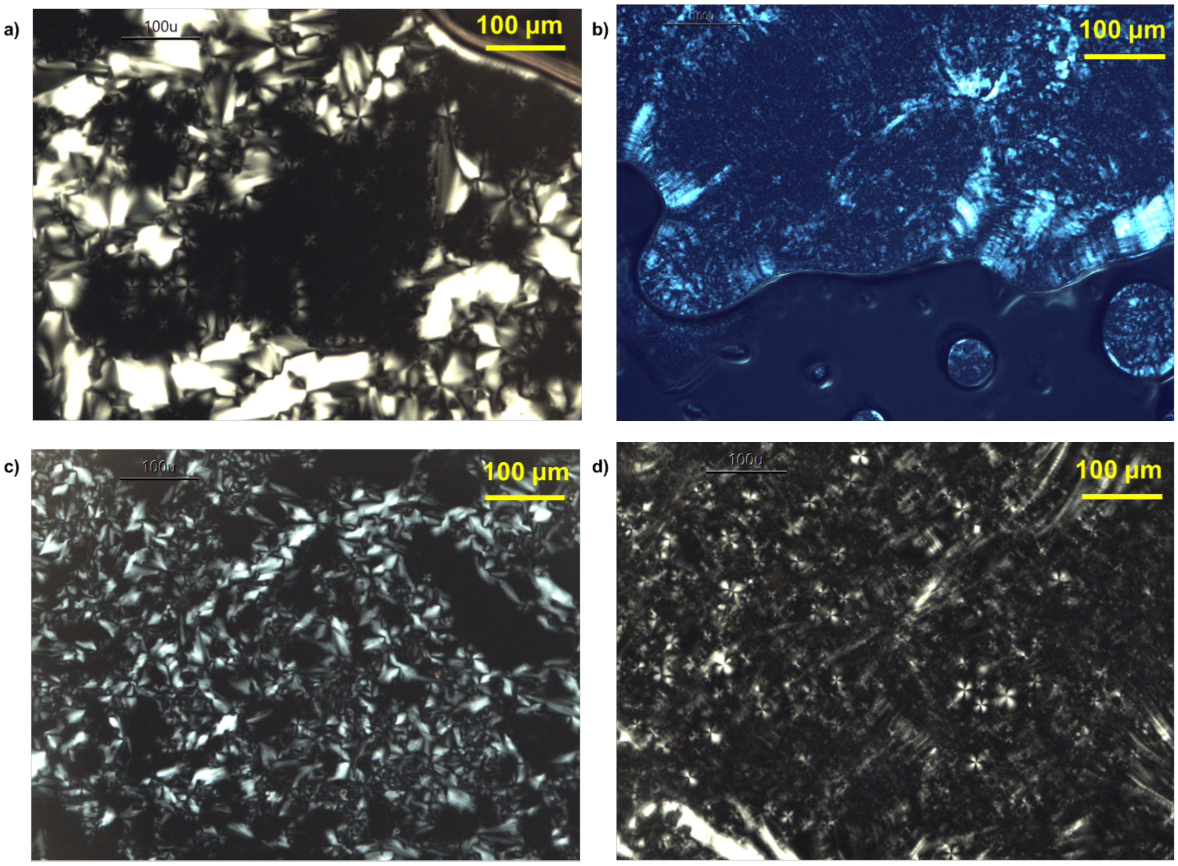

Figure S40. POM images of a) α-Mal-C_8C_4 during cooling at 155 °C showing focal conic texture representative of smectic A, b) β-Mal-C_8C_4 during heating at 145 °C revealing typical focal conic texture of smectic A, c) α-Lac-C_8C_4 during cooling at 166 °C showing focal conic texture representative of smectic A, d) β-Lac-C_8C_4 during heating at 180 °C showing focal conic texture representative of smectic A.

XVI. Molecular Dynamics Simulation of Glycolipids

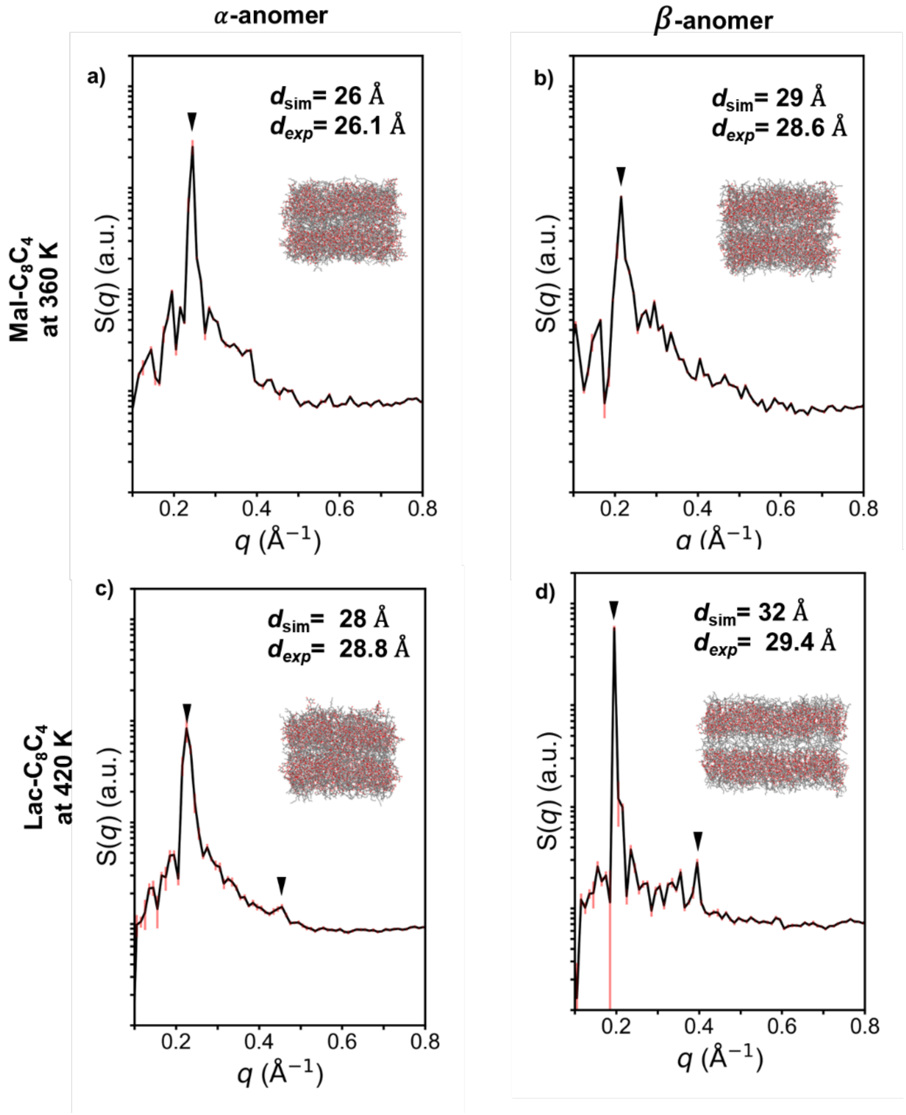

Figure S41. Time-averaged structure factor profile from MD simulation of a,b) Mal-C_8C_4 at 360 K, c,d) Lac-C_8C_4 at 420 K. A snapshot of the molecule packing is also included for each glycolipid

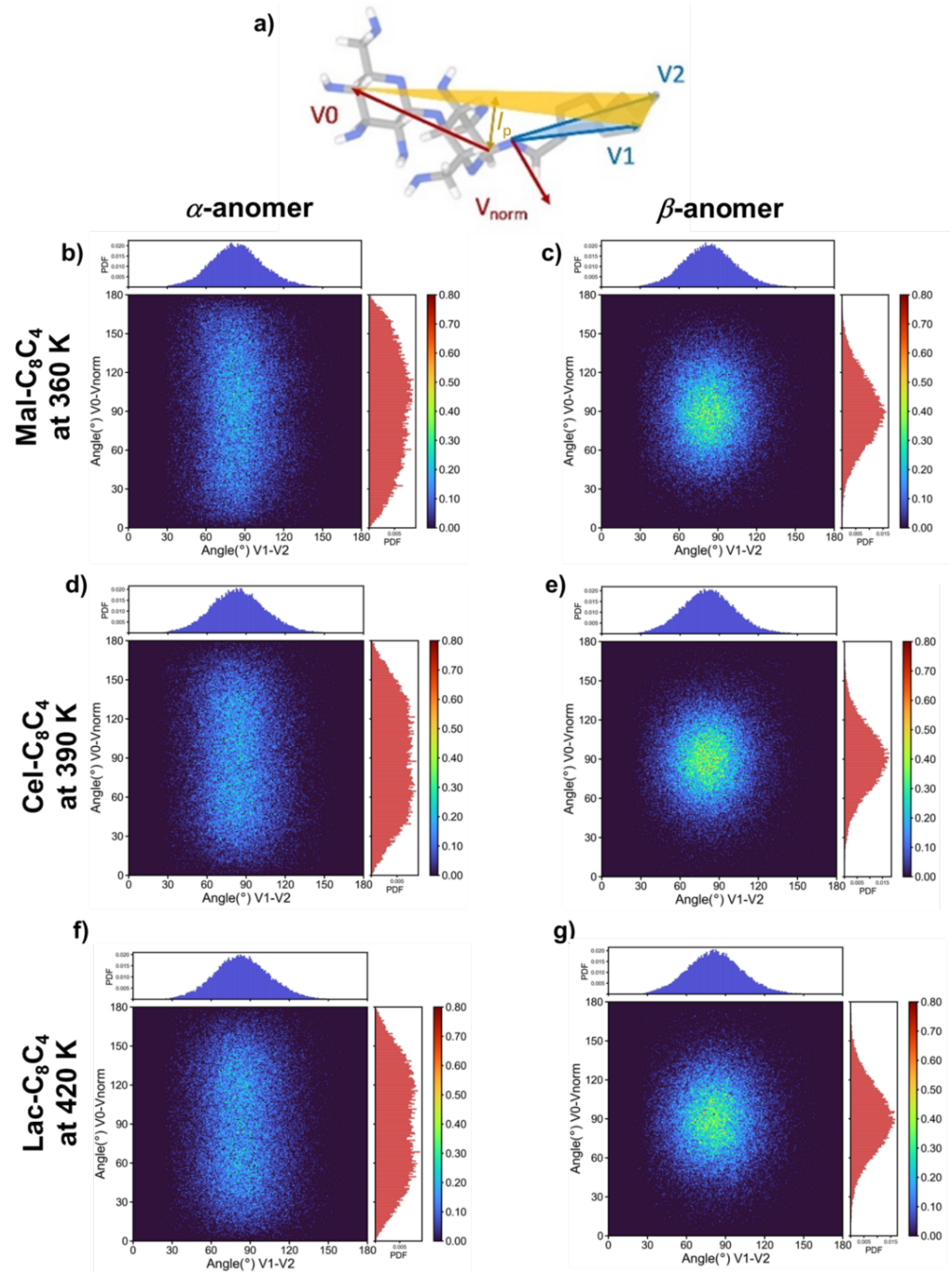

Figure S42. Molecular conformations of Mal-C_8C_4, Cel-C_8C_4, Lac-C_8C_4 at 360 K, 390 K, 420 K in LAM phase from MD simulations. (a) Sketch of plane formed by the distal carbon atoms of the sugar and tail groups (red, "glycolipid plane") and by the ether linker and tail ends (blue "tail plane"). Heat maps of the tail splay angle (V_1-V_2) and angle between the long axis of the head group and the normal to the tail plane ($V_0 - V_{norm}$) for α- and β- anomers of (b,c) Mal-C_8C_4, (d,e) Cel-C_8C_4, (f,g) Lac-C_8C_4 at 420 K.

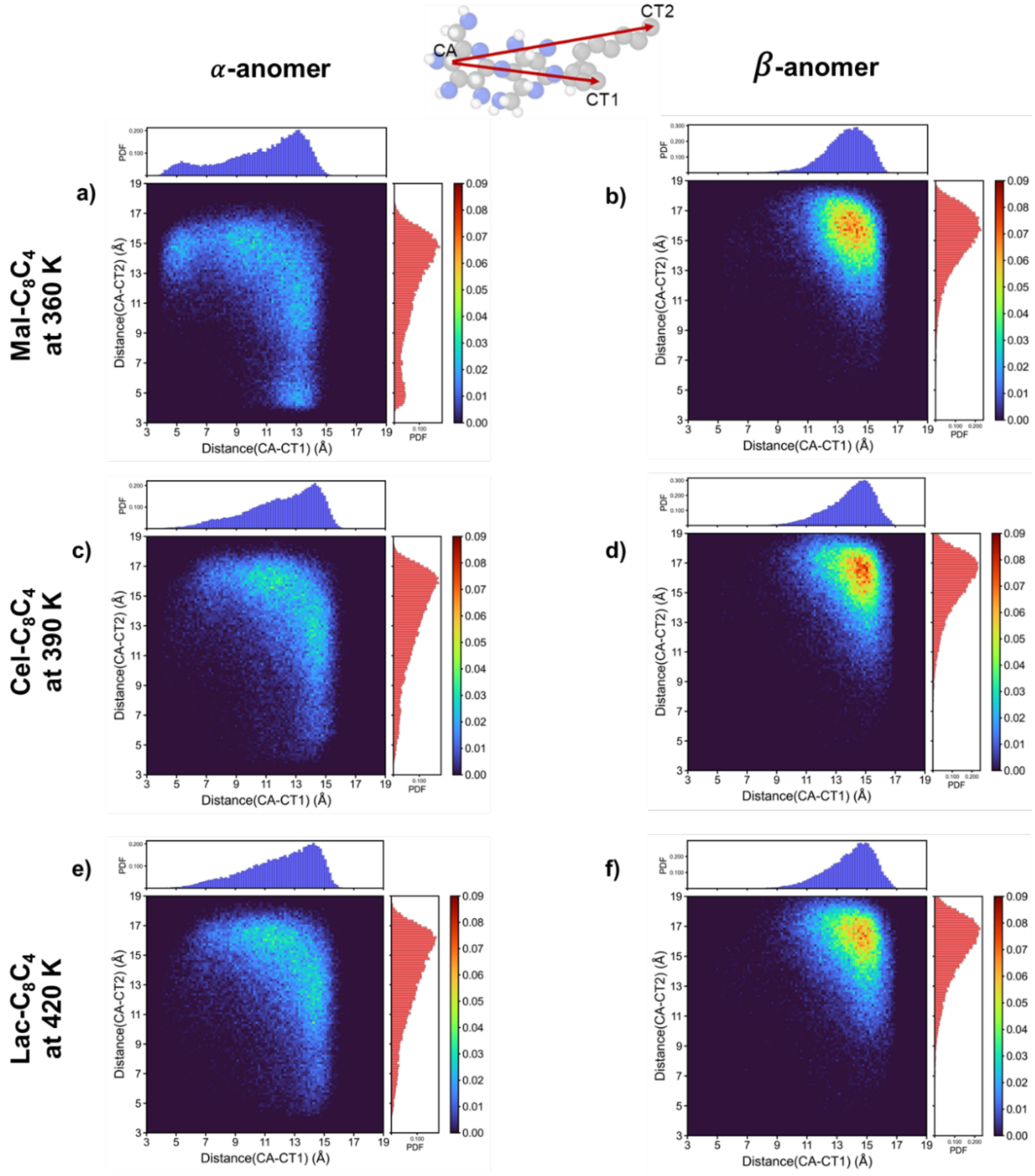

Figure S43. 2D heatmap of the distance distribution of a) α-Mal-C_8C_4, b) β-Mal-C_8C_4, c) α-Cel-C_8C_4, d) β-Cel-C_8C_4, e) α-Lac-C_8C_4, f) β-Lac-C_8C_4. The color bar value denotes the probability density at the bin.

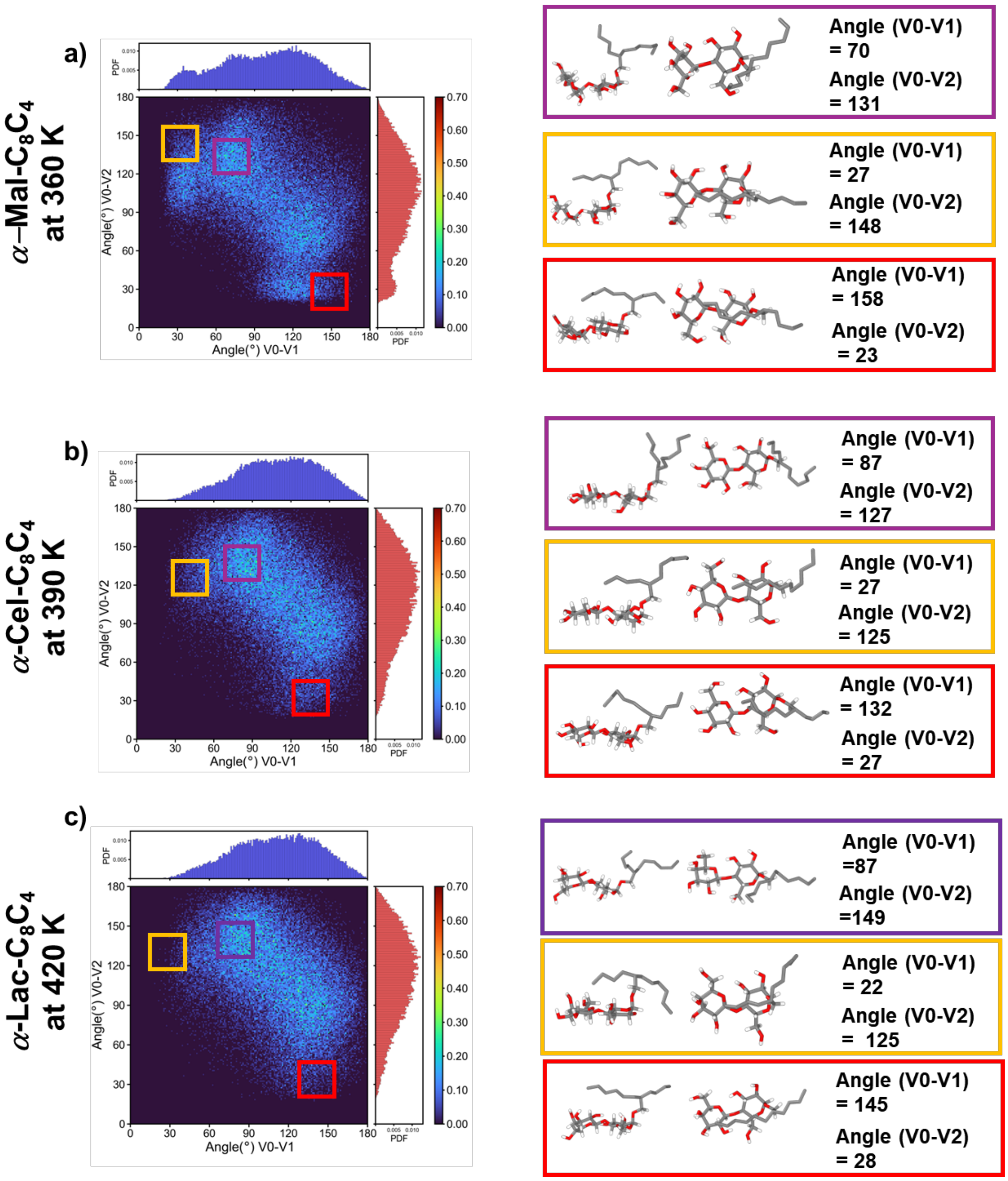

Figure S44. 2D heatmap of the angle distribution of a) α-Mal-C_8C_4, b) α-Cel-C_8C_4, c) α-Lac-C_8C_4. The color bar value denotes the probability density (scaled by 1000) at the bin. Selected configurations of all a-anomers shown in the yellow, purple and red colored boxes.

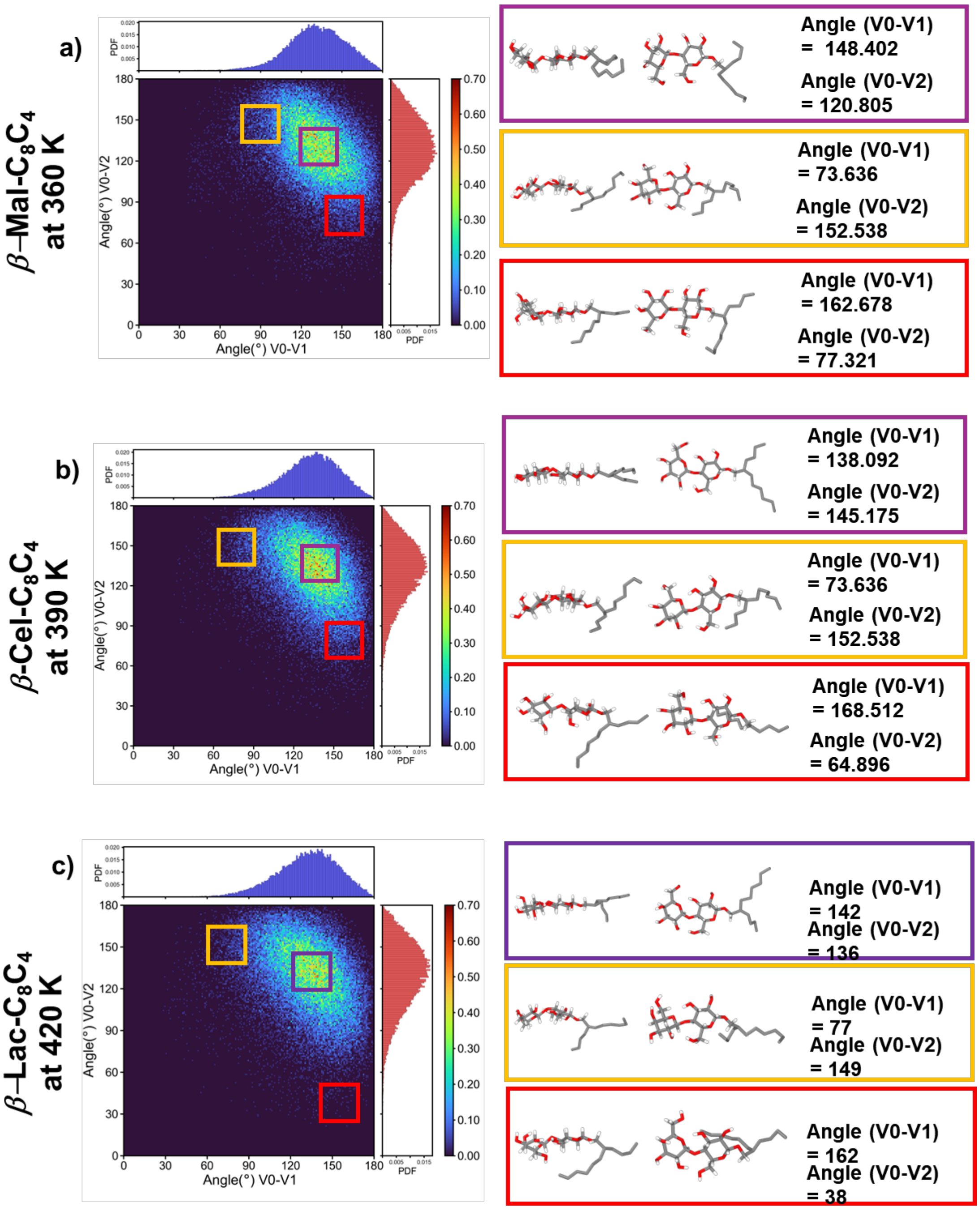

Figure S45. 2D heatmap of the angle distribution of a) *β*-Mal-C$_8$C$_4$, b) *β*-Cel-C$_8$C$_4$, c) *β*-Lac-C$_8$C$_4$. The color bar value denotes the probability density (scaled by 1000) at the bin. Selected configurations of all a-anomers shown in the yellow, purple and red colored boxes.

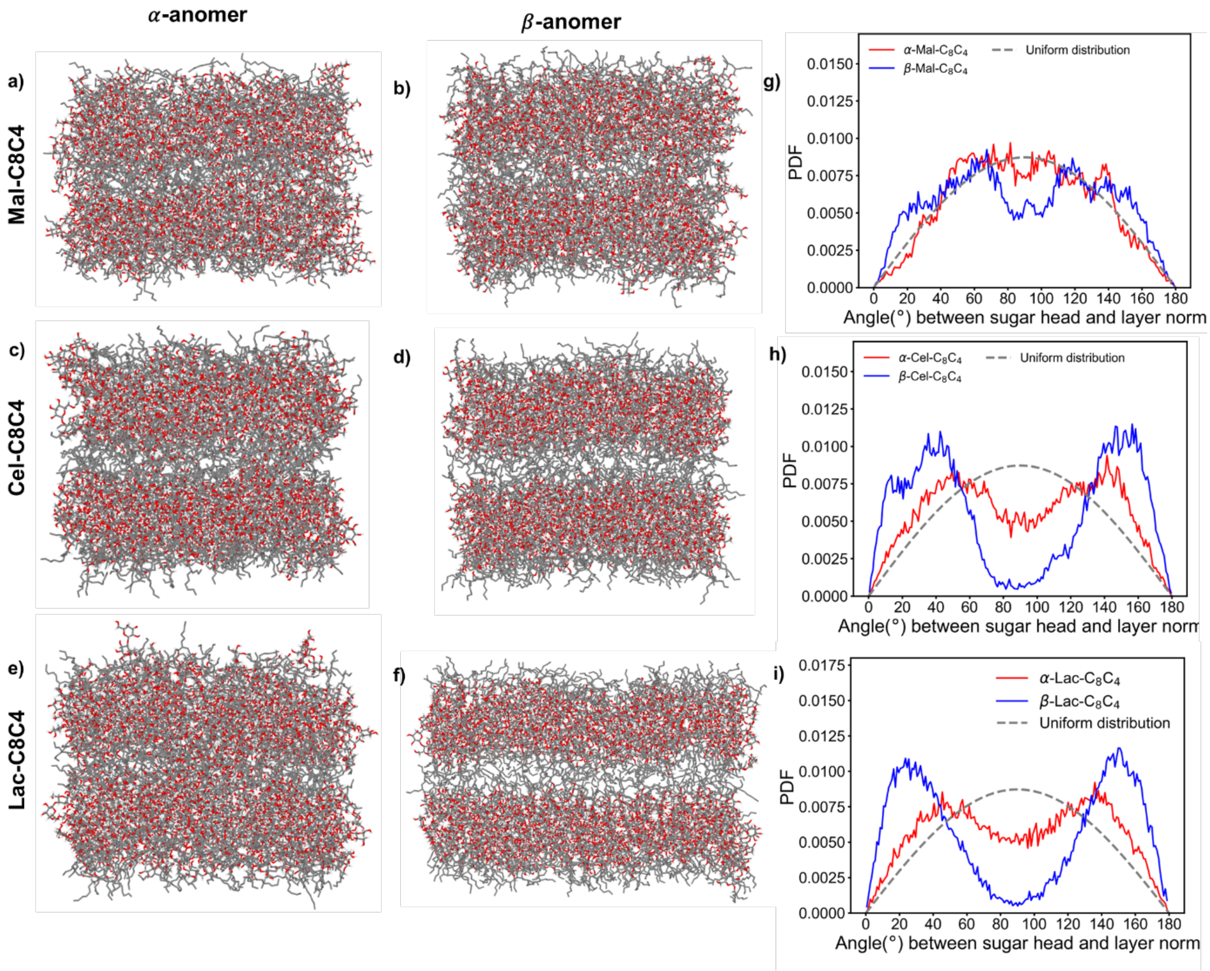

Figure S46. Snapshots of the simulation box of a) α-Mal-C$_8$C$_4$, b) β-Mal-C$_8$C$_4$, c) α-Cel-C$_8$C$_4$, d) β-Cel-C$_8$C$_4$, e) α-Lac-C$_8$C$_4$, f) β-Lac-C$_8$C$_4$. Distribution of the angle between the sugar head and the LAM layer norm in g) α-,β-Mal-C$_8$C$_4$, h) α-,β-Cel-C$_8$C$_4$, i) α,β-Lac-C$_8$C$_4$. α and β-anomers were represented by red and blue lines respectively. The uniform distribution between two randomly oriented vectors is shown for comparison (grey dashed line).

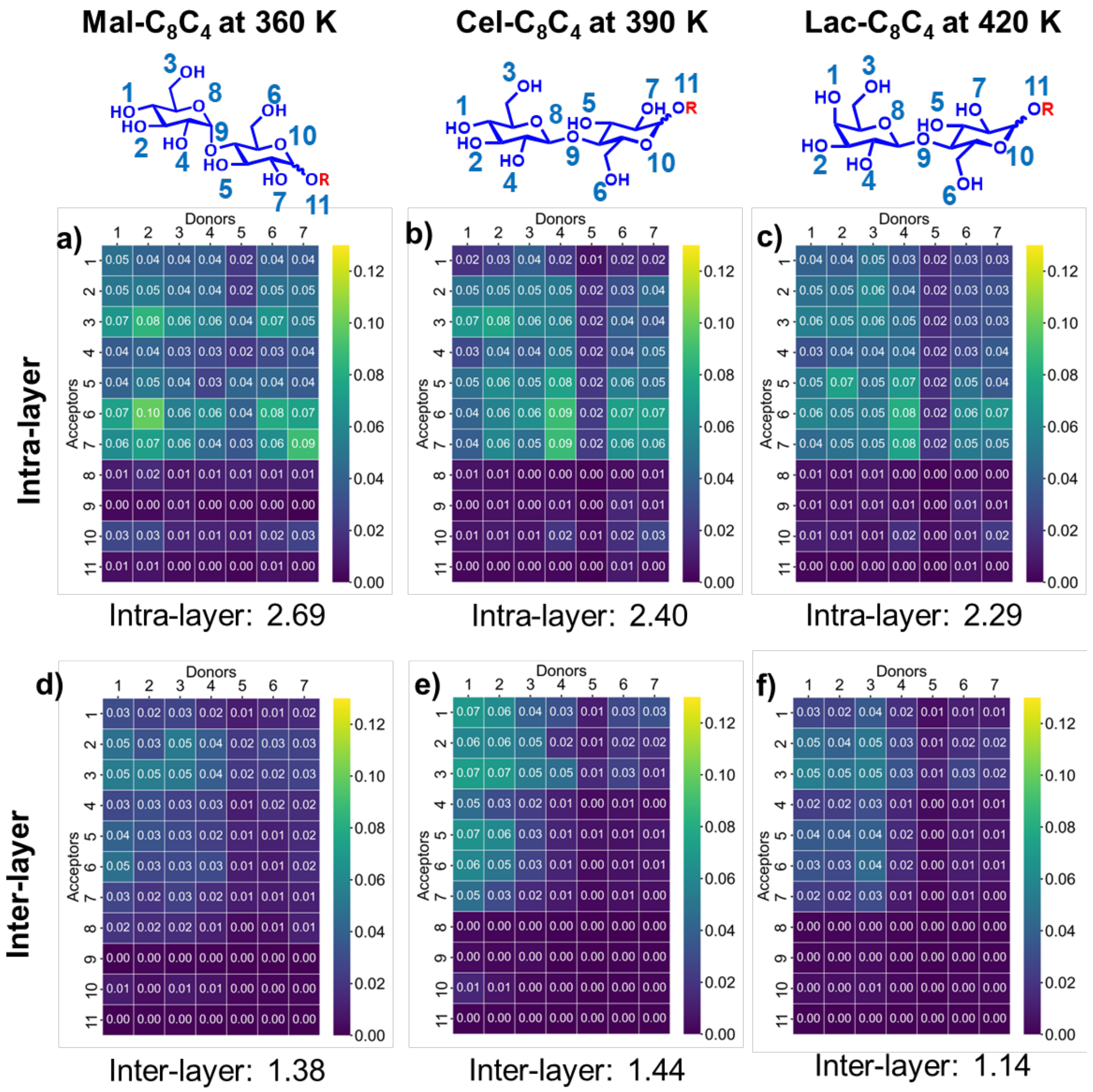

Figure S47. Map of intra-layer H-bonding in a) α-Mal-C_8C_4, b) α-Cel-C_8C_4, c) α-Lac-C_8C_4 and inter-layer H-bonding in d) α-Mal-C_8C_4, e) α-Cel-C_8C_4, f) α-Lac-C_8C_4. The value of color bar refers to the occurrence of H-bonding between certain sites divided by the total number of molecules examined. The numbers mentioned at the bottom of each H-bonding map represent the total count of occurrence of H-bonding.

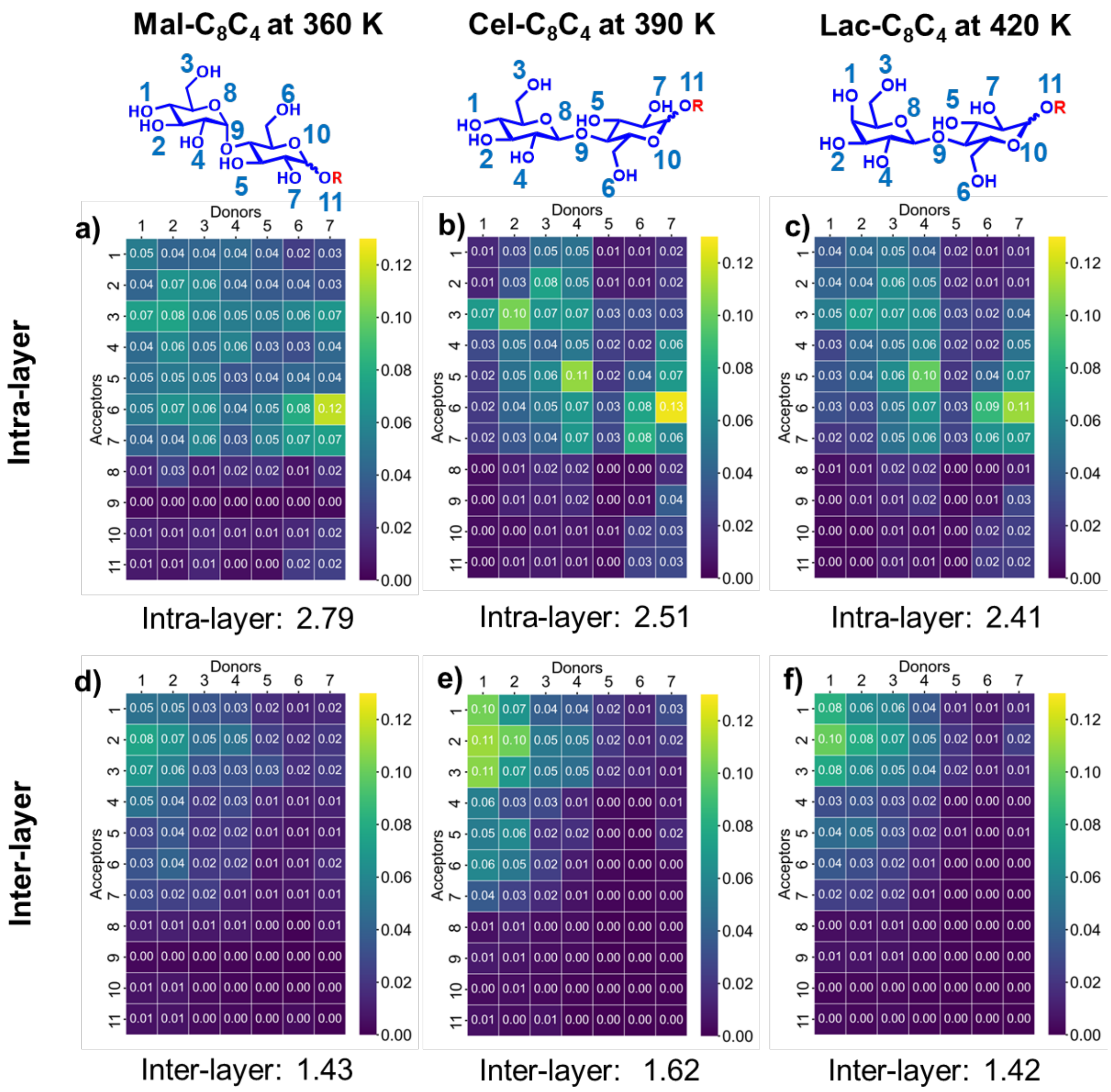

Figure S48. Map of intra-layer H-bonding in a) *β*-Mal-C_8C_4, b) *β*-Cel-C_8C_4, c) *β*-Lac-C_8C_4 and inter-layer H-bonding in d) *β*-Mal-C_8C_4, e) *β*-Cel-C_8C_4, and f) *β*-Lac-C_8C_4 . The value of color bar refers to the occurrence of H-bonding between certain sites divided by the total number of molecules examined. The numbers mentioned at the bottom of each H-bonding map represent the total count of occurrences of H-bonding.

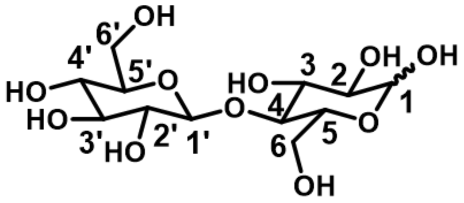

Hydroxyl Group Number	Carbon Position
1	C4’
2	C3’
3	C6’
4	C3’
5	C3
6	C6
7	C2

Figure S49. Description of the hydroxyl group position to the sugar group carbon

XVII. Schematics of Intra- and Inter-layer hydrogen bonding

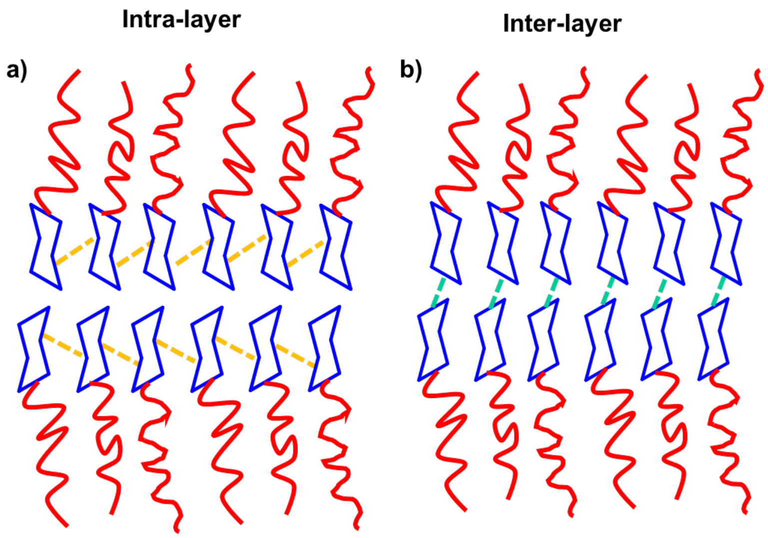

Figure S50. Schematic description of a) intra-layer, b) inter-layer hydrogen bonding.

XVIII. References:

1. Alam, M. A.; Motoyanagi, J.; Yamamoto, Y.; Fukushima, T.; Kim, J.; Kato, K.; Takata, M.; Saeki, A.; Seki, S.; Tagawa, S., “Bicontinuous cubic” liquid crystalline materials from discotic molecules: a special effect of paraffinic side chains with ionic liquid pendants. *J. Am. Chem. Soc.* **2009,** *131* (49), 17722-17723.

2. Saari, N. N.; Mislan, A. A.; Hashim, R.; Zahid, N. I., Self-assembly, thermotropic, and lyotropic phase behavior of guerbet branched-chain maltosides. *Langmuir* **2018,** *34* (30), 8962-8974.

3. Zahid, N. I.; Conn, C. E.; Brooks, N. J.; Ahmad, N.; Seddon, J. M.; Hashim, R., Investigation of the effect of sugar stereochemistry on biologically relevant lyotropic phases from branched-chain synthetic glycolipids by small-angle X-ray scattering. *Langmuir* **2013,** *29* (51), 15794-15804.

4. Patrick, M.; Zahid, N. I.; Kriechbaum, M.; Hashim, R., Guerbet glycolipids from mannose: liquid crystals properties. *Liq. Crys.* **2018,** *45* (13-15), 1970-1986.

5. Chen, K.; Chen, C.-Y.; Chen, H.-L.; Komaki, R.; Kawakami, N.; Isono, T.; Satoh, T.; Hung, D.-Y.; Liu, Y.-L., Self-assembly behavior of sugar-based block copolymers in the complex phase window modulated by molecular architecture and configuration. *Macromolecules* **2022,** *56* (1), 28-39.

6. Nowak, S. R.; Lachmayr, K. K.; Yager, K. G.; Sita, L. R., Stable Thermotropic 3D and 2D Double Gyroid Nanostructures with Sub-2-nm Feature Size from Scalable Sugar–Polyolefin Conjugates. *Angew. Chem., Int. Ed.* **2021,** *133* (16), 8792-8798.

7. Von Minden, H.; Brandenburg, K.; Seydel, U.; Koch, M.; Garamus, V.; Willumeit, R.; Vill, V., Thermotropic and lyotropic properties of long chain alkyl glycopyranosides. Part II. Disaccharide headgroups. *Chem. Phys. Lipids* **2000,** *106* (2), 157-179.

8. Hashim, R.; Hashim, H. H. A.; Rodzi, N. Z. M.; Hussen, R. S. D.; Heidelberg, T., Branched chain glycosides: Enhanced diversity for phase behavior of easily accessible synthetic glycolipids. *Thin Solid Films* **2006,** *509* (1-2), 27-35.

9. Bonnet, C.; Guillet, P.; Igonet, S.; Meister, A.; Marconnet, A.; Keller, S.; Jawhari, A.; Durand, G., Hybrid double-chain maltose-based detergents: Synthesis and colloidal and biochemical evaluation. *J. Org. Chem.* **2019,** *84* (17), 10606-10614.

10. Periyannan, G. R.; Lawrence, B. A.; Egan, A. E., 1H NMR spectroscopy-based configurational analysis of mono-and disaccharides and detection of β-glucosidase activity: an undergraduate biochemistry laboratory. *J. Chem. Educ.* **2015,** *92* (7), 1244-1249.

11. Aripin, N. F. K., *Synthesis and characterisation of maltosides and lactosides based on alcohol mixtures obtained from palm oil and palm kernel oil*. University of Malaya (Malaysia): 2009.

12. Lindsay, A. P.; Mueller, A. J.; Mahanthappa, M. K.; Lodge, T. P.; Bates, F. S., 1D SAXS indexing macro for Igor Pro. **2021**.

13. Raman, E. P.; Guvench, O.; MacKerell Jr, A. D., CHARMM additive all-atom force field for glycosidic linkages in carbohydrates involving furanoses. *J. Phys. Chem. B.* **2010,** *114* (40), 12981-12994.

14. Guvench, O.; Mallajosyula, S. S.; Raman, E. P.; Hatcher, E.; Vanommeslaeghe, K.; Foster, T. J.; Jamison, F. W.; MacKerell Jr, A. D., CHARMM additive all-atom force field for carbohydrate derivatives and its utility in polysaccharide and carbohydrate–protein modeling. *J. Chem. Theory Comput.* **2011,** *7* (10), 3162-3180.

15. Jo, S.; Kim, T.; Iyer, V. G.; Im, W., CHARMM-GUI: a web-based graphical user interface for CHARMM. *J. Comput. Chem.* **2008,** *29* (11), 1859-1865.

16. Lee, J.; Patel, D. S.; Ståhle, J.; Park, S.-J.; Kern, N. R.; Kim, S.; Lee, J.; Cheng, X.; Valvano, M. A.; Holst, O., CHARMM-GUI membrane builder for complex biological membrane simulations with glycolipids and lipoglycans. *J. Chem. Theory Comput.* **2018,** *15* (1), 775-786.

17. Martin, M. G.; Siepmann, J. I., Transferable potentials for phase equilibria. 1. United-atom description of n-alkanes. *J. Phys. Chem. B* **1998,** *102* (14), 2569-2577.

18. Chen, B.; Potoff, J. J.; Siepmann, J. I., Monte Carlo calculations for alcohols and their mixtures with alkanes. Transferable potentials for phase equilibria. 5. United-atom description of primary, secondary, and tertiary alcohols. *J. Phys. Chem. B* **2001,** *105* (15), 3093-3104.

19. Stubbs, J. M.; Potoff, J. J.; Siepmann, J. I., Transferable potentials for phase equilibria. 6. United-atom description for ethers, glycols, ketones, and aldehydes. *J. Phys. Chem. B* **2004,** *108* (45), 17596-17605.

20. Martínez, L.; Andrade, R.; Birgin, E. G.; Martínez, J. M., PACKMOL: A package for building initial configurations for molecular dynamics simulations. *J. Comput. Chem.* **2009,** *30* (13), 2157-2164.

21. Van Der Spoel, D.; Lindahl, E.; Hess, B.; Groenhof, G.; Mark, A. E.; Berendsen, H. J., GROMACS: fast, flexible, and free. *J. Comput. Chem.* **2005,** *26* (16), 1701-1718.

22. Berendsen, H. J.; Postma, J. v.; Van Gunsteren, W. F.; DiNola, A.; Haak, J. R., Molecular dynamics with coupling to an external bath. *J. Chem. Phys.* **1984,** *81* (8), 3684-3690.

23. NOSÉ, S., A molecular dynamics method for simulations in the. *Mol. Phys. 52* (2).

24. Hoover, W. G., Canonical dynamics: Equilibrium phase-space distributions. *Phys. Rev. A.* **1985,** *31* (3), 1695.

25. Parrinello, M.; Rahman, A., Polymorphic transitions in single crystals: A new molecular dynamics method. *J. Appl. Phys.* **1981,** *52* (12), 7182-7190.

26. Nosé, S.; Klein, M. L., Constant pressure molecular dynamics for molecular systems. *Mol. Phys.* **1983,** *50* (5), 1055-1076.

27. Das, S.; Zheng, C.; Lodge, T. P.; Siepmann, J. I.; Mahanthappa, M. K.; Calabrese, M. A.; Reineke, T. M., Self-Assembly of Unusually Stable Thermotropic Network Phases by Cellobiose-Based Guerbet Glycolipids. *Biomacromolecules* **2024,** *25* (2), 1291-1302.

28. Ogawa, S.; Asakura, K.; Osanai, S., Thermotropic and glass transition behaviors of n-alkyl β-D-glucosides. *RSC Adv.* **2013,** *3* (44), 21439-21446.

29. Gerber, S.; Wulf, M.; Milkereit, G.; Vill, V.; Howe, J.; Roessle, M.; Garidel, P.; Gutsmann, T.; Brandenburg, K., Phase diagrams of monoacylated amide-linked disaccharide glycolipids. *Chem. Phys. Lipids* **2009,** *158* (2), 118-130.

30. Stefaniu, C.; Latza, V. M.; Gutowski, O.; Fontaine, P.; Brezesinski, G.; Schneck, E., Headgroup-ordered monolayers of uncharged glycolipids exhibit selective interactions with ions. *J. Phys. Chem. Lett.* **2019,** *10* (8), 1684-1690.

31. Yu, Z.; Calvert, T.; Leckband, D., Molecular forces between membranes displaying neutral glycosphingolipids: evidence for carbohydrate attraction. *Biochemistry* **1998,** *37* (6), 1540-1550.

32. Schneider, M. F.; Zantl, R.; Gege, C.; Schmidt, R. R.; Rappolt, M.; Tanaka, M., Hydrophilic/hydrophobic balance determines morphology of glycolipids with oligolactose headgroups. *Biophys. J.* **2003,** *84* (1), 306-313.

33. Hinz, H.; Kuttenreich, H.; Meyer, R.; Renner, M.; Fründ, R.; Koynova, R.; Boyanov, A.; Tenchov, B., Stereochemistry and size of sugar head groups determine structure and phase behavior of glycolipid membranes: densitometric, calorimetric, and X-ray studies. *Biochemistry* **1991,** *30* (21), 5125-5138.

34. Tanaka, M.; Schneider, M. F.; Brezesinski, G., In-Plane Structures of Synthetic Oligolactose Lipid Monolayers—Impact of Saccharide Chain Length. *ChemPhysChem* **2003,** *4* (12), 1316-1322.

35. Larsson, K., Physical properties—structural and physical characteristics. In *The lipid handbook*, Springer: 1986; pp 321-384.